# THÈSE

pour obtenir le grade de

## Docteur de l'Université Joseph Fourier Grenoble I

*Discipline*: Physique

présentée et soutenue publiquement
par:


## Carla Cristina Gil Abilio


le 15 Novembre 1999

---

## EFFETS DE LOCALISATION INDUITS PAR LE CHAMP MAGNÉTIQUE DANS DES RÉSEAUX SUPRACONDUCTEURS

---

Composition du jury:

| | |
|---|---|
| F. Hekking | |
| M. Konczykowski | Rapporteur |
| D. Mailly | Rapporteur |
| D. Feinberg | |
| M. Godinho | |
| B. Pannetier | |


Thèse préparée au Centre de Recherches sur les Très Basses Températures
CNRS - GRENOBLE

# Contents

# Remerciements

Ce travail a été réalisé au Centre de Recherches sur les Très Basses Températures et a été soutenu financièrement durant ces trois années par une bourse PRAXIS XXI du Ministère pour la Science et Technologie portugais. Au long de ces trois années j'ai pu profiter de l'ambiance chaleureuse et décontractée dans le laboratoire en même temps que scientifiquement très efficace. Je suis très reconnaissante à l'ensemble du personnel du laboratoire pour leur patience et disponibilité envers moi durant toute la durée de cette thèse.

J'exprime ma respectueuse reconnaissance à Monsieur Bernard Hebral, Directeur du Centre de Recherches sur les Très Basses Températures, pour l'accueil qu'il m'a réservé et l'intérêt qu'il a porté à ce travail.

Mes sincères remerciements s'adressent à Monsieur le Professeur Frank Hekking pour avoir accepté de présider le jury de cette thèse. J'adresse mes chaleureux remerciements à Monsieur Marcin Konczykowski, Directeur de Recherches au CNRS, et Monsieur Dominique Mailly, Directeur de Recherches au CNRS, qui ont bien voulu mobiliser leur temps et leur compétence pour être rapporteurs de ce travail. Je remercie aussi M. D. Feinberg, Directeur de Recherches au CNRS d'avoir bien voulu faire partie de mon jury de thèse.

Je tiens aussi à remercier Mme le Professeur Margarida Godinho, Université de Lisbonne, qui m'a transmis son enthousiasme pour la recherche pendant la première expérience en physique expérimentale que j'ai acquise dans son laboratoire. Je lui suis reconnaissante d'avoir accepté de participer à mon jury de thèse.

Monsieur Bernard Pannetier, Directeur de Recherches au CNRS, a dirigé mes recherches avec beaucoup d'enthousiame durant ces trois années. J'ai pu apprécier ses larges compétences et sa culture scientifique qui m'ont été précieuses et je lui suis infiniment reconnaissante pour sa disponibilité et ses dispositions optimistes.

Durant ces trois années j'ai pu profiter des nombreuses discussions avec plusieurs chercheurs européens dans le cadre du 'Training and Mobility of Researchers Programme on Superconducting Nanodevice'. En particulier, je tiens à remercier vivement M. Rosario Fazio, Professeur à l'Université de Catania, Italie, pour les nom-

breuses discussions scientifiques durant ces trois années et son amitié, et également M. Piero Martinoli, Professeur à l'Institut de Physique de Neuchâtel, Suisse, et M. Korshunov, de l'Institut Landau, Russie, pour leur intérêt dans ce travail.

J'adresse aussi mes chaleureux remerciements à Messieurs Julien Vidal, Rémy Mosseri et Benoit Douçot qui nous ont motivés pour la réalisation d'une partie des expériences et à M. Patrick Butaud qui à participé dans cette recherche avec beaucoup d'enthousiasme. Les discussions théoriques avec eux m'ont beaucoup apporté.

J'exprime aussi ma sincère gratitude à M. Olivier Buisson pour son aimable disponibilité et les nombreuses discussions qui m'ont beaucoup aidées.

Une partie des échantillons étudié dans cette thèse ont été fabriqués au laboratoire du CRTBT. Je remercie M. Thierry Crozes pour sa contribution à plusieurs niveaux et sa grande disponibilité pour résoudre les petits problèmes des litho-débutants. Je remercie M. Thierry Fournier qui a réalisé de splendides photos au MEB du CEA-LETI et aussi au TEM du laboratoire de Cristallographie.

Dans le cadre du programme PLATO, j'ai pu profiter de la contribution de l'équipe du CEA-LETI pour la fabrication des échantillons. L'engagement et l'enthousiasme de M. Th. Fournier du CRTBT et aussi de M. S. Tedesco et M. B. Dalzotto du CEA-LETI ont été indispensables pour le bon déroulement de cette collaboration.

Je remercie aussi M. Peter Scheuzger, du groupe du Professeur Piero Martinoli, qui nous a gentiment lithographié et cédé les réseaux de jonctions Josephson pour mes calibrations de champ magnétique.

Enfin, mes remerciements s'adressent à l'ensemble des chercheurs et thésards de l'équipe de Mésoscopie pour la bonne ambiance: Olivier, Hervé, Monique, Klaus, Benedetta, Cécile, Pascal, Norbert, Laurent, et Wilfried.

J'exprime ma profonde gratitude à Michael Borowski et à Sarah Mimran qui m'ont beaucoup aidé à mettre en forme ce mémoire et dans les traductions en français. Je tiens aussi à remercier Hervé Courtois, Monique Giroud, Patrick Butaud et Olivier Buisson pour leur lecture critique de quelques parties du manuscript.

Je voudrais enfin exprimer ma reconnaissance aux chercheurs Grenoblois pour leur sympathie qui m'a beaucoup soutenue dans mon début de séjour en France, notamment Sergio Loureiro, Lionel Marques, M. Roger Arnaud, M. J.J. Capponi, M. J.L. Tholence, et aussi l'ensemble des membres du club CAESUG Ski. Merci à tous.

# Chapter 1

# Introduction

Les propriétés physiques dans les nanostructures supraconductrices ont suscité un grand intérêt ces dernières années - partiellement motivé par le dévelopement des techniques de nanofabrication aussi bien du point de vue de l'expérience que de la théorie. Le contrôle des dimensions de l'échantillon qui deviennent comparables aux longueurs caractéristiques des matériaux supraconducteurs, la longueur de cohérence et la profondeur de pénétration, donnent la possibilité d'imposer un confinement de la fonction d'onde du supraconducteur. Dans le cas particulier des réseaux supraconducteurs, de nouveaux phénomènes physiques apparaîssent à cause des effets dûs à la compétition entre le champ magnétique et la géométrie. En particulier, les réseaux supraconducteurs à deux dimensions (2D) dans un champ transverse se sont avérés des systèmes de laboratoire idéaux pour étudier des phénomènes dûs à la combinaison de la topologie, la frustration ou même la nature des états électroniques. Le problème de la frustration joue un rôle central dans un vaste domaine de la physique de la matière condensée moderne, comme des verres de spin, des quasicristaux, ou simplement le modèle XY. Dans les réseaux supraconducteurs 2D, la frustration peut être introduite par le champ magnétique appliqué et se définit simplement comme le flux magnétique réduit par plaquette du réseau, $f = \phi/\phi_0$, ou $\phi_0 = h/2e$ est le quanta du flux supraconducteur. Il est alors une variable facile à modifier, permettant d'étudier des effets de la frustration dans une grand variété de topologies, des structures périodiques aux structures fractales. Les réseaux de jonctions Josephson représentent la réalisation du modèle XY frustré en 2D et ils ont été largement utilisés

pour des études de transition de phase dans ces systèmes. Les réseaux supraconducteurs de fils ont été largement utilisés comme systèmes modèles dans l'étude des états d'électrons en liaison forte, confinés dans un potentiel modulé. La connection entre ces deux champs a été possible grace à la description de Ginzburg-Landau (linéarisée), developpée par Alexander pour des réseaux de fils. Ce formalisme permet une description du réseau dans un modèle de liaison forte et offre la possibilité d'analyser quelques particularités du spectre d'une particule dans ce modèle.

Dans cette thèse nous présentons une étude de phénomènes de localisation induits par des champs magnétiques dans des systèmes supraconducteurs.

Dans une première partie, nous traiterons un problème d'interaction entre des états de bord supraconducteurs dans les réseaux de trous. Ces états sont localisés autour des bords de trous par les effets de supraconductivité de surface.

Dans une deuxième partie, nous étudions un effet de localisation particulier, qui résulte des interférences quantiques du type Aharonov-Bohm dans un réseau périodique. C'est la combinaison entre la topologie du réseau et le déphasage de la fonction d'onde supraconductrice induit par le champ appliqué, qui est dans ce cas l'origine du phenomène. Nous montrons que, quand le flux par cellule est égal à un demi quanta de flux, le comportement du réseau est similaire à celui d'une boucle fermée isolée.

Nous avons utilisé des réseaux fabriqués à partir de matériaux supraconducteurs à basse température de transition, Aluminium et Niobium, pour lesquels les techniques de nanofabrications sont bien établies. L'Aluminium est bien adapté à l'étude des phenomènes dont l'amplitude dépend du rapport entre la longueur de cohérence et du paramètre de maille. La grande longueur de cohérence de l'Aluminium permet la fabrication de réseaux avec un paramètre de maille de l'ordre de quelques $\mu$m pour lequel des phenomèmes comme la nature oscillatoire de la température de transition dans un champ magnétique peuvent être observés facilement. De telles dimensions peuvent être facilement réalisées avec les méthodes de lithographie. La décoration de Bitter est réalisée sur des échantillons de Niobiumà 4.2 K. L'Aluminium ne peut pas être utilisé à cause de sa basse température de transition, par contre le Niobium est bien adapté avec sa température de transition d'environ 9.2 K. De plus, les distributions de vortex dans un film supraconducteur peuvent être fortement influencées

par des inhomogenéités de l'échantillon et des films minces de très haute qualité sont donc nécessaires. Pour cette raison nous avons utilisé seulement des films minces de Niobium épitaxiés.

Le manuscrit est organisé de la façon suivante:

Les détails concernant la nanolithographie sont décrits dans le Chapitre 2. En particulier, nous décrivons un procédé à trois couches pour la lithographie *Deep-UV* developpé pour le *lift-off* des réseaux étendus dans l'Aluminium. Les techniques de mesures de transport et de décoration Bitter, sont décrites dans le Chapitre 3.

Dans le chapiter 4, nous présentons une étude sur l'interaction entre les états de bords localisés dans un réseau carré de trous. Ce travail poursuit un travail précédent réalisé par A. Bezryadin au sujet des vortex multiquanta, piégés par les trous. Ici, nous étudierons la nature des interactions à bas champs. Nous montrerons que les interactions sont du type de celles des réseaux de fils quand la distance entre les trous est inférieure à la longueur de cohérence. Une comparaison avec la théorie montrera que le passage à un régime de trous isolés avec l'augmentation du champ est dû à une transformation des conditions aux limites aux bords des trous. Nous montrerons que, dans les réseaux dilués, les interactions sont mieux décrites par un couplage faible. Un modèle simple, proposé par R. Fazio, décrivant ce régime est présenté.

Dans le chapitre 5, une étude expérimentale d'un nouveau phénomène de localisation est présentée. Ce phénomène est induit par un champ magnétique dans des réseaux 2D périodiques avec une géométrie particulière (géométrie d'étoile). Le nouvel aspect de ce phénomène est que les interférences quantiques totalement destructives se produisent quand le flux par cellule de réseau est égal à la moitié d'un quantum de flux. Dans ce cas, la propagation d'un paquet d'onde est confinée dans des cages dites d'Aharonov Bohm. Notre approche expérimentale consiste à étudier la ligne de transition, le courant critique et les configurations de vortex dans des réseaux de fils supraconducteurs à géométrie d'étoile. Un aspect important est que ce phénomène semble être très sensible au désordre aléatoire qui peut détruire totalement l'effet d'interférence. Nous avons donc utilisé, dans nos mesures de transport, des réseaux de fils supraconducteurs de très haute qualité géométrique. La lithographie de ces échantillons a été réalisée au CEA-LETI. Les résultats expérimentaux obtenus par

ces mesures de transport sont comparés à la théorie, en utilisant l'adaptation de la description linéaire de Ginsburg-Landau d'un réseau de fils dans le modèle de liaisons fortes. Nous verrons qu'un très bon accord quantitatif entre la ligne de transition et la théorie peut être obtenu. Un bon accord qualitatif pour le courant critique est aussi obtenu, bien que l'approche linéaire de Ginzburg-Landau utilisée soit une trop forte approximation. Le fait de considérer des termes non linéaires dans la topologie complexe d'un réseau infini est cependant un problème très complexe qui reste à résoudre.

Les configurations de vortex à plusieurs frustrations ont aussi été étudiées par la décoration de Bitter. De ces expériences, nous essayerons de montrer que la distribution des vortex au demi-flux est très désordonnée, ceci étant dû à la dégénéresence infinie attendue pour cette valeur de flux.

Enfin, nous présenterons au chapitre 6 un travail préliminaire dans le but d'optimiser la technique de Bitter pour des expériences de quenching sur des systèmes supraconducteurs bidimensionnels. Une brève description du phénomène qui a motivé ce travail est présentée et sera l'objet de futurs développements.

# Chapter 2

# Nanofabrication Techniques

Les techniques de nanofabrication utilisées dans l'élaboration des échantillons submicroniques sont décrites ici. Le choix des procédés a été déterminé par divers facteurs: la taille et la géométrie des échantillons adaptés aux types de mesures, les métaux évaporés et bien sûr les techniques disponibles. Dans la plupart des cas, l'équipement disponible au sein du laboratoire était suffisant pour satisfaire les propriétés indispensables de nos échantillons. Pour cela, on a disposé de méthodes de lithographie électronique au MEB et de photolithographie en ultraviolet profond (DUV) pour l'insolation des couches de résine positive PMMA. Pour cette dernière méthode, un procédé de tri-couche pour le *lift-off* de l'aluminium a été optimisé visant l'obtention d'un bon profil des motifs de l'ordre du micron sur une surface de un $cm^2$. Les méthodes de transferts choisies ont été la gravure RIE pour graver des couches de niobium et la technique de *lift-off* pour l'aluminium. Pour les échantillons à géométrie d'étoile utilisées dans les expériences sur les cages d'Aharonov-Bohm, il nous fallait, à la fois une résolution submicronique, une homogéneité et une parfaite isotropie sur les surfaces de l'ordre du millimètre, ce qui a nécessité l'accès à un masqueur électronique très performant. Nous avons pu profiter des équipements de lithographie et des équipes de travail du CEA-LETI de Grenoble dans le cadre du programme PLATO, *Silicium nanostructuré pour la physique.*

# Introduction

The principle of lithography lies in writing a given pattern on a sensitive medium which is able to sustain the transfer process of the recorded pattern to the final sample. In this chapter we describe the nanofabrication techniques used in the preparation of the superconducting arrays and networks studied in chapters 4 and 5. Since the studied physical phenomena involves the interplay between the applied magnetic field and the samples topology, the arrays must be very homogeneous and isotropic, with well defined shaped patterns over a large surface. The choice of the patterning procedure was decided on the basis of several factors: the type of measurement to be performed, the available patterning techniques, and the compromise between total surface and resolution of the individual pattern elements. In general, most of the fabrication steps were carried out with the equipment and techniques available in C.R.T.B.T.. As exposure methods we used *e-beam* lithography and *DUV* photolithography on positive PMMA resist. For the patterning transfer, we used reactive ion etching for the niobium films and the *lift-off* technique for the aluminium samples. For all our samples we used superconducting metals of low transition temperature, aluminium and niobium, which were deposited on oxide silicon or sapphire substrates, respectively, by thermal evaporation in Ultra High Vacuum conditions.

For the square array of holes studied in chapter 4 we developed a tri-layer process for *DUV* photolithography and lift-off of aluminium, in order to improve the holes profile from the one obtained by lift-off using the monolayer process.

In the study of the localization phenomena presented in Chap. 5, we fabricated wire networks with the STAR geometry on aluminium and niobium. For the samples used in the transport measurements, we chose aluminium for several reasons. First of all, the amplitude of some phenomena we studied is proportional to the ratio $\xi(0)/a$, where $a$ is the network lattice constant and $\xi(0)$ the temperature dependent coherence length. We also need a two-dimensional network, that is, with wire width much larger than $\xi(T)$, on a wide temperature regime. Given the coherence length of our aluminium films, $\xi(0) = 0.2\ \mu$m, we can design networks which fulfill these requirements and using regular nanofabrication techniques. Aluminium is very suitable for $lift-off$ of extended networks ($\approx 1\ \text{mm}^2$) with a high precision of wire thickness

($\approx$ 1 nm). Moreover, its low zero field transition temperature, of about 1.25 K, is well adapted to the optimum temperature range of our cryostat. The alignment requirements for the lithography of these networks, micron-size cells of 100 nm width wires over a 1 mm$^2$ surface, were beyond the limits of our *e-beam* microscope. Therefore, the lithography was performed using the nanofabrication facilities and working teams of CEA-LETI.

The wire networks used in the decoration experiments were made from epitaxial niobium films. In this case we used niobium since we needed samples with a transition temperature higher than the 4.2 K at which the decoration experiments are performed. The lithography was performed with our *e-beam* microscope. We tried to obtain isotropic networks, with 0.3 $\mu$m wire width over a total surface of the order of 100 $\times$ 100 $\mu$m$^2$ (about 1000 cells). However, we observed that we couldn't obtain a good alignment of successive pattern rows due a mechanical deflection of the microscope *e-beam*. We were thus constricted to use smaller networks, below 80 $\times$ 80 $\mu$m$^2$ total surface, for which this effect is negligible.

The organization of this chapter is as follows: on the next sections we describe the exposure methods we used, *e-beam* lithography and photolithography in deep-ultraviolet. On section 2.2 are briefly described the characteristics of the used resist and in section 2.3 the characteristics of our metallic films. Finally, on section 2.4 we describe the *lift-off* and reactive ion etching (RIE) processes. In this section are also given the nanofabrication details for each of the studied samples. We decided to group all the aluminium samples in the *lift-off* subsection and the niobium samples in the RIE subsection, respectively, since these are the processes which transfer the pattern from the mask to the metal film. All technical data concerning the preparation of each sample is given at the end of the chapter. We used the general references (Refs. [1, 2, 3, 4]).

## 2.1 Exposure Methods

We used as exposure methods *Deep Ultra-Violet* (DUV) photolithography and electron beam (*e-beam*) lithography. The choice depends on the sample requirements,

since both methods present advantages and disadvantages. DUV photolithography offers sub-micron resolution over a large surface (1 $cm^2$) and short exposition times, ranging from a few seconds to a dozen minutes, depending on the resist and pattern. However, it requires the use of exposition masks, which makes it a less flexible and more expensive technique than *e-beam* lithography, at least for our laboratory purposes. In contrast, *e-beam* lithography offers a great flexibility in the pattern conception and design, with an excellent scale resolution ($\approx$ 20 nm with PMMA resist), which can be however compromised if extended patterned surfaces are required.

The total surface of the arrays and networks used on the transport measurements ranged from $0.1 \times 0.1$ $mm^2$ to 1 $cm^2$. Such extended surfaces are needed since these measurements were performed close to the superconductor phase transition, and are therefore sensitive to finite size effects or the placement of the probe contacts. For the array of micron-size holes we used (DUV) photolithography since this method offers the required resolution over a large patterned surface of 1 $cm^2$. For the Star networks we needed very isotropic networks, with a sub-micron resolution on the wires and over a surface of the order of 1 mm2. Such requirements are well beyond the possibilities of our *e-beam* microscope or the (DUV) photolithography. Therefore, the lithography was performed using an *e-beam* writer at the CEA-LETI facilities.

For the samples used in the decoration experiments, we performed *e-beam* lithography with a scanning electron microscope, which allows a good flexibility in the pattern design. For this type of experiments a total surface of 50 $\mu$m side length and wire widths of the order of 0.3$\mu$m is often sufficient, which can be easily reached by this method.

On the following we describe each of this exposure methods.

### Electron-beam lithography

In electronic lithography, a resist layer is exposed to the electron beam whose position and incidence time is controlled by computer in order to deliver a fixed exposure dose per patterned unit surface. We used a Scanning Electron Microscope Cambridge S240, with a maximum electron acceleration of 30 kV and an electron beam current of the order of 0.1 nA, with typical exposure doses for PMMA resists of 120 $\mu C/cm^2$.

In the case of electron beam lithography the resolution limits are set not by the beam diameter ($\approx$ 2 nm) but by the resist exposure to backscattered electrons from the sample substrate and/or to secondary electrons, arising from scattering events inside the resist layer. These effects expose undesirable areas of the resist layer (proximity effect) and limit the pattern resolution, being particularly important in extended patterns. This effect can be minimized by adjusting the exposition doses and/or by decomposition of the pattern elements.

### Deep-UV lithography

The DUV lithography is performed using a Karl Suss MJB 3 UV 250 sub-micron mask aligner, equipped with a 275 W Hg/Xe lamp of 240 - 260 nm wavelength. The attained resolution is thus 0.3 $\mu$m in optimum conditions. This mask aligner allows the manipulation of substrates wafers of different shapes and thickness, up to 3" diameter substrates. It is also equipped with an alignment microscope which allows a visual alignment between the substrate and the mask. A relative displacement in X,Y directions can be done by two alignment micrometers.

We used high-precision quartz masks with different chromium patterns defined over a 1 cm$^2$ surface[1]. Before exposure, the mask is thoroughly cleaned with distilled water and rinsed with isopropanol. It is then fixed on the mask holder.

Three exposure modes are available, which vary in the contact strength between the mask and the resist coated wafer: soft and hard contact, with which a resolution of 1.5 $\mu$m and above can be achieved, and vacuum contact. In the soft contact, a vacuum is created below the substrate which is pressed against the mask by mechanical contact only. In the hard contact mode, compressed nitrogen gas is used, whose pressure can be regulated (from 0 to 1 bar) to adjust the contact strength. In the vacuum contact mode, a vacuum is created between the substrate and the mask with the help of a vacuum chamber. The highest resolution is attained in this mode because then the space between substrate and mask is reduced to its minimum, being just limited by the substrate roughness, dust particles, etc. For this reason, this mode is more susceptible to substrate imperfections than the others, requiring a special care to

[1] 2 1/2 quartz plate fabricated by CSEM, Neuchâtel, Switzerland

avoid surface contamination which may lead to an heterogeneous resist exposure.

## 2.2 The recording medium

A suitable recording medium for electron and photon lithography are resist materials. In our case, we used polymer solutions whose solvability in a resist solvent increases (positive resist) or decreases (negative resist) in the exposed areas.

The resist is applied over the substrate wafer and spin at a constant angular speed $w$ during a fixed time interval (usually 30 seconds). The wafer is then baked at a constant temperature T= 160 °C during 5 minutes to dry out the solvent. The result is a thin, homogeneous resist film. The final thickness of this layer is determined by the characteristics of the polymer solution (molecular weight, concentration, viscosity,...) and the rotation speed $w$. For a given solution, the layer thickness varies with $w$ approximately as $1/\sqrt{w}$. Since the angular speed of our spin-coating device can only be varied between 1000 and 8000 rotations per minute (rpm), a wider resist thickness range is attained using resist solutions of different concentrations. The resist we mostly used was polymethyl methacrylate (PMMA) (dissolved at different concentrations in chlorobenzene) or co-polymer resists for which a thickness range from 100 to 400 nm can be attained, suitable to our applications.

## 2.3 Thermal evaporation of metals

All metallic films are deposited by thermal evaporation on a Ultra High Vacuum (UHV) Riber chamber. The samples are first introduced in a load lock and transferred into the UHV chamber when the load lock pressure attains $3\times10^{-7}$ mbar. After each venting of the UHV chamber for maintenance, the whole ensemble is baked at 250 °C during 48 hours. These procedures help to maintain within the UHV chamber a base vacuum pressure of $10^{-10}$ mbar, obtained with an ionic pump assisted by a titanium sublimator. During metal evaporation the pressure raises to a few $10^{-9}$ mbar.

Metallic charges of very pure metals (Nb, Si, Al, Au, Cu) are available inside the chamber and placed in a massive copper support, which is water cooled in order to avoid charge contamination. The metal thermal evaporation is induced by an

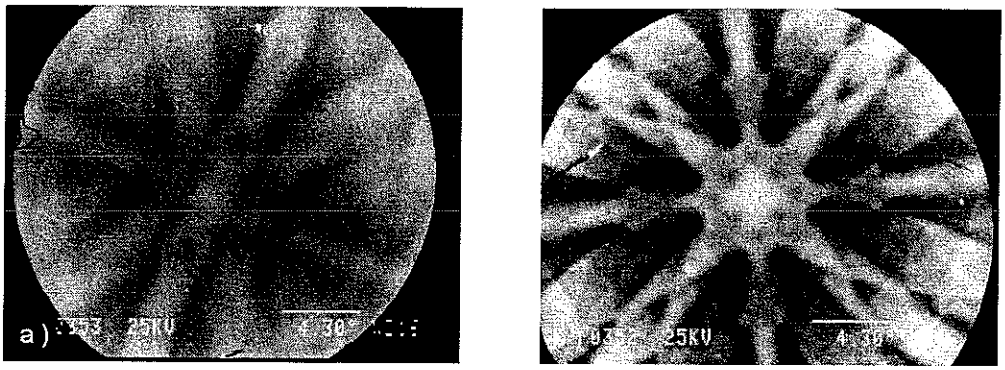


Figure 2.1: Pseudo Kikushi lines of Nb films grown on sapphire substrates with orientation: a) (1,1,-2,0) and b) (1,-1,0,2). The film grown on the (1,-1,0,2) substrate has a better epitaxy. (SEM micrograph, Laboratoire de Cristallographie - CNRS).

electron beam which is focused on the metallic charge by two small induction coils which deflect the beam (current intensity of about 150 mA and an acceleration voltage of 10 kV). The deposition rates depend on the evaporated metal, ranging from 1 to 10 Å/s.

### 2.3.1 Characteristics of the metallic films

The niobium films are deposited on sapphire substrates heated at a temperature of a 550 °C, which enables the growth of epitaxial films of high quality. Sapphire substrates with the crystal orientations (1,-1,0,2) and (1,1,-2,0) were used to test its influence in the film epitaxy. The epitaxy of the grown Nb films was characterized by the pseudo Kikushi lines method, revealing an epitaxy in the (100) direction for both substrates but with best results for the (1,-1,0,2) orientation. This method relies in the variation of the electrons absorption inside a crystal with the propagation direction. When close to a Bragg plane, there is an anomalous absorption which changes the retrodiffusion coefficient. Therefore, if the sample is observed by SEM at weak amplification, and the electron beam direction is displaced by small angles, several families of Bragg plans will be probed. For a well oriented crystal, a structure of lines, the pseudo Kikushi lines, with an arrangement related to the crystal orientations will appear, superposed over the sample image. The lines symmetry reflect the crystal symmetry, while deformations produce a distortion of the Kikushi lines.

The SEM images obtained for 200 nm thickness Nb films grown with different sapphire substrates are presented in Fig. 2.1. For both substrates an image of structured lines is obtained, indicating that both films are oriented in the (100) direction, however lines are better defined for the (1,-1,0,2) sapphire orientation indicating a better epitaxy with this substrate. This result is confirmed by the residual resistivity ratios, which are 35 for the Nb film with sapphire substrate (1,-1,0,2) in contrast to 25 for sapphire (1,1,-2,0).

| Film | thickness [nm] | RRR | $T_c(0)$ [K] | $\Delta T$ [mK] | $\xi(0)$ [nm] | $\lambda(0)$ [nm] |
|---|---|---|---|---|---|---|
| Nb | 200 | 35 | 9.2 | 3 | 20 | 100 |
| Al | 80 | 5 | 1.25 | 3 | 250 | 170 |

Table 2.1: Typical parameters of the aluminium and epitaxial niobium films.

The aluminium films are deposited at room temperature on a single crystal silicon substrate, resulting on non-oriented films.

Some typical parameters of the niobium and aluminium films are summarized in Table 2.1. The coherence length is estimated from the slope of the upper critical field as a function of temperature $H_{c2} = (\Phi_o/2\pi\xi^2(0))(1 - T/T_c)$. The penetration depth $\lambda(0)$ of the Nb films was determined from measurements of the reflection coefficient at 1 GHz frequency of a Nb stripe in short-circuit at the end of a coaxed cable [5]. For the Al films the penetration depth is obtained using the dirty limit relations $l_{el} = \xi(0)/0.852\sqrt{\xi_o})^2 \approx 54$ nm and $\lambda(0) = 0.64\lambda_o\sqrt{\xi_o/l_{el}} \approx 170$ nm, using the values $\xi_o = 1600$ nm and $\lambda_o = 50$ nm for pure Al. The effective penetration depth for a film of thickness $d$ smaller than $\lambda(0)$ is thus obtained from $\lambda_{eff} = \lambda^2(0)/d$.

## 2.4 Patterning Transfer Processes

In this section we describe the patterning processes used for each of the samples in more detail. On a first part we will describe those patterned by *lift-off* and on a second part the array patterned using Reactive Ion Etching.

### 2.4.1 The Lift-off Process

We used *lift-off* processes with PMMA resist for the patterning of aluminium samples or in the fabrication of the aluminium masks used in plasma etching or pattern inversion. *Lift-off* is an additive transfer process that makes use of a resist deposition mask. The metal film is deposited on the substrate through this mask, which will be dissolved on a appropriate solvent, removing both the resist and the metal deposited on the top of it. This process present some advantages over subtractive methods, such as etching. It allows the patterning of soft metal films not easily etched by anisotropic plasma and it does not lead to a lost of profile definition such as isotropic etching does.

For a successful *lift-off* over a single resist layer, this one must fulfill certain requirements:

i) the resist layer must be thicker than the metal layer to ensure discontinuity between the metal deposited over the substrate and on the top of the resist, respectively. In the case of angle evaporation, special attention is needed to avoid deposition on the resist walls.

ii) During metal evaporation the resist temperature must not exceed its glass transition temperature, above which the resist flows, causing distortion of the pattern profiles.

iii) After development the resist must have undercut profile. This profile is due to the *pear-shape* of the resist energy absorption profile, which is developed at high electron doses due to proximity effects. As long as the profile at the surface is not affected, since the metal passes through the small open areas in the top, there is no loss of pattern resolution and profile broadening in the bottom helps the removing process.

PMMA resist is widely used on metal films patterning since it fulfills most of these requirements. In contrast to PMMA, co-polymers of PMMA have higher sensitivity but is difficult to obtain undercut profiles suitable for *lift-off* by a mono-layer process. One limitation of PMMA resist is that it cannot sustain thermal evaporation of refractive metals such as niobium, due to its glass transition temperature of 120 °C, which is however adapted for the evaporation of aluminium or silicon.

On the next subsections we describe the technical details of the aluminium samples patterned by this method.

#### 2.4.1.1 STAR aluminium wire networks

These arrays were used in the transport measurements presented in Chap. 5. The lithography of the wire superconducting networks with STAR geometry were performed at LETI (CEA-Grenoble) using an e-beam writer LEICA VB6-HR. These networks are constituted by rhombus cells of 1 $\mu$m side wire length and wire width of 100 nm. The large networks surfaces ($0.6 \times 1$ mm$^2$ and $0.02 \times 1$ mm$^2$) are patterned by aligning writing fields of $200 \times 200$ $\mu$m$^2$. Patterned strips were also defined at each side of the array sample, though disconnected from it, for correction of proximity effects during the lithography exposure. In this way, the pattern at the array edges is exposed to the same dose as in the array center, thus ensuring a good wire uniformity through all the array surface.

The patterning is defined on a 600 nm thick positive resist mono-layer of SHIPLEY UV3. The exposure dose is 7 $\mu$C/cm$^2$ for an acceleration voltage of 50 kV. After development, a 100 nm layer of pure aluminium is evaporated in our UHV deposition chamber and *lifted-off* in a solvent POSITRIP EKC 830 (2-(2-aminoethoxy) ethanol solution) during 20 minutes. The main steps are illustrated in Fig. 2.2.

#### 2.4.1.2 Square array of micron size holes in aluminium

These arrays were studied in Chap. 4. We used DUV lithography since we needed a large array surface (of the order of 1 cm$^2$) to avoid parasitic short circuits from surface superconductivity at the sample edges. The exposure was done on PMMA resist layer (240 nm thickness) using a high precision chromium mask of a $1 \times 1$ cm$^2$ square array of chromium squares, with side length of 2 $\mu$m and 4 $\mu$m of lattice constant. It was found to be very difficult to obtain an excellent development of the PMMA resist mono-layer. It required a long exposition time of 12 minutes (in comparison with a few seconds for negative resists), resulting in a lost of contrast and pattern definition since the process becomes more sensible to defects in the resist layer, mechanical vibrations during exposure, etc. After development, pure aluminium is evaporated

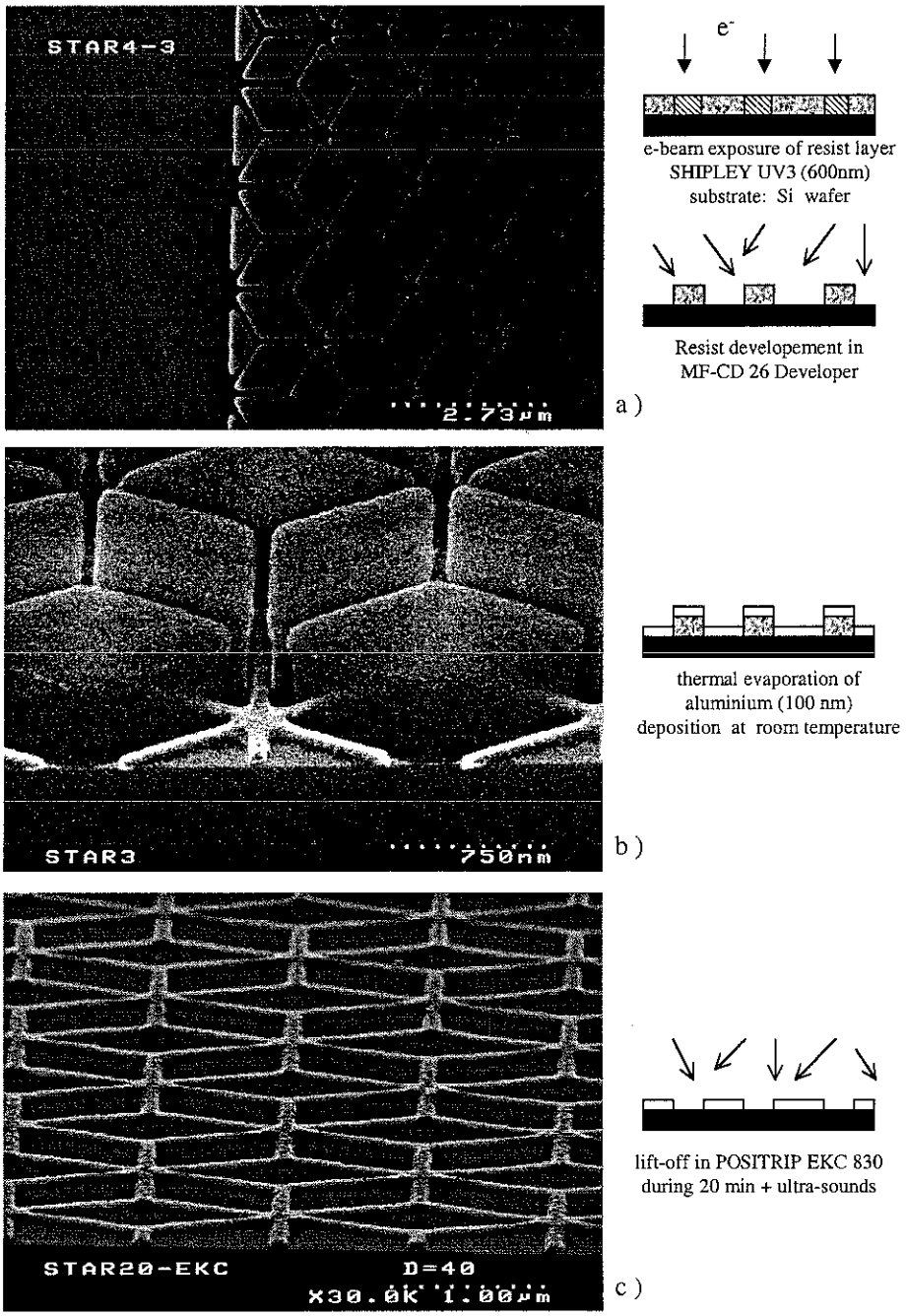


Figure 2.2: Illustration of the different patterning steps of the STAR Al wire networks. a) pattern close to the future current contact pad after development of the resist; b) aluminium wires after thermal evaporation before lifting, the resist blocks are still present; c) network after the *lift-off*.

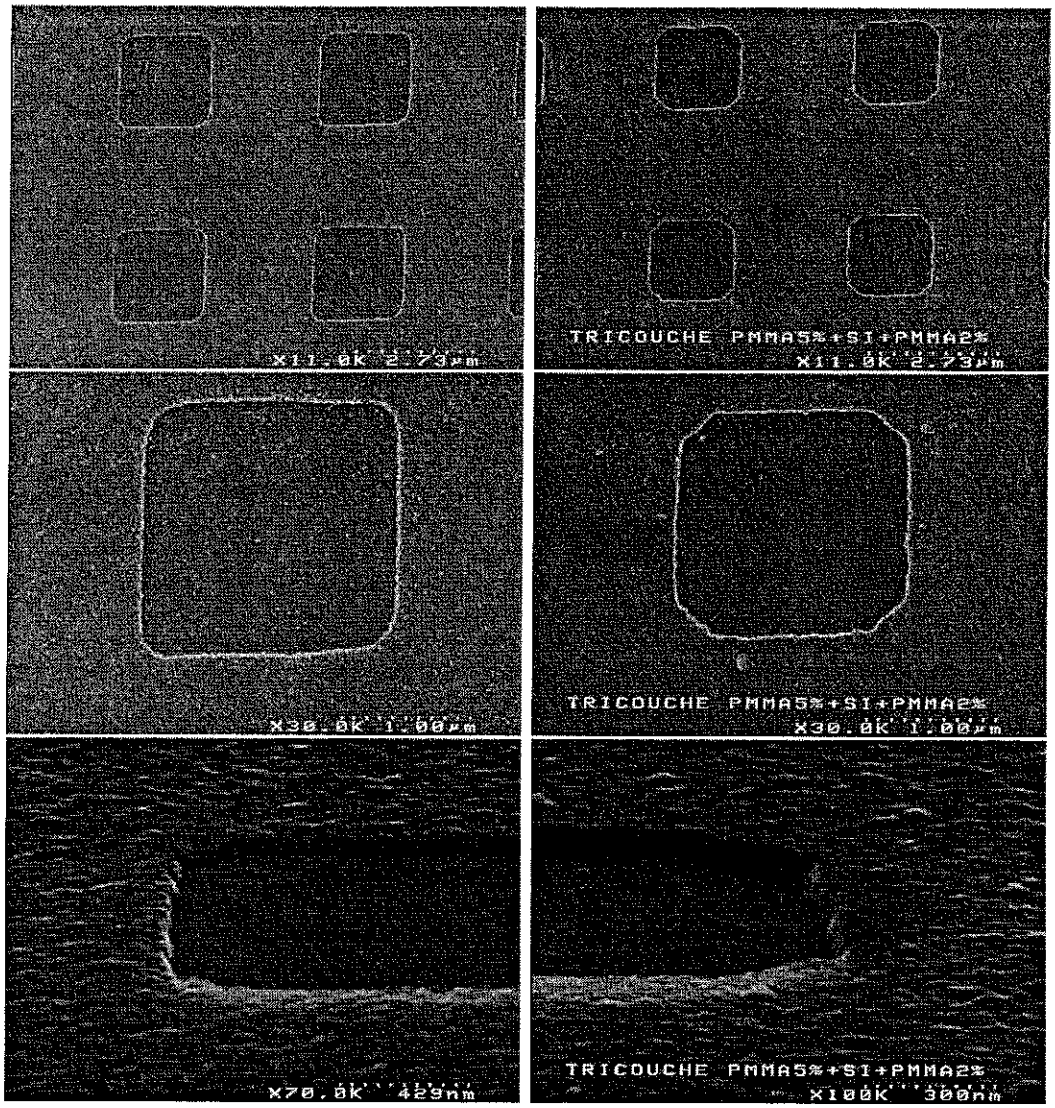


Figure 2.3: Comparison of the hole definition using the mono-layer (left column) and the tri-layer (right column) processes; the tri-layer process provides of better definition of the square holes, with excellent replica of the mask shape.

(80 nm thickness) over the resist mask and then *lifted.*

In order to improve the definition of the square holes edges a tri-layer process for *DUV* was developed. In this process, we have a thin silicon metal layer (45 nm) between two PMMA resist layers. The top resist layer is exposed to *DUV* and developed. The intermediate Si layer is then etched through the resist mask by Reactive Ion Etching (RIE) with $SF_6$. The bottom resist layer is then etched with $O_2$ (RIE). Aluminium is then evaporated over this suspended metal mask.

A comparison between the hole edges definition obtained by the mono-layer and the tri-layer processes is illustrated on Fig. 2.3. We found that, the edges shape and sharpness obtained by the tri-layer process is better. However, given the sensitivity of photolithography to surface contamination and the complexity of the tri-layer process, it is more difficult to attain an homogeneous development over the total surface by this method in comparison to the mono-layer process.

### 2.4.2 Subtractive process by dry etching

The niobium samples were essentially patterned using dry etching. On one hand, because niobium is a refractory metal it cannot be evaporated over polymer resist masks such as PMMA. *Lift-off* processes for Niobium using other resists such as victrex [6] have been developed, however for our decoration experiments we need epitaxial niobium films of high quality, which require deposition over heated sapphire substrates, and a Nb bottom layer to improve the image contrast, which is obtained from incomplete etch of the Nb film.

The preferred etching process was the *Reactive Ion Etching* (RIE) due to its both high chemical selectivity and attack anisotropy. Moreover, the RIE plasma parameters (power, pressure, gas flow and composition) are optimized so that the etch rate of the different metals and resists is well controlled. We can thus etch completely or just a given thickness of the metal layer. The depth of attack is chosen by fixing the RIE time.

All niobium samples are patterned on epitaxial films of high quality (see section 2.3) which are covered by a protective Si layer of 5 nm. The Nb films are coated with a positive resist PMMA layer which is *e-beam* lithographed. After development, the

resist mask can be used directly for etching or to fabricate an metal mask by *lift-off*. For pattern elements of a few micron size, such as holes, loops, the pattern transfer was done directly with the mono-layer resist mask, by RIE etching with $SF_6$. One of these arrays is illustrated in Fig. 2.4 (left image). However since resists are also slightly etched by the $SF_6$ plasma, they are not suitable as patterning masks when a good definition of the pattern elements is needed (for *eg.*, below one micron), such as in thin wire networks. In these cases, a metallic Al mask is used, since the Al is not attacked during the Nb etching, as resists are, leading to a better edge definition.

**Description of the $SF_6$ RIE process**

The reactive ion etching is performed in a MG 200 PLASSYS system. It combines a reactive gas (such as $SF_6$) and a RF plasma (13 MHz) which produce very reactive ions that attack the metal surfaces not protected by a resist layer. The speed of attack (defined as the removed thickness per second) can be followed *in situ* by measure of the reflexivity or the interference of a laser incident in the sample surface. The parameters of a typical etching process with $SF_6$ are:

1. $2 \times 10^{-2}$ mbar gas pressure
2. gas flow of 20 scc/min
3. 20 W of discharge power

In this case the etching speed are typically 3 nm/s for Niobium and 5 nm/s for Silicon. The attack speed can be decreased without changing the RIE process by inserting a Si wafer inside the RIE chamber. The attack speed for Nb is then reduced to 1.3 nm/s, which may be interesting when attacking thin surfaces or for an incomplete etch. The use of the Si wafer also improves the attack anisotropy.

#### 2.4.2.1 STAR wire networks in epitaxial niobium

These networks were used on the decoration experiments described in Chap. 5. In these experiments we were studying the influence of the applied field and the network topology in the vortex distribution, therefore we tried to fabricate very isotropic

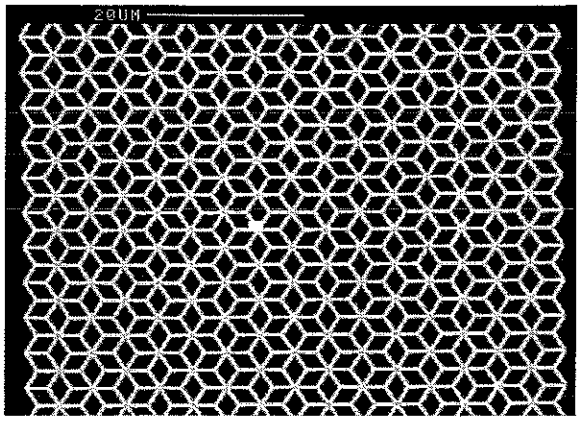


Figure 2.4: SEM micrographs of a wire network with the STAR geometry and an array of square loops in niobium. The *e-beam* lithography is performed using CRTBT SEM.

networks with uniform wires to avoid that geometric defects influence the vortex configurations.

Typical dimensions of these networks were a total surface of $50 \times 50$ $\mu m^2$, unit cells with side length varying between 1 to 3 $\mu$m and wire width of 0.3 $\mu$m. The dry etching is performed through an aluminium mask, fabricated by *lift-off*. This mask is not removed from the final sample since it does not affect the decoration results, and saves the sample from a processing step. A SEM micrograph of one of such networks is presented in Fig. 2.4.

The patterning was performed using *e-beam* lithography and the main difficulties we found were the broadening of the diagonal wires relative to the horizontal ones, as well as at the wires intersection, and a small misalignment of successive rows of pattern elements. The broadening problem is related with proximity effects and the pattern design itself, which can be reduced by coding the diagonal wires with less pixels than the horizontal ones and decomposing the crossing wires nodes in three trapezes shaped elements. A pattern element for the STAR design is displayed in Fig. 2.5a) as well as the decomposition elements. The pattern element repeated in the vertical direction was offset for clarity.

The non-alignment of successive rows of cells is related to the displacement of the *e-beam*. The whole pattern is defined by successive horizontal passages of the *e-beam* which repeats the pattern elements in successive vertical rows (see upper right

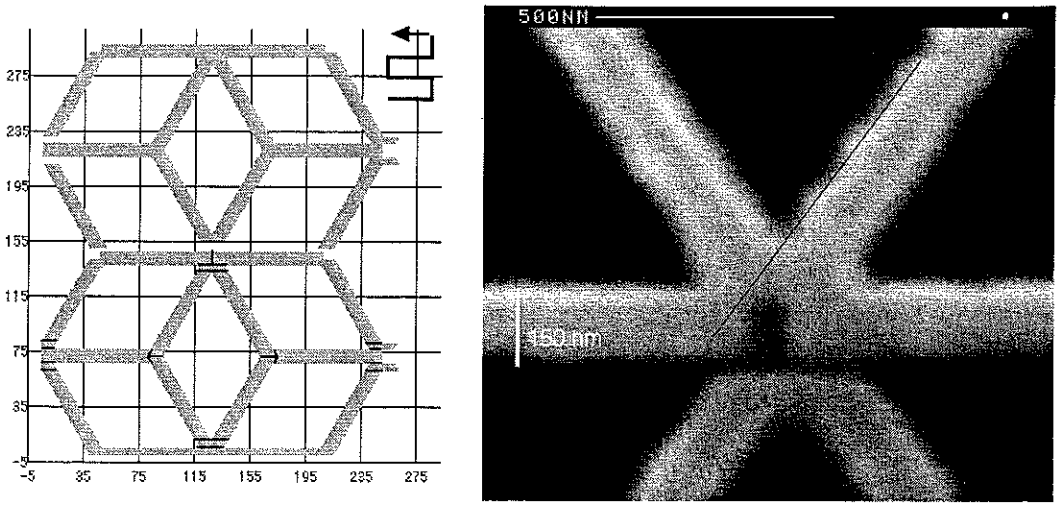


Figure 2.5: a) Two pattern elements for the design of the star network repeated in the vertical direction (coordinates are in pixels). The displacement of the *e-beam* during patterning is represented on the upper right corner. b) SEM micrograph of a two vertically juxtaposed element patterns of the STAR geometry. A clear misalignment between the diagonal wires can be observed. The solid line is a guide to the eye.

corner of Fig. 2.5a) ). When the *e-beam* total displacement for one row is too long ($\approx 100$ $\mu$m), the return to the origin is not well aligned with the previous one, resulting in a small misalignment of successive rows. This effect is illustrated in Fig. 2.5 near a 6-fold node of the network obtained by the intersection of two pattern elements designed in successive *e-beam* displacements. It is clearly seen that the upper right wire is not in the same diagonal as the lower left one. The black diagonal line is drawn as a guide to the eye. This micrograph is from a dose test sample defined on a $100 \times 100$ $\mu$m$^2$ surface (the separation of one pixel between some decomposition elements is visible).

We also observed that this misalignment effect is not reproducible and therefore, very difficult to compensate. For this reason, we only used wire networks with a total surfaces below $80 \times 80$ $\mu$m$^2$, for which the misalignment effect is negligible.

## 2.5 Concluding remarks

In this chapter were presented all the nanofabrication processes used in the fabrication of the samples discussed in this thesis. Most of them consisted on adaptations to our sample requirements of currently used processes. A trilayer process with *DUV* photolithography was optimized for lift-off of micron-size aluminium patterns. A special effort was developed to obtain epitaxial niobium wire networks with STAR geometry for magnetic decoration. Uniform networks with 200 nm wire width over a surface of $50 \times 50$ $\mu$m$^2$ were obtained by *e-beam* lithography with positive PMMA resist. Finally, we profited from the nanofabrication equipment and working teams of CEA-LETI (Grenoble) in the lithography of wire networks with the Star geometry.

# Technical details of the nanofabrication processes

### Lift-off process for Star wire networks in aluminium

1. positive resist SHIPLEY UV3 of 600 nm thickness
2. electron beam exposure: standard dose of 7 $\mu C/cm^2$ for an accelerating voltage of 50 kV
3. resist development: developed in a MF-CD 26 developer.
4. aluminium deposition: thermal evaporation of 100 nm Al layer at a deposition rate of 0.2 nm/s
5. aluminium *Lift-off*: POSITRIP EKC 830 during 20 min.

### Processes for the square arrays of holes in aluminium

### Positive resist monolayer process for DUV

1. resist deposition:

   PMMA 2% resist layer (final thickness 240 nm) spin at w=2000 rpm during 30 seconds and baked at 165 °C during 5 minutes.

2. *DUV* exposure:

   exposed with a constant luminous intensity of 1.2 $mW/cm^2$ during 12 minutes.

3. resist development:

   developed in a solution of cellosolve and isopropanol (5:3) during one minute and rinse for one minute in isopropanol.

4. aluminium deposition:

   thermal evaporation of 80 nm Al layer at a deposition rate of 0.2 nm/s

5. aluminium *Lift-off*:

   Lifted in cellosove acetate at 65 °C during 20 minutes.

### Tri-layer process for DUV

1. bottom resist layer deposition:

   PMMA 5% resist layer (final thickness nm) spin at w=2000 rpm during 30 seconds and baked at 165 °C during 5 minutes.

2. intermediate silicon layer deposition:

   thermal evaporation of 45 nm Si layer at a deposition rate of 0.1 nm/s

3. second resist layer deposition:

   PMMA 2% resist layer (final thickness 240 nm) spin at w=2000 rpm during 30 seconds and baked at 120 °C during 7 minutes.

4. *DUV* exposure: exposed at a constant luminous intensity of 1.2 mw/cm$^2$ during 12 minutes.

5. top resist layer development:

   developed in a solution of cellosolve and isopropanol (5:3) during 1 minute and rinse for 1 minute in isopropanol.

6. dry etching:

   plasma etching of the silicon layer: $SF_6$ P=20 mW at a rate of 3 nm/s.
   plasma etching of the bottom resist layer: $O_2$ during 30 seconds

7. aluminium deposition:

   thermal evaporation of 80 nm Al layer at a deposition rate of 0.2 nm/s

8. aluminium *lift-off*: Lifted in cellosove acetate at 65 °C during 20 min.

### RIE patterning of Nb wire networks with an Al mask

1. Niobium epitaxial layer:

   thermal evaporation of a 200 nm niobium epitaxial layer on a sapphire (1,-1,0,2) substrate heated to 550 °C, followed by evaporation of a protective layer of silicon with 5 nm thickness.

2. resist deposition:

   PMMA 5% resist layer (final thickness nm) spin at w = 4000 rpm during 30 seconds and baked at 165 °C during 5 minutes.

3. electron beam exposure:

   standard dose of 120 $\mu C/cm^2$ for an accelerating voltage of 30 kV

4. resist development:

   1 minute in a solution of cellosolve and isopropanol (1:1) and rinse in isopropanol during 1 minute.

5. aluminium mask deposition:

   thermal evaporation of 30 nm Al layer at a deposition rate of 0.2 nm/s

6. aluminium *lift-off*:

   Lifted in cellosove acetate at 65 °C during 20 minutes.

7. dry etching:

   plasma etching of the niobium layer: $SF_6$ P=20 mW at a rate of 3 nm/s leaving a 50 nm bottom layer of niobium.

### RIE patterning of Nb arrays with a resist mask

1. Niobium epitaxial layer:

   thermal evaporation of a 200 nm niobium epitaxial layer on a sapphire (1,-1,0,2) substrate heated to 750 °C, followed by evaporation of a protective layer of silicon with 5 nm thickness.

2. resist deposition:

   PMMA 5% resist layer (final thickness nm) spin at w= 4000 rpm during 30 seconds and baked at 165 °C during 5 minutes.

3. electron beam exposure:

   standard dose of 120 $\mu C/cm^2$ for a accelerating voltage of 30 kV

4. resist development:

   1 minute in a solution of cellosolve and isopropanol (1:1) and rinse in isopropanol during one minute.

5. dry etching:

   plasma etching of the niobium layer: $SF_6$ P = 20 mW at a rate of 3 nm/s leaving a 50 nm bottom layer of niobium.

# Chapter 3

# Measurement Techniques

Dans ce chapitre sont présentés les détails concernant les techniques de mesures de transport et la méthode d'imagerie de vortex par décoration de Bitter. Les améliorations apportées y sont aussi présentées, à savoir, une brève description du logiciel développé pour l'automatisation des mesures de transport et l'application de réseaux de jonctions Josephson pour la détermination précise du zéro du champ magnétique effectif.

# Introduction

In this chapter we describe the techniques used in the transport measurements and the method of vortex imagery by Bitter decoration. Besides the general details concerning each technique, a more detailed description of the improvements is given. In the case of the transport measurements an elaborated software in C programming language was developed, which allowed the automatic control of applied field and temperature, as well as data acquisition during automatic sequences of increasing/decreasing temperature, field or current. A special routine for critical current measurements was also included. The condensation of $He^3$ is also automatically controlled. As for the Bitter decoration technique, the determination of the zero effective field with a good resolution (one Abrikosov vortex per $70 \times 70 \mu m^2$) now available by measuring the magnetoresistance of Josephson junction arrays before decoration. A characterization of the cooling rates attained in the decoration chamber was also performed, which is presented in chapter 6.

## 3.1 Transport Measurement

Our transport measurements consisted in the study of the samples resistance as a function of applied field, temperature, DC bias current, as well as in the study of the temperature and field dependence of the superconducting critical current. All samples studied by this technique were made of aluminium. We chose this material because of its large coherence length, of the order of 0.2 $\mu$m at zero temperature, which allows the fabrication of arrays with a two-dimensional behaviour for patterns sizes easily achieved by lithography. arrays with exhibit a two-dimensional behaviour since for this measurements we need large patterned arrays which can be done more easily by aluminium *lift-off*. Moreover, the critical temperature in zero field of about 1.26 K and the critical field at zero temperature less than 200 Oe, are well suited to the optimum working range of our $He^3$ cryostat. In fact, since most of the studied phenomena occur close to the normal-to-superconductor phase boundary, a high stability and resolution of both fields and temperature were required. For this reason, we used an $He^3$ cryostat which fulfills this requirements:

1. working temperature range from 0.3 K to 10 K, with a temperature stability better than 0.1 mK at 1 K

2. low residual field, $< 10$ mOe and resolution in the applied field better than 1 mOe

3. high resolution in the resistance measurement, of $10^{-5}$ of the resistance range at weak currents (20 nA - 100 $\mu$A)

### 3.1.1 Cryostat Description

The cryostat was fabricated in C.R.T.B.T. and makes use of both $He^4$ and $He^3$, contained in separate circuits. The minimum temperature achieved in the cryostat is 0.3 K. This temperature is attained by a $He^3$ condensation procedure: a small copper chamber (45 $cm^3$) placed inside the calorimeter is fed continuously through a thin capillary of liquid $He^4$ from the external bath at 4.2 K. This small chamber is pumped, decreasing the $He^4$ vapor pressure, and therefore the temperature of the contained liquid, down to 1.2 K. This container is surrounded by the $He^3$ condensation chamber, which is connected in a closed circuit to the $He^3$ gas reservoir. A pumping system based on active carbon is placed inside the condensation chamber, which at 1.2 K adsorbs the whole $He^3$ gas. By heating the carbon, the gas is desorbed and the $He^3$ condensation can be done follow according to the following computer controlled procedure:

1. the active carbon is heated during 10 minutes by feeding a current of 100 mA through a heating resistance placed in the carbon container. During this step, the carbon desorbs the $He^3$, increasing the $He^3$ gas pressure to about 300 mbar. When the $He^3$ vapour saturation pressure at 1.2 K is achieved, the gas condenses, filling the $He^3$ chamber of liquid $He^3$.

2. the carbon heating is stopped. While the carbon cools down, it adsorbs the $He^3$ gas, decreasing the pressure above the $He^3$ bath, and therefore decreasing its temperature to 0.3 K.

The autonomy of the cold point at 0.3 K depends on the working temperatures at the sample holder. It can vary from 3 hours at 1 K to 17 hours at 0.3 K.

#### Sample holder

The sample holder is a copper platform sustained by stainless steel tubes of low thermal conduction to the liquid $He^3$ container. The heat exchanges made through a thin copper wire are limited to 0.17 mW/K. The sample heating is done through a heating resistance installed in the sample holder and the temperature measured using a germanium thermometer. The thermometer resistance is measured by the 4-probe technique using a Barras Provence high resistance bridge, at a frequency of 33 Hz.

#### Field coil

The magnetic induction field is applied by a copper coil which surrounds the calorimeter, the current being fed by a current source. At the sample position the applied field as a function of applied current corresponds to 16.4 mT/A. Field inhomogeneities due to the coil finite size was reduced by extra spirals wounded at its extremities. The field homogeneity is then of 0.13% on a central cylindrical region of 3 mm diameter.

### 3.1.2 Resistance Measurement

The low temperature sample resistances must be measured with very small currents, of the order or less than a micro-Ampere, to avoid heating effects on the sample itself and limit the energies dissipated inside the calorimeter. The synchronous detection technique is suitable to the measurement of low resistance samples with weak measuring currents but with a high resolution. For these measurements we use a Barras Provence 4-probe resistance bridge. This bridge bias the sample with an *ac* current of 33 Hz frequency. The in-phase sample voltage signal is compared with a reference value, imposed manually by a decade inductive divider or by a software program through a programmable multiplier. The output signal is proportional to the difference between the sample resistance and the reference value. When these are the same, the bridge is compensated and the output signal is zero.

In the case of a measurement controlled by the software, the output tension signal is converted by an analog-digital converter and is sent to the computer. We use 16-bits converters which allow a resolution of 0.0015% (that is, 65536 levels) in the transmitted data. Using a simple calibrating procedure which is described in the next section (two signal readings at two different reference values), the resistance values are recovered from the tension signal. For low resistance bridges the calibration parameters change with temperature within a small temperature interval, such as 0.5 K, due to the high sensitivity of the measuring circuit . A calibration procedure at each temperature must be performed to obtain reproducible data readings.

### 3.1.3 Automatic data acquisition

Data acquisition and the control of the different parameters, applied field, DC current fed into the sample, temperature control, *etc*, can be done automatically by an elaborated program in C language which controls the different devices through an RS-232 and GPIB interfaces. The communication between the interface and the resistance bridges are done through programmable multipliers and the data reading is done using analog/digital converters.

In the following, we describe the main elements of this program in a user perspective. The program gives access to several menus which control several functions. Two of them are directly related to the measurement itself: the APPAREIL menu, which allows the control of each device separately, and the ACQUISITION menu, from which are launched the data acquisition sequences, as well as the routines for critical current measurements, automatic condensation of Helium 3, and data storing.

The program conception is *device oriented*, and to each device (for ex. a source current) has been attributed a window on which the several parameters can be changed (range, maximum current increments). They also allow an immediate assignment of some parameter or a data reading.

The main executable functions available are:

1. Temperature Control

   The temperature control is done through the resistance bridge using a programmable multiplier which replaces the analog inductive divider. When a

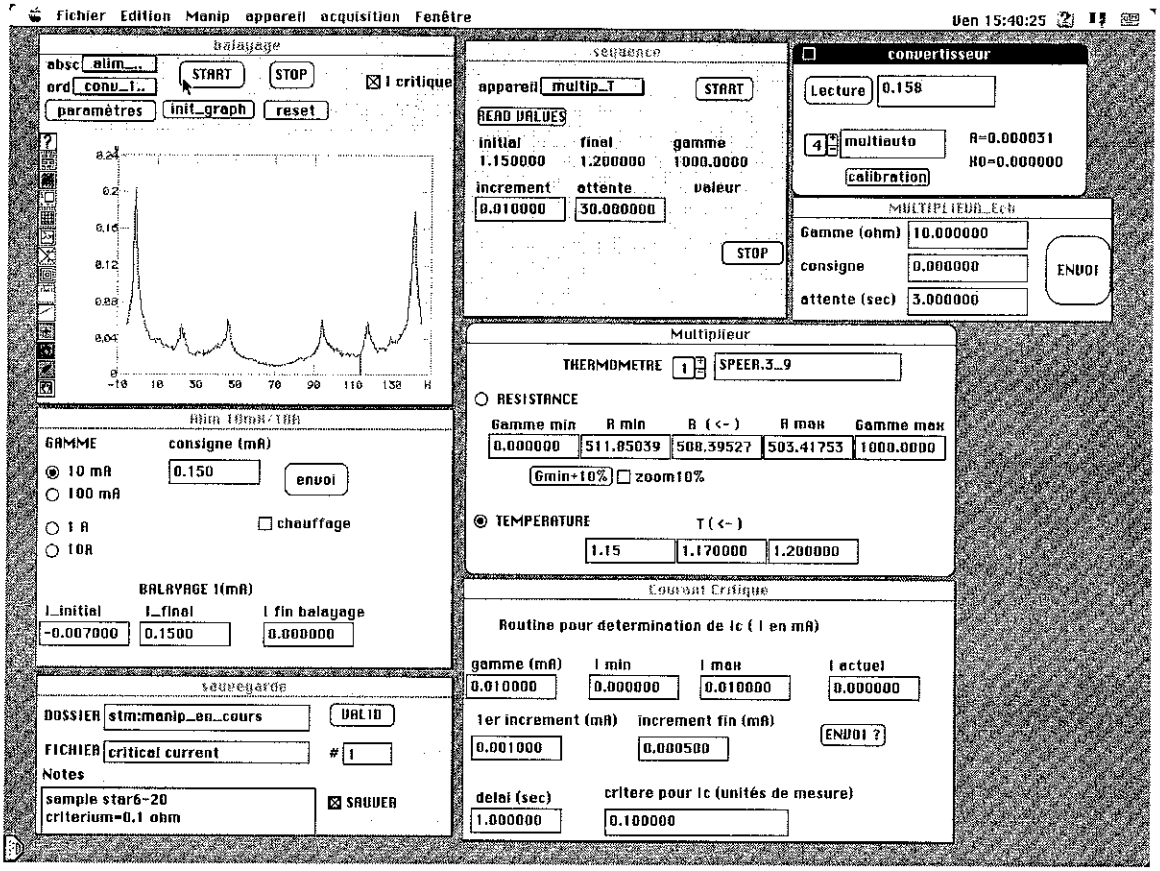


Figure 3.1: Active windows as seen on the computer screen during a measurement of critical current as a function of applied field.

target temperature is chosen, it is converted into a resistance value using a thermometer calibration table. This value is converted into a 16-bit digit and transmitted to the multiplier. We can also select a temperature range for data acquisition as a function of temperature.

2. Sample Measurement

The sample resistance is read using a 16-bit analog/digital converter connected to the in-phase output of the resistance bridge. The voltage signal is converted into a 16-bit signal, which is transmitted and converted into a voltage value by the program. The voltage output signal at the resistance bridge is independent of the resistance range, varying between 0 and 1. The voltage signal $V$ is converted into a resistance value $R$ by $R = a \times V + R_o$, where $a$ and $R_o$ are

calibration coefficients. These coefficients are calculated from two readings $V_1$ and $V_2$ performed at known resistance values $R_1$ and $R_2$, as $a = (V_2 - V_1)/(X_2 - X_1)$ and $R_o = 2(X_2 + X_1)/(V_2 + V_1)$. This calibration can be done at the beginning of one sequence or before each data reading.

3. Current Sources

   We use two different current sources: a 10 A for the external field and a 100 mA current source for the resistance measurements as a function of bias DC current. The corresponding windows allow the selection of the current source range, the assignment of an immediate current value or the definition of the current ranges used in the data acquisition as a function of applied field and/or current. The current increment can be chosen, in terms of fraction of range for the 100 mA current source or by a time delay for the 10 A current source.

The data acquisition sequences use the functions defined for the individual devices.

Data Acquisition Sequences:

1. Data acquisition as a function of one variable: time, field, temperature or dc current, while the other variables are fixed

   The range of the varying parameter is defined respective device window. We can select the number of data readings in the measure range, the waiting time before each data reading or before the data acquisition starts. Two data averaging options are available: averaging of $n$ independent data acquisition runs or averaging of $n$ data readings at each step of the sequence.

2. Sequences of independent data acquisition runs

   Enables the performance of a predefined data acquisition run (for ex. resistance as a function of field in a given field range) for a set of different values (for ex. at different temperatures).

3. Critical Current

   This routine uses the same functions which are used in a simple data acquisition run, but instead of performing one data reading after each variable change, it

calls a critical current routine which determines the critical current at that point. This critical current routine increases the dc current fed to the sample within a specified range for a given increment and measures the sample resistance at each step. This resistance is compared to a defined criteria: if its below this criteria, the dc current is increased by one step and the resistance reread; if above, the current is decreased by one step and a new sequence of smaller increments is restarted from this value until the read resistance fulfills the criteria. The critical current value is stored, and the acquisition run continued.

Other utilities functions are also available, such as:

1. Condensation of $He_3$

   This function launches the $He_3$ condensation. A triggering signal is sent to a small current source which supplies a current to the heating resistance of the carbon container. The heating is maintained during a specified waiting time, which by default is 5 minutes.

2. Data Storing

   The read data is stored at the end of each acquisition run in a text file with two columns (X, Y), where X is the variable parameter and Y the read data. The file name and folder are specified in the Data Saving window. Comments introduced in a text case are also stored at the beginning of the data file.

3. Device Configuration

   This function enables the configuration of all devices to default values specified in a user configuration file.

## 3.2 Bitter Decoration

### 3.2.1 Principle

The technique of magnetic decoration developed from the Bitter experiment to visualize the field distribution in ferromagnetic materials [7], was first applied in 1967 by Träuble and Essmann in the observation of the vortex lattice in an alloy of lead-indium [8]. It has been used since then in the imagery of vortex structures in conventional low $T_c$ superconductors as well as in high temperature superconductors. More recently it has also been optimized for the study of vortex configurations in artificial superconducting networks [5, 9, 10].

This technique is based on the attraction of small ferromagnetic particles by the gradients of magnetic field at the sample surface, thus giving information on the static magnetic domain distribution at the decoration moment. The magnetic gradients can have a diverse nature, such as vortex cores in a type-II superconductor or the flux enclosed in a superconductor ring.

The advantage of this technique over other vortex imagery methods is both the good spatial and magnetic field resolutions (of the order of 50 nm and 0.2 mT, respectively) over a considerable surface of about 5 $mm^2$. The vortex configuration can then be studied by observing the decorated sample at room temperature with a scanning electron microscope.

In the case of superconductor samples, the decoration procedure is rather simple, though its success depends critically on certain parameters. The samples are cooled under an external magnetic field from a temperature above its transition temperature to 4.2 K, temperature at which the decoration is performed. A small amount of ferromagnetic particles deposited on a thin filament are then evaporated by a current impulse. These particles thermalize in a residual atmosphere of helium, by collisions with the helium molecules, and form small magnetic clusters which diffuse towards the sample. These clusters fall preferentially where the magnetic gradients are important, and stick to the sample surface by Van der Walls forces, thus remaining at their positions even after heating the sample to room temperature. The positions of the maximum gradients at the moment of decoration can be then visualized by SEM

microscopy, due to the contrast between the white spots formed by the ferromagnetic clusters and the sample surface.

### 3.2.2 Description of the decoration chamber

A detailed description of the decoration chamber is presented in the thesis work of Katherina Runge [5]. We will briefly review the essential parameters for a successful decoration and the decoration chamber main elements, which are: the sample holder, the source of ferromagnetic particles and the shields which protect the sample from undesirable heating during the particles evaporation.

A scheme of the decoration chamber is presented in Fig. 3.2. The chamber dimensions are as follows: external diameter of 5.8 cm, internal diameter of 4.5 cm and internal height of 9.5 cm. The sample-shield and shield-filament distances are the same and equal to 0.8 cm. The magnetic field is applied by an external coil surrounding the chamber, which is inserted in a liquid helium cryostat.

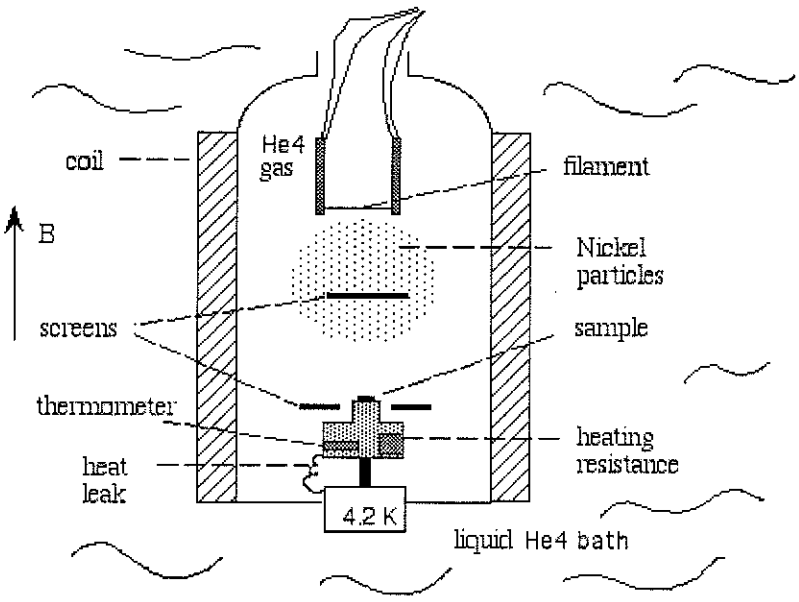


Figure 3.2: Scheme of the decoration chamber an its main constituents: the filament, the radiation screens, the sample holder and the heat leak connecting to the cold point at 4.2 K. The chamber is sealed and directly dipped into a liquid helium bath. The drawing dimensions do not scale to the real chamber dimensions.

The sample holder is formed by a small copper block where a carbon resistance thermometer and a heating resistance were installed in order to measure and control the sample temperature. This block is sustained by a stainless steel tube, the main heat exchanges with the cold point at 4.2 K being done through a thin copper wire heat leak.

A very important element are the shields, which protect the sample from direct radiation of the filament. During evaporation the filament temperature raises up to 2500 K, emitting radiant energy in all directions. When this energy strikes the shields, part of it is reflected and absorbed in the chamber walls and another part is absorbed by the shields, therefore, they must have high reflective coefficient and specific heat to prevent them from heating. In this chamber two different shields are installed: a first one which protects the sample from direct radiation and a second one which protects the sample holder. They were made of 2 mm copper foils which are coupled together to the liquid helium bath by a copper bar. The internal black wall of the chamber helps the absorption of the heat reflected from the shields. A detailed study of the temperature variation of the sample due to the filament radiation indicated a temperature increase of less than 0.7 K, at 4.2 K and at typical decoration pressures [5].

The evaporation source of ferromagnetic particles consists in a nickel-plated filament which is spot welded to a filament holder of a scanning electron microscope. The choice of Nickel as ferromagnetic material was due to its weak saturation magnetic moment (when compared to cobalt or iron) being thus less perturbing during decoration, as well as due to the facility and reproducibility of the electrochemical processes for Nickel plating. The electrochemical process we used is described at the end of this chapter.

The Nickel particles are evaporated by feeding a short voltage pulse through the filament which raises its temperature to about 2500 K. The optimum evaporation rate at decoration pressures is attained for 1.7 V pulse and 600 ms duration, the maximum current being limited to 2 A to avoid breaking the filament. Only a small part of the energy dissipated in the filament is used in the Nickel evaporation (about 30%), most of the rest being dissipated by radiation and/or evacuated by the copper

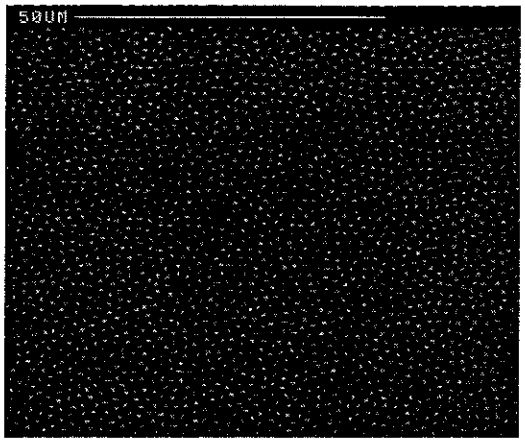


Figure 3.3: SEM image a decoration performed at 0.6 mbar and a magnetic field of 0.8 mT in a niobium film; vortices are easily identified by the white spots.

contact leads. The filament should be chosen as short and as thin as possible in order to reduce dissipation by Joule effect during the evaporation. Typical filament dimensions are 60 $\mu$m of diameter and 5 mm of length, giving an overall deposition surface of about 1 mm$^2$.

Before evaporation, the chamber is filled with helium gas. The gas pressure is a critical parameter for the success of the decoration experiment: at too high pressures the ferromagnetic particles form big clusters, reducing the imaging resolution; at too low pressures the particles are not sufficiently thermalized, resulting in poor contrasted images or no contrast at all. The best results are obtained for pressures between 0.5 and 0.7 mbar.

Figure 3.3 displays a SEM photographs of a Niobium films decorated for a magnetic field of 0.8 mT at 0.6 mbar. The vortices positions are well identified by the white spots, which have an average size of 0.5 $\mu$m.

The sample is not decorated instantaneously after the flash. Since the nickel particles are submitted to the gravity force and to the collisions with the helium molecules, the forces balance lead to a finite diffusion time for reaching the sample, which for the chamber dimensions and decoration pressures was estimated to be of the order of 20 seconds. An experimental study of the waiting time required between the flash and heating the sample to room temperature, indicated that a good resolution is attained for waiting times above 40 seconds [5].

### 3.2.3 Decoration of artificial superconducting structures: the compression layer method

In decoration vortex imagery, we are sensible to the gradients of magnetic induction instead of gradients in the order parameter, which are set by $\xi$. In the case of a superconducting film, it is the effective field screening length at the decoration temperature $\lambda(T)$, which sets the magnetic resolution, as well as the size of the decorated white spots. The field modulation associated to one vortex can then be approximated by $\Phi_o/\lambda^2$.

In the case of artificial superconducting structures, such as wire networks, it is very difficult to obtain information about the fluxoid distribution due to both the magnetic induction profile and the weak magnetic modulation attained in such structures. A detailed calculation of the field gradients as a function of the vertical distance from the network has shown that, for a cell occupied by a fluxoid, the field gradient is maximum at the sample surface on the wires. Relative gradient maxima are attained at the cell center only for distances superior to $0.3a$, where $a$ is the cell size [5]. In order to identify the occupied cells, the magnetic particles must then be stopped at about this distance. This is the principle of the *planarisation method* optimized by K. Runge [9] and which allowed the first vortex decoration in an artificial superconducting structure.

Nevertheless, this method does not discern between cells occupied by one or several fluxoids, and the field modulation is still rather weak when compared to a vortex in an uniform film. If we approximate the flux gradient in a network cell by $\Phi_o/S_{cell}$, where $S_{cell}$ is the cell surface, and use typical values for the London penetration depth in Niobium films $\lambda = 100$ nm, the magnetic modulation of a fluxoid in a cell with $1\mu\text{m}^2$ surface is about 2 mT, in contrast to 200 mT for a vortex in an uniform film.

An important innovation in this direction was introduced by A. Bezryadin [10] with the use of a compression layer. It consists in leaving a thin superconductor layer at the bottom of the network cells which, when in the superconductor state, promotes the compression of the flux enclosed in the network cells due to the formation of normal vortex cores. This method presents two advantages relative to the previous one: the magnetic contrast is increased of about two orders of magnitude and the

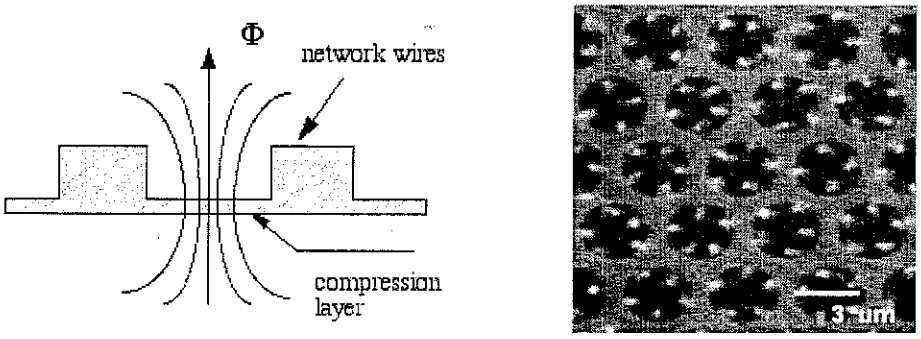


Figure 3.4: a) Compression layer method: a thin superconducting layer at the cells bottom, compress the flux threading each cell into normal core vortices. b) Decoration of triangular array of holes (black regions) at 0.6 mT by the compression layer method. The vortex positions are seen as white spots. The average flux-quanta per hole is $5\Phi_o$.

number of flux quanta threading each cell can be counted, since the enclosed flux will be compressed individually as single vortex cores in the layer.

The compression layer should be as thin as possible to minimize perturbations on the fluxoid distribution, arising from intrinsic pinning in the layer itself, effects in the boundary conditions at the cells edges, etc. In the case of Niobium networks and arrays, we use as compression layer a bottom niobium layer left from the incomplete film etching. Typically, the bottom layer has 50 nm thickness, whose transition temperature is about 8.6 K, in comparison to 9.2 K for the bulk. The minimum thickness for this layer was found to be about 20 nm, at which the transition temperature is approximately 7 K. The decrease of the niobium transition temperature with decreasing thickness is an additional advantage since when the compression layer becomes superconducting, the fluxoid distribution over the network should be already established and the initial configuration remain unchanged.

In Fig. 3.4 is displayed a SEM image of a decorated triangular array of circular holes with a bottom layer of 70 nm. The holes appear as dark circles and vortices positions are identified by the white spots. The bottom layer enables the counting of the flux quanta enclosed by each hole.

For this reason, this method was employed in the study of multi-quanta vortices trapped inside holes. The effect of the bottom layer in the number of vortices trapped by a single hole was addressed theoretically and experimentally[10]. It was shown that

though the surface transition field decreases with increasing bottom layer thickness, the winding phase number around the hole (or trapped vortices) remains unchanged. The flux-quanta trapped by a hole was observed by decoration and it was seen that it is consistent with the winding number which maximizes the critical field $H^*_{c3}$ and higher than the applied flux per hole. This results were based on the assumption, that at our cooling rates, the trapped vortices are determined during the transition and remain unchanged. In fact, since at 4.2 K the supercurrents around hole boundaries are expected to be barriers against vortex motion from holes [11], as well as the intrinsic pinning in niobium inhibits vortices to move, we believe this is a reasonable assumption.

### 3.2.4 Field calibration using Josephson-junction arrays

In this section we describe a high resolution measure of the magnetic field using Josephson junction arrays. The geometry and size of the magnetic field coil has been designed for the decoration chamber, in order to obtain an homogeneous field within 0.5% in the region of the particles diffusion, that is, inside a cylinder zone with 2 cm of length and 1 cm of radius. The coil is made of copper wire, providing a good precision at weak fields. Extra spirals are added at both extremities of the coil to compensate the coil finite size and obtain a parallel field in the center of the decoration chamber.

During a decoration experiments the chamber is shielded from the earth magnetic field by double $\mu$-metal screens. However, decorations performed at zero applied field revealed a non-zero vortex density, correspondent to an average field of 0.03 mT, which can be due either to an incomplete shielding or to trapped currents in the magnetic field coil. Such weak fields are undesirable when a high resolution of the applied field and an effective zero field are required. To overcome this problem, we employed Josephson-junction arrays to measure the effective field, taking advantage from the well know behaviour of these systems in a transverse magnetic field [12].

2D Josephson-junction arrays consist of superconductor islands, weakly coupled with its neighbours by Josephson junctions. The coupling energy between islands can be described as $E_J(T)\cos(\varphi_i - \varphi_j - A_{ij})$, where $E_J(T) = i_c(T)\hbar/2e$ is the Josephson coupling energy, $\varphi_i - \varphi_j - A_{ij}$ the gauge-invariant phase difference between adjacent

islands $i$ and $j$, and $A_{ij}$ the line integral of the vector potential $\mathbf{A}$. As a result, the coupling varies periodically with applied field, and if only first-neighbour interactions are considered, the Hamiltonian of the system is given by,

$$H = -E_J(T) \sum_{ij} \cos(\varphi_i - \varphi_j - A_{ij})$$

which is periodic on the frustration parameter $f$, defined as $f = BS_{cell}/\Phi_o$, with period $f = 1$, where $B$ is the magnetic induction and $S_{cell}$ the surface of a unit cell of the array.

This periodicity is obviously reflected in the transport properties such as the magnetoresistance, which is periodic with $f = \pm 1$ and present additional local minima at fractional values of $f = p/q$ with $p$ and $q$ integers. The magnetic period $\Phi_o/S_{cell}$ is determined by the surface of the cell array, therefore a high sensitivity in the applied field can be attained using arrays with small cells. For example, for a cell size of $10 \times 10$ $\mu$m$^2$ the magnetic period is approximately 0.02 mT. Moreover, the main oscillations remain exactly periodic in applied field for $f$ values of the order of 10 or more, as long as self screening effects can be neglected, providing an excellent method for calibrating weak magnetic fields.

We performed calibration measurements using a triangular array of crosses, as illustrated in Fig. 3.5. The crosses are superconducting islands coupled to the adjacent ones by a thin superconductor layer of 50 nm which is left during the etching process. These samples were supplied to us by the group of P. Martinoli from Nêuchatel, Switzerland. They were fabricated using a niobium thin film of 200 nm thickness deposited on a silicon substrate and coated with a 700 nm resist layer (SHIPLEY SPR 3008). The patterning was done by *DUV* lithography, using a high precision chromium mask, with lattice constant of 15 $\mu$m. The crosses arms are 3.5 $\mu$m wide and separated from adjacent crosses by 675 nm. The film is etched by $SF_6$ *Reactive Ion Etching* through the resist mask during 50 s.

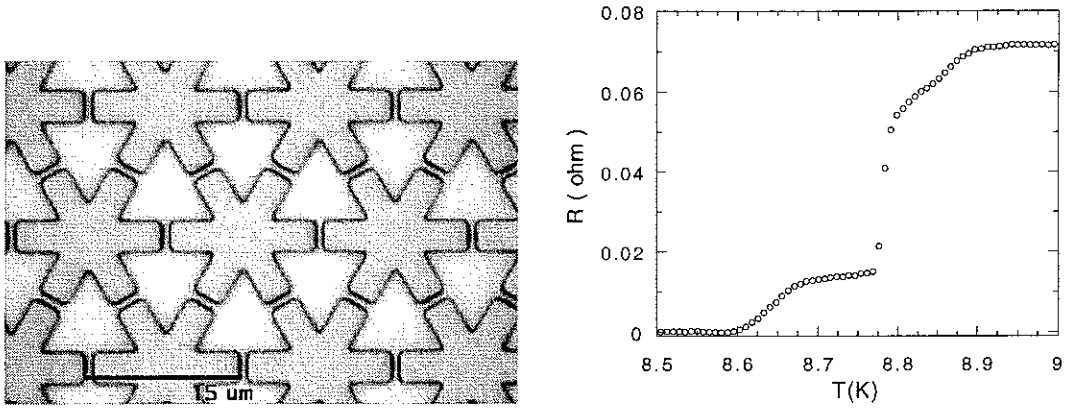


Figure 3.5: Photograph of the Niobium triangular array. The superconductor islands (stars) are coupled to the adjacent ones by a thin superconductor bottom layer. Resistive transition of the triangular array in zero applied field. The first main transition corresponds to the onset of superconductivity in the islands while the second transition at 8.65 K marks the onset of the Josephson coupling regime.

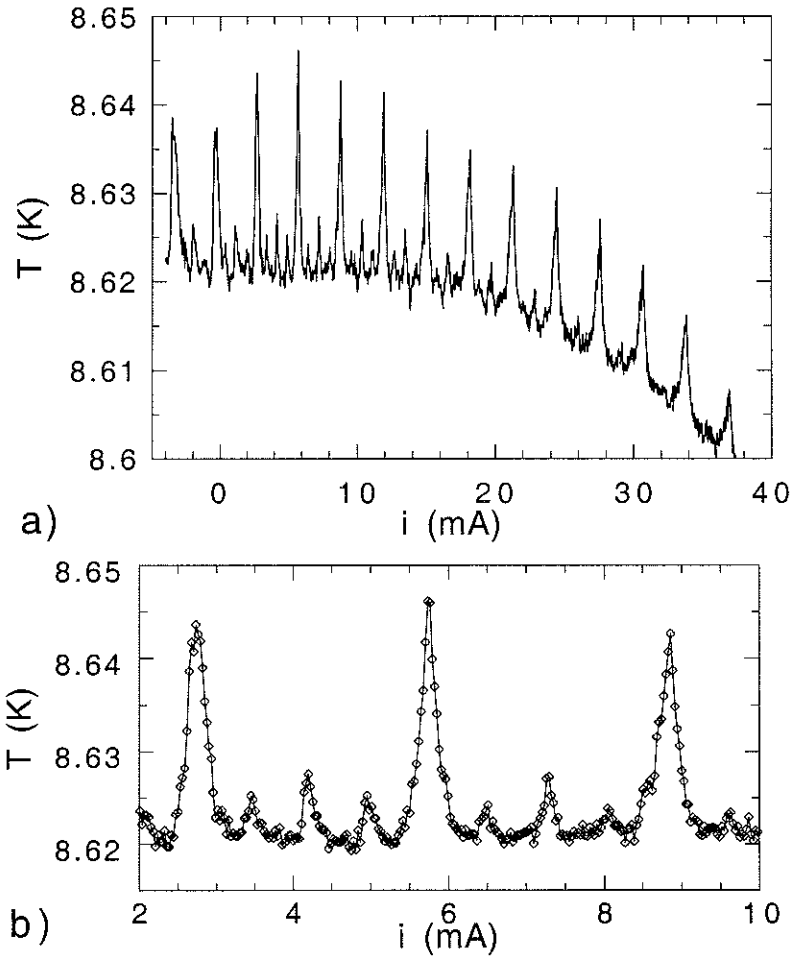


Figure 3.6: a) Transition temperature of the triangular Josephson-array as a function of the applied field, here represented by the current fed into the coil. b) Zoom close to the effective zero field, in this case compensated with an applied current of 5.73 mA.

The transport measurements were made using a four-probe resistance bridge, with an ac measuring current of 4 $\mu$A and 33 Hz frequency. The resistive transition in zero applied field is represented in Fig. 3.5. The main transition corresponds to the superconducting transition of the crosses and the second transition at lower temperatures corresponds to the Kosterlitz-Thouless transition.

Since the coupling between crosses is only established during this second transition, we measured the field dependence of the array transition in this resistive regime. This transition temperature is determined by measuring the thermometer resistance while a feedback heating procedure controlled by the sample itself, maintains its resistance at a constant value while the magnetic field is increased. The results obtained for a 0.5 m$\Omega$ criteria are displayed in Fig. 3.6 as a function of the field coil bias current. Each point corresponds to a current increment of 0.03 mA. This measurement corresponds to a resistance criteria of 0.5 m$\Omega$, that is, at the tail of the second resistive transition shown in Fig. 3.5.

Sharp peaks can be distinguished until a current in the coil of 40 mA, and are exactly periodic on current, with a period of 3.1 mA. The main peaks corresponds to integer values of frustration $f = BS_{cell}/\Phi_o$, the magnetic induction field being obtained from the current $i$ applied in the coil by,

$$B = b\, i + B_{rem}.$$

The coefficient $b$ can thus be determined from a linear fit of the peak frustration as a function of $i$, as displayed in Fig. 3.7. Using the unit cell surface, which is 97.43 $\mu$m$^2$, we obtained $b = 6.81$ $\mu$T/mA.

The second advantage of using a Josephson-junction arrays for the field measurements is that since the barriers against vortex motion is only a small fraction of the array coupling energy (0.2 $E_J$(T) [13] for a square array), close to the transition temperature the vortices are very mobile. The oscillations of the magnetoresistance as well as of the array transition are then very sharp and the zero field peak the most prominent, thus the effective zero field can be determined with a good accuracy. As we can see from Fig. 3.6 the highest peak is situated at $i = 5.73$ mA, which corresponds to an unscreened magnetic field of $-0.039$ mT. The transition temperature corresponding to the three main peaks close to the effective zero field is displayed

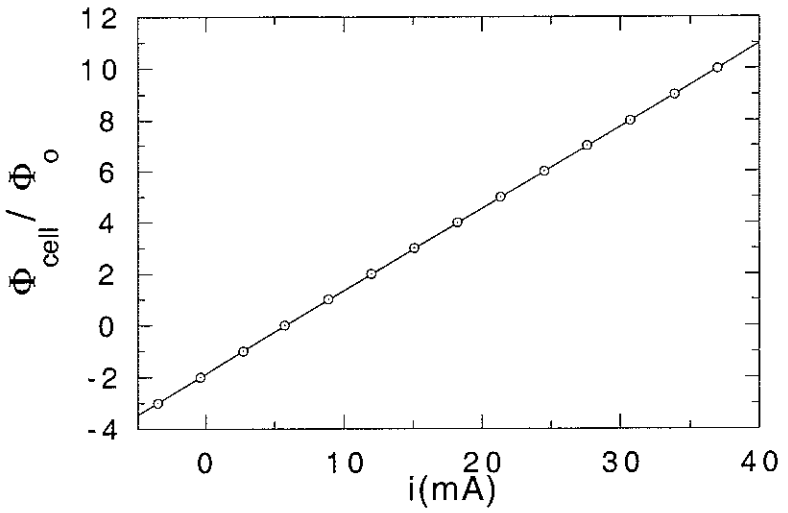


Figure 3.7: Frustration of the fundamental peaks of the transition line *vs* the applied current in the field coil (open dots). The linear fit used in the determination of the field calibration coefficient is represented by the solid line.

in Fig. 3.6 as a function of applied current. The peak half-width corresponds to an applied current difference of 0.25 mA, that is to a difference in the applied field of 1.7 $\mu$T. The array is sensitive to the current increments of 0.03 mA in applied field, that is, to a field variation of 0.2 $\mu$T which corresponds to about 100 $\mu$m distance between vortices, which fulfills the requirements for quenching experiments in zero applied field with cooling rates of the order of the millisecond. This resolution is related to the temperature regulation while the magnetic field is swept. It can be further increased by measuring close to the zero field peak the magnetoresistance with finer field steps at a constant temperature. The superfluid response of these arrays to a weak ac magnetic field is sensible to about 1 nT in the center of the array [12].

## Electrochemical process for nickel deposition

The electrochemical processes for nickel deposition are very well known and reproducible, enabling a good control of the deposited amount. An average mass of 60 $\mu$g of nickel is usually deposited by the electrochemical process further described. The tungsten filament is previously cleaned in the acid solution,

| | |
|---|---|
| $HNO_3$ | 37.5% in volume |
| HF | 37.5% in volume |
| $H_2O$ | 25.0% in volume |

then rinsed during a few minutes in distilled water to stop the reaction and further rinsed in ethanol. The Nickel filament should be previously cleaned in a solution of nitric acid.

The electrochemical deposition is then performed using the tungsten prominent as cathode and as anode a nickel filament, which are immersed in the following solution,

| | |
|---|---|
| $NiCl_2$ | 300g/l |
| $H_3BO_3$ | 30 g/l |

A 1 mA current is applied between the cathode (W) and the anode (Ni) electrodes during 3 minutes, leading to a voltage of about one volt. If the deposition is proceeds at higher voltages it means that the filaments are not clean enough and it is advised to stop the process and restart with cleaner ones.

## 3.3 Concluding remarks

The general details of the used measurement techniques were presented. The measurements were performed on pre-existent cryostat, however some innovations were introduced. For transport measurements, a very complete software was implemented and the automation of several data acquisition modes is now available, as well as the automation of some routine tasks ($He^3$ condensation, data saving, ...). In the case of the Bitter decoration it was introduced a high resolution method for the measurement of the effective magnetic field, with a resolution better than 0.4 $\mu$T, which is particularly valuable for decorations performed at weak magnetic fields and at effective zero field.

# Chapter 4

# Coherence of superconducting edge states on periodic arrays of micro-holes

Dans ce chapitre nous présentons une étude expérimentale de l'interaction entre les états de bords en fonction du champ magnétique dans un réseaux de trous. Ces états de bord correspondant à des états de supraconductivité de surface localisés autour des bords de chaque trou, dans une région de l'ordre de la longueur de cohérence. Nous avons étudié un réseau périodique carré avec un pas de 4 $\mu$m, et avec de trous carrés de taille proche de 2 $\mu$m. Ces dimensions ont été choisies de façon à distinguer le passage d'un comportement collectif à un comportement de trous, par l'augmentation du champ magnétique et ainsi étudier le régime à bas champ. Pour cette étude nous avons utilisé des échantillons en aluminium fabriqués par photolithographie en ultraviolet profond, suivie d'un *lift-off*. La température de transition supraconductrice a été étudiée par des mesures de transport à quatre fils en fonction du champ magnétique appliqué. Nous avons observé une structure très riche, caractérisée à bas champ par des oscillations de concavité positive, ayant des maxima locaux périodiques avec un quantum de flux par plaquette du réseau. Ce comportement est caractéristique d'une interaction collective entre des états de bord. Nous avons pu montrer que ce comportement est typique d'un réseau de fils 2D et persiste tant que la longueur de cohérence est supérieure à la distance entre les bords de trous voisins. D'autre

part, nous avons pu constater que dans le régime de réseau de fils, le processus de nucléation est déterminé par des conditions aux limites aux bords de trous adjacents, le passage au régime de trous isolés étant associé au passage à une nucléation au bord d'un seul trou. Ces phénomènes de supraconductivité de surface n'avaient pas été étudié dans une structure multiconnexe, comme un réseau, où ils sont responsable d' une forte augmentation de la température de transition du réseau, et de la mise en ordre des vortex interstitiels dans un régime de champ intermédiaire. Nos résultats sont comparés à un travail précédent de A. Bezryadin, pour des réseaux carrés de trous circulaires ou le rapport entre la taille du trou et le pas du réseau est le double de notre réseau et où le régime collectif est représentatif d'un couplage faible. Un modèle proposé par Rosario Fazio et qui décrit l'interaction entre les états de bord par couplage Josephson permet d'obtenir les traits essentiels du passage du régime de trous isolées au régime collectif. Nous effectuons une analyse systématique de l'ensemble des régimes. Ce travail sera publié dans Journal of Low Temperature Physics.

# Introduction

The effect of artificial pinning centers on the vortex dynamics of type-II superconductors has attracted a great interest in both fields of high $T_c$ and conventional low $T_c$ superconductors. Low $T_c$ materials are particularly interesting due to the development of nanofabrication techniques which enable the introduction in a controlled way of nanofabricated defects. These patterned samples constitute relatively simple systems for the study of how geometric parameters such as defect size, shape and/or defect density influence vortex dynamics[14, 15, 16, 17].

Previous experiments on superconducting arrays of holes have shown that the transition line is dominated by surface superconducting states nucleated around the hole boundaries [14, 15]. As a result, the array transition occurs at fields $H_{c3}^*$ higher than the nucleation fields in the bulk $H_{c2}$, and the transition line $T_c^*(H)$ exhibits a non-trivial field modulation due to flux quantization of the edge states over the two geometric lengths of the problem: the hole surface and the array elementary cell.

In particular, it was previously identified a crossover with decreasing field from an isolated hole regime to a low field regime dominated by the interaction between edge states. Though the behavior at high fields was well understood, the nature of the interactions at low fields remained unclear. The two extreme cases, the isolated hole in an infinite film[18] and the superconducting wire network [19, 20] (vanishing hole separation) are quite well known. The relevant parameters for this problem are the external field, the temperature dependent coherence length ($T_c^*$), the lattice constant $a$, the hole size, and the inter-hole distance $w$. We tried to put forward the role of these parameters on the crossover to the collective regime and the type of interaction established at low fields.

In this chapter we present by transport measurements an experimental study of the superconducting transition line of a square array of square holes where the aspect ratio hole size/lattice parameter is approximately two. This array is made of aluminium and its dimensions were chosen in order to obtain a clear crossover from a collective to a single hole behaviour of the array with increasing field. Our results are compared with the previous work of A. Bezryadin [14, 15] on a different array with similar aspect hole/lattice parameter but with twice the distance between hole edges. The collective regime at low fields is established when the distance between adjacent hole edges $w$ is comparable to the array lattice constant $a$ and is addressed in detail. A distinct behavior at low fields was found between samples and was interpreted as arising from distinct nucleation processes, which are determined by the ratio $w/\xi$.

When $w/\xi(T_c^*)$ is lower than the critical ratio 1.84 [21], nucleation is then dominated by thin wire superconducting edge states and the coupling is well described by the formalism of superconducting wire networks [19, 20] as observed in our measurements. In the regime $w/\xi(T_c^*) > 1.84$, edge nucleation is determined at the single hole edge but if $w$ is still small enough to allow a weak overlap between neighbor edge state wave functions, the low field behavior can be interpreted using a simple model based on a weak link interaction between adjacent edge states. This model proposed by R. Fazio is able to capture the essential features of the crossover previously discovered [14, 15]. The results here discussed are essentially those to appear in Journal of Temperature Physics.

## 4.1 Experimental Results

The array sample consists of a thin film of aluminum (80 nm) patterned with a regular square array of nanofabricated holes. The lattice spacing is 4.0 $\mu$m and holes have a square shape with $1.85 \pm 0.01$ $\mu$m side length, the distance between neighbor hole edges being $w = 2.15 \pm 0.01$ $\mu$m as determined by SEM microscopy. We shall refer to this sample as sample A. The full array size is $1 \times 1$ cm$^2$ corresponding to a total of $6.25 \times 10^6$ holes.

The patterning was defined on a monolayer PMMA coated 2" Si wafer by Deep UV photolithography using a high precision chromium mask [1]. The sample is then prepared using conventional *lift-off* techniques after thermal evaporation of pure aluminum over the resist mask on a UHV chamber. An homogeneous thin film of aluminum evaporated at the same time and submitted to the same fabrication steps is also measured for a reference of the patterning process effect on the material parameters.

Both samples were studied by conventional four-probe resistance measurements using an AC four terminal resistance bridge at a 33 Hz frequency and a measuring current of 2 nA. Assuming an uniform current distribution over the array, the current density per wire is $4.5 \times 10^{-4}$ Acm$^{-2}$. We used a similar in-line geometry for the voltage contacts (spiral-shaped) in the array sample as in Ref.[14, 15], placed at a distance of 2.8 mm from each other in the array center to avoid short circuits from the sample borders. For the reference sample we simply attached gold (non-superconducting) wires by ultrasound bounding. No overshoot in the $R(T)$ curves was observed, in contrast to the reference sample in [14, 15] where the spiral contacts were used and small cusps in the R(T) curves were present. [2]

Resistance measurements as a function of temperature were also performed at sev-

[1] 2 1/2 quartz plate fabricated by CSEM, Neuchâtel, Switzerland

[2] We remark that the R(T) curves for array A in non zero field do not exhibit the double transition observed on array B, which was then assigned to a first transition at $T_{c2}$ and to a second transition at higher temperatures $T_c^*$. We now believe the observation of the $T_{c2}$ transition in array B was possible due to the transition of the 20 $\mu$m strips between patterned fields (of about $300 \times 300$ $\mu$m$^2$). In the case of array A, which is an homogeneous pattern over a 1 cm$^2$ surface, the double transition is not observed.

| *Sample* | *hole shape* | $a$ ($\mu$m) | $w$ ($\mu$m) | $T_{co}$ [K] | $\xi(0)$ ($\mu$m) |
|---|---|---|---|---|---|
| array A | square | 4.0 | 2.15 | 1.263 | 0.25 |
| array B | circle | 9.0 | 4.74 | 1.25 | 0.25 |

Table 4.1: Some parameters of array A and array B. The array lattice constant is $a$ and $w$ the minimum distance between the edges of adjacent holes.

eral magnetic fields between 0 and 5 mT. From the zero field R(T) measurement we estimated several material parameters. Using a two-dimensional Aslamazov-Larkin fit [22], we estimate a BCS transition temperature $T_{co} = 1.262$ K and a normal state resistance of $R_n = 0.099\ \Omega$. The resistance per single wire of length $a = 4.0\ \mu$m and width $w = 2.15\ \mu$m is then $r_n = 0.354\ \Omega$ and the normal state resistivity $\rho_n = 1.49\ \mu\Omega$cm. Using $v_F = 2.03 \times 10^8$ cm/s we obtain an electronic mean free path $l_{el} = 26.5$ nm. The zero field transition temperature defined at half of the normal state resistance are 1.263 K and 1.265 K for the patterned sample and the homogeneous thin film, respectively, the transition width being 3 mK for both samples. We summarize on Table 1 some parameters of array A and the parameters of the sample previously studied [14, 15], array B. This array consists on an aluminum thin film (80 nm thickness) patterned with a square array of circular holes of diameter $2r = 4.26\ \mu$m and a lattice parameter of 9.0 $\mu$m.

The field dependence of the nucleation temperatures $T_c^*(H)$ is determined using a heating feedback technique that keeps the sample resistance at a constant value while the magnetic induction field is smoothly varied by small increments of 0.2 $\mu$T. This method enables us to attain a fine field tuning of the array transition line. Several resistance criteria between 0.01 and $0.7R_n$ were used. The nucleation temperatures using the sweeping field method agree by less than 1 mK with those obtained for the same resistance criteria from R(T) measurements, indicating a good temperature regulation attained by the feedback method.

The transition line $T_c^*(H)$ of array A for criteria $0.4R_n$ is displayed in Fig. 4.1.a) as

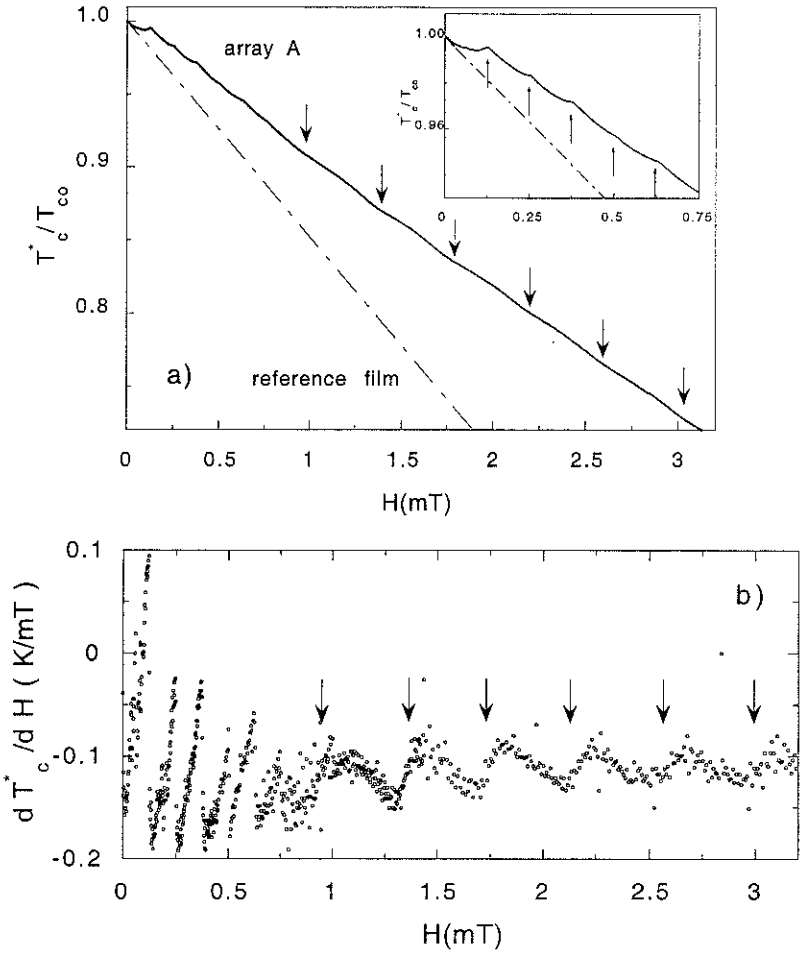


Figure 4.1: a) Field dependence of the superconducting transition line $T_c^*(H)$ of array A (solid line) and of the reference sample $T_{c2}(H)$ (dashes line). Two types of field modulation are clearly identified for array A: downward, large period oscillations with dips at half integers of $\Phi_o$ per hole (down arrows) and upward oscillations of shorter period with cusps at integers of $\Phi_o$ per array elementary cell (inset:up arrows); b) $T_c^*(H)$ slope for array A as a function of H. The change of magnetic period due to the crossover from collective to single hole regime is quite visible.

a function of applied field. For comparison it is also displayed the bulk transition line reconstructed from $H_{c2}(T^*/T_{co}) = (1 - T^*/T_{co})\,\Phi_o/2\pi\xi^2(0)$, using the reference film coherence length at $T = 0$ K, $\xi(0) = 220$ nm (determined from the initial linear slope of the reference film transition line). The array transition line is clearly above the estimation for the bulk. Besides, the non-trivial field modulation associated to the single hole and collective regimes are clearly identified. At fields below 0.75 mT it is characterized by periodic upward cusps, with a magnetic period of exactly $H = 0.128$ mT, that correspond to a quantum flux enclosed on a square cell of side length $a = 4.0$ $\mu$m, indicating the presence of phase coherence over the array lattice. At higher fields, the transition line exhibits downward dips occurring with a larger magnetic period. These large period oscillations correspond to the single hole regime discussed previously. In this case, the magnetic period is not constant since it depends on the effective surface formed by the hole radius and the surface superconducting sheath surrounding the hole. The average magnetic period is 0.543 mT, which corresponds to an effective square surface of side length $l_{hole} = 1.94$ $\mu$m, comparable to the array hole size of 1.85 $\mu$m.

These field modulations were found for all the criteria used in the transition line measurement. The crossover between the two field regimes is well illustrated on Fig. 4.1.b) where the sawtooth variation of the transition line slope $dT_c^*(H)/dH$, at low field gives place to a smoother variation at higher fields, along with the change of magnetic period.

## 4.2 Extraction of the nucleation energies

The role of the nucleation processes involved will be discussed in terms of the energies for nucleation of superconductivity at a given field, $\epsilon_{nucl}$. The energy $\epsilon_{nucl}$ can be obtained by finding the lowest eigenvalue solution of the linear Ginzburg Landau differential equation

$$\frac{\hbar^2}{4m}\left[\frac{\nabla}{i} - \frac{2e}{c}\mathbf{A}\right]^2 \psi(\mathbf{r}) = \epsilon_{nucl}\psi(\mathbf{r}) \tag{4.1}$$

which fulfills the given boundary conditions on the order parameter $\psi(\mathbf{r})$.

This approach is valid when we can neglect spatial variations of $|\psi(\mathbf{r})|$, such as

thin films or wires of thickness $\ll \xi$ or when the applied magnetic field reduces $|\psi(\mathbf{r})|$ to a value much smaller than the equilibrium amplitude $|\psi_\infty|$ achieved deep inside the bulk superconductor. The regime of validity is then usually restricted to temperatures close to $T_{co}$.

An alternate approach is to extract $\epsilon_{nucl}$ at a given field from the measured $T_c^*(H)$ using the relation [23, 24],

$$ln\left[\frac{T_c^*}{T_{co}}\right] = \Psi_D\left[\frac{1}{2}\right] - \Psi_D\left[\frac{1}{2} + \frac{\epsilon_{nucl}}{4\pi k_B T_c^*}\right] \tag{4.2}$$

where $\Psi_D(x) = \Gamma'(x)/\Gamma(x)$ is the digamma function. This relation describes the depression of $T_c^*(H)$ relative to $T_{co}$ due to a magnetic perturbation. Though it was initially established by Abrikosov and Gor'kov for magnetic impurities [23], it can be generalized to all pair breaking perturbations which destroy the time reversal symmetry of Cooper pairs [24, 25], if the scattering time of the electron pair is short enough for their relative phases be randomized by the perturbation.

It can thus be applied to a dirty superconductor in strong external magnetic fields (and only surrounded by insulators), if the mean free path $l_{el}$ is much smaller than all sample dimensions and $\xi_o$ or in the case of a small superconducting particle with all dimensions $\ll \xi_o$. The sample thickness must be smaller than $\xi$ and the penetration depth to ensure the penetration of the magnetic field. At temperatures close to $T_c^*(H)$, $\epsilon_{nucl}$ is the energy required to break the Cooper pair thus destroying superconductivity. When $T_c^* = 0$, (or $H = H_{c3}^*(0)$), $\epsilon_{nucl}$ coincides with the BCS superconducting gap $1.76 k_B T_{co}$. Close to $T_{co}$ the digamma function can be expanded around 1/2 and the $T_c^*(H)$ depression is linear in $\epsilon_{nucl}$, $T_{co} - T_c^*(H) = \epsilon_{nucl}\pi/8k_B$.

The advantage of using Eq. 4.2 on the determination of $\epsilon_{nucl}$ is that it remains valid down to all temperatures and in strong magnetic fields. The linear Ginzburg-Landau results can be recovered if the temperature dependent coherence length is defined as $\xi^2(T) = D\hbar/\epsilon_{nucl}$, where $D = 1/3 v_F l_{el}$ is the coefficient for electronic diffusion. For sample A, $D = 180$ cm$^2$s$^{-1}$ obtained from the mean free path $l_{el} = 26.5$ nm. Using $\xi^2(0) = \hbar D/1.76 k_B T_{co}$ we estimate $\xi(0) = 250$ nm.

We calculated $\epsilon_{nucl}(H)$ for arrays A and B using Eq. 4.2 and the experimental $T_c^*$ at the given applied field H. These results are displayed in Fig. 4.2 after being normalized by the nucleation energy on the bulk, $\epsilon_{c2} = hDH/\Phi_o$, with the same coherence

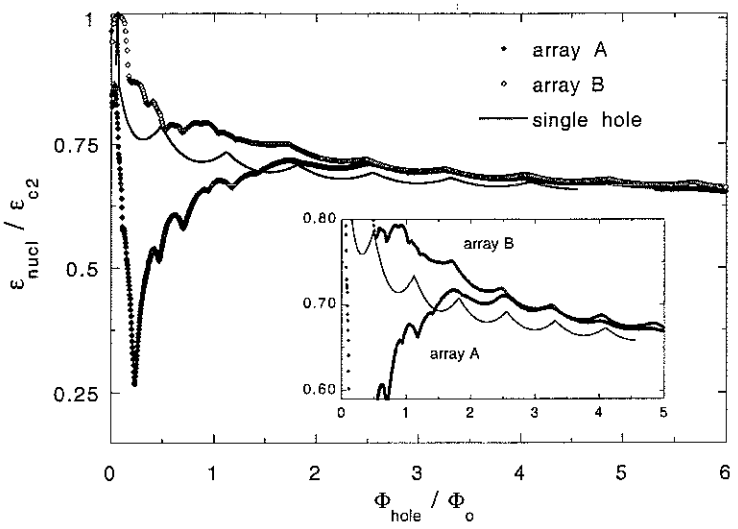


Figure 4.2: Normalized nucleation energies $\epsilon_{nucl}/\epsilon_{c2}$ as a function of magnetic field (in units $HS_{hole}/\Phi_o = \Phi_{hole}/\Phi_o$), for sample A (solid dots), sample B (open diamonds) and the theoretical calculation for a cylindrical cavity in an infinite thin film (solid line).

length as the array. For comparison, we also represent the theoretical $\epsilon_{nucl}/\epsilon_{c2}$ for a circular hole on an infinite film (solid line) [10]. In fact, the representation $\epsilon_{nucl}/\epsilon_{c2}$ is equivalent to the inverse ratio of the nucleation fields $H_{c2}/H^*_{c3}$, that close to $T_{co}$ acquires the Ginzburg Landau form $H_{c2}/H^*_{c3} = (1-T^*_c/T_{co})\, H_{c2}(0)/H$, using $H_{c2}(0) = \Phi_o/2\pi\xi^2(0)$ and the coherence length as defined above.

From Fig. 4.2 it is clear that in the high field regime both samples are very well described by the theoretical single hole case. With decreasing fields both arrays deviate from the single hole description, with the appearance of the collective field modulation, periodic on $\Phi_o$ per array cell, and with upward concavity.

It is in this regime that the samples present a strikingly distinct behavior. The reduced energies $\epsilon_{nucl}/\epsilon_{c2}$ for sample B and for the single hole tend to an overall increase with decreasing field, reaching 1 at zero field. In contrast, for sample A, $\epsilon_{nucl}/\epsilon_{c2}$ decreases with decreasing field, dropping well below the single hole line. This means that in this regime, array A presents a ratio $H^*_{c3}/H_{c2}$ higher than the classical limit of 1.69 for an infinite surface sheath[21]. Comparing the array geometric parameters, they both have similar aspect ratios $w/a$, 0.54 (array A) and 0.53 (array

B), respectively and similar ratios of the superconducting volume over the array cell volume $V_s/V_{cell}$, 0.79 (array A) and 0.82 (array B). We thus believe the distinct low field behavior is associated to the different ratio $w/\xi(T_c^*)$, which close to $T_{co}$ controls the process of edge nucleation and the type of coupling. In fact, both samples loose the collective behavior for $w/\xi(T_c^*) > 3$.

On the following subsections we shall analyze these features by describing the array nucleation energy as coming from two main contributions: the nucleation energy of the single edge state and the coupling energy between neighbor edge states.

## 4.3 Wire networks of wide strands

In this section we focus on the low field behavior of array A. In this regime, the array energy is a sum of the nucleation energy on a individual wire in parallel field $\epsilon_{strip\|}$ and a coupling energy, that can be described within the framework of superconducting wire networks theory [19, 20].

The case of superconducting wire networks of narrow wires is well understood. It can be treated as a periodic array of superconducting islands strongly coupled to each other by thin superconducting wires of length $a$ ($\xi >> a$) and width $w >> \xi$. Neglecting superconducting fluctuations, the coupling energy can be computed within mean-field theory by solving the linearized Ginzburg-Landau equations at each node of the network. For a regular square lattice (same length of all strands) the order parameter $\psi_i$ on each island $i$ will be coupled to the first neighbor sites through field dependent phase factors as,

$$4\ \cos(u)\ \psi_i = \sum_j \psi_j \exp(-i\gamma_{ij}) \tag{4.3}$$

where 4 is the lattice coordination, $\gamma_{ij} = 2\pi/\Phi_o \int_i^j \mathbf{A}\cdot d\mathbf{l}$ is the phase factor along the wire linking site $i$ to a site $j$, $\mathbf{A}$ the vector potential, and $u = a/\xi(T)$ is the strand length in units of $\xi(T)$. The coupling energy is then given by, $\epsilon_{wnt} = \hbar D u^2/a^2$.

Eq. 4.3 is equivalent to a tight binding equation in a potential with the same geometry and tight binding energy $\epsilon_{tb} = 4\ \cos u$. The network coupling energy $\epsilon_{wnt} = \hbar D u^2/a^2$ can then be expressed in terms of the tight binding ground state

level $\epsilon_{tb}$ with $u = \arccos(\epsilon_{tb}/4)$ [26, 27]. However, this relation is only valid in the limit $w << \xi$. Taking into account the finite thickness of the wires, a more complex relation between $\epsilon_{tb}$ and $u$ is obtained, $\epsilon_{tb} = 4\ \cos u + 4\ \tan(uw/2a)\ \sin u - uw/a$ [28]. This result was established for zero external field but it can still be applied at low fields while there are no vortices in the wires.

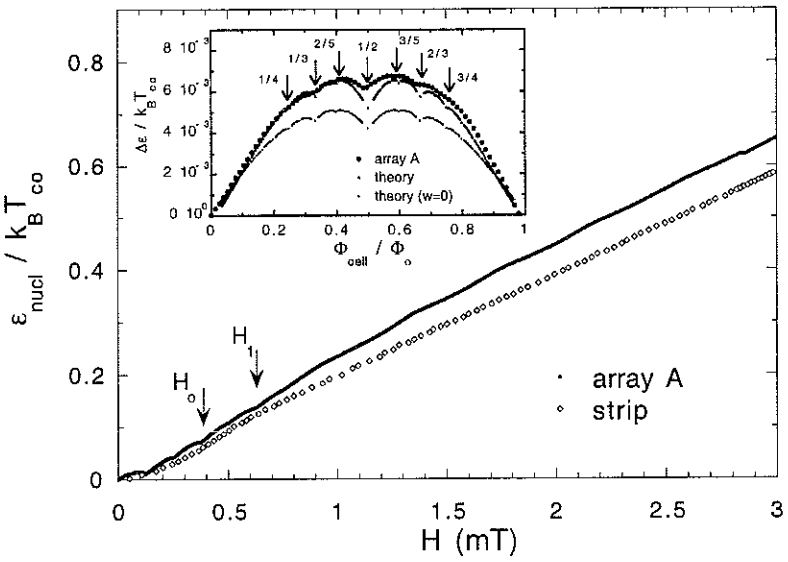


Figure 4.3: Field dependence of the nucleation energies of array A (solid dots) and for a strip of width $w = 2.15\mu$m (open diamonds), normalized by $k_B T_{co}$. In the field range $H_o < H < H_1$ interstitial vortices appear within strands. Inset: Coupling energy $\epsilon_{wnt}$ for array A (solid dots) and the theoretical $\epsilon_{wnt}$ for a superconducting wire network with $w = 0$ (small dots; lowest curve) and taking into account the wire thickness (small dots, upper curve) as a function of reduced field $\Phi_{cell}/\Phi_o$ between 0 and 1. The main dips position at rational $p/q$ are indicated by down arrows.

In the inset of Fig. 4.3 is displayed the coupling energy of array A and the theoretical $\epsilon_{wnt}$ energy as a function of magnetic flux per array elementary cell $\Phi_{cell}$, for $\Phi_{cell}/\Phi_o$ between 0 and 1. The coupling energy for array A is obtained from $\epsilon_{nucl}$ (calculated using Eq. 4.2 and the experimental $T_c^*(H)$) after subtracting the parabolic energy contribution due to edge nucleation in the wires, $\epsilon_{strip\ ||}$. The theoretical $\epsilon_{wnt}$ is obtained from the ground state tight binding energy calculated for rational values of $\Phi_{cell}/\Phi_o = p/q$, with $q < 30$ and $p < q$. A very good agreement is obtained between the experimental and the theoretical data which take into account the wire thickness.

The theoretical results in the limit $w = 0$ lead to a smaller energy. Since we are close to $T_{co}$, the variation of $T_{co} - T_c^*(H)$ due to the coupling (after subtracting the linear dependence on H) corresponds to $\epsilon_{wnt}\pi/8k_B$.

Besides the fundamental dips at $\Phi_{cell}/\Phi_o = 0, 1$ and at $1/2$, additional dips can be identified at rational values $\Phi_{cell}/\Phi_o = p/q$, for $q = 3, 4$ and 5. This field structure is a manifestation of the interference of quantum states over cells of size $qa \times qa$ [27]. With increasing field, the fine field structure becomes less pronounced and only the fundamental dips remain until $\Phi_{cell}/\Phi_o = 8$. At higher fields the single hole regime is recovered.

In fact, the crossover to the single hole regime is associated to a crossover from a two-boundary to a one-boundary nucleation process in the network wires. This explains the smaller values of $\epsilon_{nucl}/\epsilon_{c2}$ when compared to the classical limit $\epsilon_{nucl}/\epsilon_{c2} = 0.59$ for nucleation in an infinite surface sheath[21] or for nucleation in a single hole. Such as for a thin slab in a parallel field, edge nucleation in the array at low fields is controlled by two boundary conditions imposed at the edges of adjacent holes.

The field dependence of $\epsilon_{strip\ ||}$ for a strip or slab of intermediate thickness $w$, is strongly dependent on $w/\xi(T_c^*)$. Below a critical thickness $w < 1.84\ \xi(T_c^*)$ (thin wire limit) nucleation starts symmetrically at both surfaces and the maximum of the order parameter occurs at middle distance between them. In this limit $\epsilon_{strip\ ||} = H^2w^2(\pi hD/6\Phi_o^2)$. With increasing field, when $w > 1.84\ \xi(T_c^*)$, $\epsilon_{strip\ ||}$ deviates from the parabolic field dependence as the order parameter solutions at each surface pull apart, their superposition giving rise to nodes along the middle plane of the wire and equidistant of $\Delta L \approx \Phi_o/Hw(1 - 1.84\xi)$. With increasing field the vortex pattern becomes more complex, until the interference between the surface solutions become negligible (compared to $k_BT_c^*$) and the one-boundary solution is recovered. In this limit $\epsilon_{strip\ ||}$ approaches the surface sheath result $0.59hDH/\Phi_o$.

All these features were discussed previously [21, 29, 30]. Here we are interested in comparing the envelope of the energy curve for array A and the nucleation energy for a strip, $\epsilon_{strip\ ||}$. On Fig. 4.3 is displayed $\epsilon_{nucl}$ for array A and $\epsilon_{strip\ ||}$ for a wire with the same width $w$ as the array strands as a function of applied field. We can identify several similarities. On the single hole regime the main dependence of $\epsilon_{nucl}$ is linear

on H such as the field dependence of $\epsilon_{strip\ ||}$ in the surface sheath limit, in agreement with the dominance of one-boundary nucleation at the edges of each individual hole. With decreasing field both curves deviate from the linear field dependence due to the emergence of interference between adjacent surfaces solutions. This deviation occurs near the field $H_1 = 0.65$ mT which corresponds to the position of the first important collective dip of $\epsilon_{nucl}/\epsilon_{c2}$ at $\Phi_{cell}/\Phi_o = 5$ (see also Fig. 4.4.b). Below the field $H_o \approx 2.75\ \Phi_o/\pi w^2$ (0.39 mT) nucleation starts symmetrically[21] in the strip and the order parameter is maximum at middle distance between adjacent edges. The occurrence of symmetric nucleation on a low field regime explains why the wire network description is still valid for arrays of wide strands. In the regime $H < H_o$, the collective dips of $\epsilon_{nucl}$ approach the parabolic envelope $\epsilon_{strip\ ||}$, since at integers values of $\Phi_{cell}/\Phi_o$ the costs in coupling energy are minimum. These results thus indicate that the small values of $\epsilon_{nucl}/\epsilon_{c2}$ for array A at low fields are simply related with the two-boundary nucleation process.

On the other hand, since the crossover from two-boundary to one-boundary nucleation is associated to the appearance of interstitial nodes of the order parameter within strands, we expect a broadening of the array resistive transition with increasing field due to these weakly bounded interstitial vortices. In Fig. 4.4 is represented the field variation of the resistive transition width $\Delta T_c^*(H)$, for array A obtained by subtracting the transition lines $T_c^*(H)$ measured for resistive criteria $0.7R_n$ and $0.03R_n$. For comparison, we also represent the field variation of the distance $\Delta L$ between nodes on a single wire, normalized by the array lattice parameter $a = 4\ \mu$m.

At fields $H \leq H_o = 0.39$ mT (region I, $\Phi_{cell}/\Phi_o \leq 3$) the transition width at integers $\Phi_{cell}/\Phi_o$ is the same as in zero field since there are no order parameter nodes in the strands, only coreless vortices inside holes. At integers $\Phi_{cell}/\Phi_o$, the flux quanta per array cell corresponds to the quanta enclosed by each hole. The transition is then sharpened since every hole encloses the same number of flux quanta. At intermediate values of $\Phi_{cell}/\Phi_o$ phase fluctuations lead to a small broadening of the transition (of about 1 mK).

At fields $H_o < H < H_1$ (region II, $3 < \Phi_{cell}/\Phi_o < 5$), the first nodes of the order parameter are expected to appear within the strands with a separation $\Delta L$ that drops

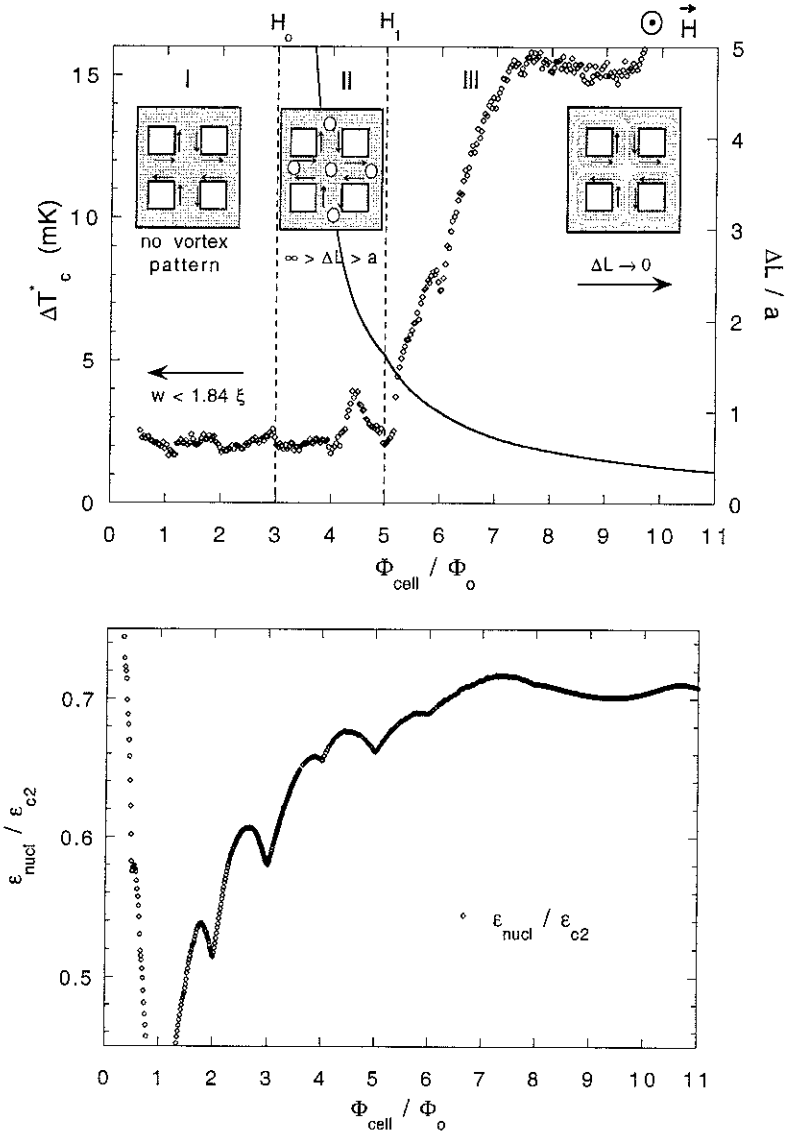


Figure 4.4: a) Resistive transition width $\Delta T_c^*$ of array A (open diamonds) as a function of the reduced flux $\Phi_{cell}/\Phi_o$, and comparison with the normalized distance $\Delta L/a$ between interstitial vortices for a thin wire (solid line). An oversimplified picture of the vortex patterns developed within the wires is represented. Three main regions can be identified: (I) $w < 1.84\xi(T)$, nucleation starts symmetrically and there is no vortex in the wires; (II) $w > 1.84\xi(T)$ and $\infty > \Delta L/a \leq 1$, nodes of the order parameter appear at interstices due to the interference of neighbor edge wave functions (white dots); (III) $\Delta L/a < 1$ and decreases with increasing field until the surface solutions become independent and the single edge states are localized around each hole. b) field variation of the nucleation energy $\epsilon_{nucl}/\epsilon_{c2}$ for array A.

from infinity to values comparable to the array lattice parameter. In this regime there will be a competition between increasing the flux per hole by $\Phi_o$ or follow the increase of field by accommodating vortices at interstitial positions in the array wires. The increase of the transition width for $\Phi_{cell}/\Phi_o$ between 4 and 5 illustrates the presence of a few loosely bound vortices. This observation is in agreement with Fig. 4.4.b) where the field dependence of $\epsilon_{nucl}/\epsilon_{c2}$ represented as a function of $\Phi_{cell}/\Phi_o$ shows that $\epsilon_{nucl}/\epsilon_{c2}$ at $\Phi_{cell}/\Phi_o = 4$ is higher than the adjacent dips. At $\Phi_{cell}/\Phi_o = 5$ every hole encloses 4 $\Phi_o$ which favors the decrease of $\epsilon_{nucl}/\epsilon_{c2}$. Also, the distance between vortices in the strands should be of the order of $a$ and, in that case, they can occupy positions at the array interstices forming a stable sub-lattice, which decreases the resistive transition width.

In region III, the distance between interstitial vortices should drop below $a$ and the transition width broadens considerably due to these weakly bounded vortices. The distance between nodes is further reduced with increasing field until edge states at each hole become independent.

We can see from Fig. 4.4.b) that at $\Phi_{cell} = 8\ \Phi_o$, the field modulation of $\epsilon_{nucl}/\epsilon_{c2}$ inverts concavity once the single hole nucleation becomes dominant. If for $\Phi_{cell}/\Phi_o$ between 5 and 8, the additional flux occupies interstitial positions, the flux per hole remaining equal to 4 $\Phi_o$, $\epsilon_{nucl}/\epsilon_{c2}$ should meet the single hole curve at its $4^{th}$ oscillation, in agreement with the results presented on Fig. 4.2.

## 4.4 Weak link array of edge states

We do not expect the description of a wire network of wide strands to hold if holes edges are pulled apart and/or shaped to circles. This is the case of sample B where the minimum inter-hole distance is $w = 4.74\ \mu$m ( $\sim$ twice compared to array A). The field for symmetric nucleation is $H_o \approx 0.08$ mT for a stripe with the same thickness. However since the distance between hole edges is not constant (varying from 4.74 to 9 $\mu$m around the hole perimeter) $H_o$ should be further reduced. As a consequence the parabolic envelope of $\epsilon_{nucl}$ is not observed. The coupling between neighbor edge states is still present though. Fundamental dips of $\epsilon_{nucl}$ at integers values of $\Phi_{cell}/\Phi_o \leq 7$

are clearly observed although we find no fine field structure. [3] At low field $\epsilon_{nucl}/\epsilon_{c2}$ is lower than the single hole calculation indicating that the energy contribution due to the overlap between edge states is important.

In the next sections we present a simple model which is able to capture the transition from the single hole to the collective behavior for array B. The application of this model is based on the assumption that in a narrow temperature region $T_{c2} < T < T_c^*$ the superconducting edge states are localized close to the hole boundaries and the system behaves like an array of weak links. The fast oscillations observed at low fields are then related to the collective behavior of the array. Since there is nonzero overlap between the wave functions of different edges, the energy should be higher than that of a single hole. One consequence is that the nucleation field $H_{c3}^*$ is lower than that of a single hole, as it is observed in the experiments. The single hole behavior is naturally recovered at higher fields where the overlap between neighboring edges vanishes.

A Ginzburg-Landau approach is suitable to study the problem. For the single hole, an analytical solution is available due to the cylindrical symmetry of the problem [31, 32]. A variational approach for the determination of the order parameter has been analyzed by Buzdin [18]. The agreement with the exact solution is good except at low fields where the variational approach predicts a region with zero flux through the hole which is not present in the exact solution. Buzdin's variational approach, however, has the great advantage of being applicable also in the many holes case where an analytical solution is impossible to obtain.

We proceed as follows. We first describe an improved variational ansatz for the single hole case by using a trial order parameter of three parameters. We then construct an effective Ginzburg-Landau free energy which takes into account, in an approximate way, the edge coupling and we determine the resulting nucleation energy.

[3] The absence of fine field structure could be interpreted has due to the presence of coherence only at a first neighbors level or due to the amplitude oscillations being smaller than our temperature resolution.

### 4.4.1 Variational approach : single hole

In this section we introduce the new variational wave function for the evaluation of the nucleation energy in a superconducting film containing a hole. Following Buzdin [18], the Ginzburg-Landau free energy ( $\mathcal{F}_N$ is the free energy of the normal state) is given by

$$\mathcal{F} - \mathcal{F}_N = \frac{\hbar^2}{4m} \int d^2r \left[ \left| \left( -i\nabla - \frac{2\pi}{\Phi_o} \mathbf{A} \right) \psi(\vec{r}) \right|^2 - \frac{1}{\xi^2} |\psi(\vec{r})|^2 \right] \tag{4.4}$$

The fourth order term has be ignored since we are interested in the phase boundary. The surface critical field can be determined with a variational procedure by determining the minimum of the functional

$$\mathcal{F} - \mathcal{F}_N = 0 \tag{4.5}$$

within the class of trial wave functions $\psi(\vec{r})$ which satisfy the proper boundary condition at the superconductor-insulator interface

$$\left[ \frac{\partial \psi}{\partial \rho} \right]_{\rho=R} = 0 \tag{4.6}$$

where $R$ is the radius of the hole. For a hole containing $m$ flux quantum, the order parameter has the following form in cylindrical coordinates ($\rho$, $\phi$, $z$),

$$\psi = \frac{1}{\sqrt{2\pi}} F(\rho) e^{im\phi}$$

It is possible to improve the result obtained by using a three-parameters trial order parameter of the form [4]

$$F(x) = \left[ 1 + \alpha(x - x_0)^\eta + \beta(x - x_0)^\zeta \right] \exp\left[ -\frac{\gamma}{2}(x - x_0)^2 \right] \tag{4.7}$$

where $\alpha, \beta, \gamma$ are the variational parameters and the dimensionless quantities $x = \rho(eH/c\hbar)^{1/2}$, $x_0 = R(eH/c\hbar)^{1/2} = (\Phi_{hole}/\Phi_o)^{1/2}$ has been introduced.

For the case of a single hole an exact solution for the nucleation energy is expressed in terms of the eigenvalues of the Kummer's equation [31, 32, 33]. We compare our results (the best results have been obtained for $\eta = 2$ and $\zeta = 2.05$) with the

[4] Buzdin has chosen a trial form of the type $F(x) = \exp\left[ -\frac{\gamma}{2}(x - x_0)^2 \right]$.

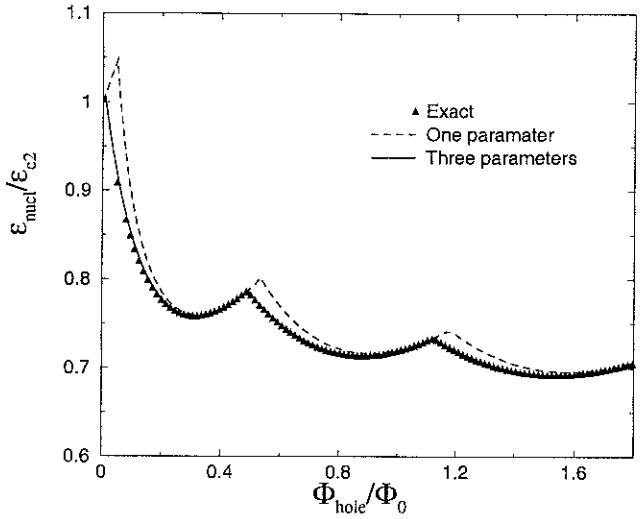


Figure 4.5: Variational approximations for $\epsilon_{nucl}/\epsilon_{c2}$. The thick curve is obtained using the three parameter variational wave function. For comparison the curve obtained from the one parameter variational function is reported (dashes line).

exact calculation and with the one parameter trial function [18]. This is shown in Fig. 4.5. The trial function $F(x)$ given by Eq. (4.7) has a maximum at $(x - x_0)^2 \sim (2 - \gamma/(\alpha + \beta))/\gamma$, a feature which is also present in the exact solution. This seems to improve considerably the accuracy of the variational approach [34].

The result obtained by using Eq. (4.7) improves considerably the agreement with the exact solution. In particular the spurious $m = 0$ is shrunk to very low fields ($< 0.03\ \Phi_o$).

### 4.4.2 Variational approach : array of holes

We obtain an approximate expression of the nucleation energy for a regular array using the variational wave function introduced in the previous section and an appropriate Ginzburg-Landau free energy which takes into account the overlap between edge states of adjacent holes. The model is sketched in Fig. 4.6, we will consider an array of edges connected by weak links (dashes lines in the figure). The crossover between the single hole and the collective behavior stems from the interplay of flux quantization on each hole and frustration effects through the elementary array cell.

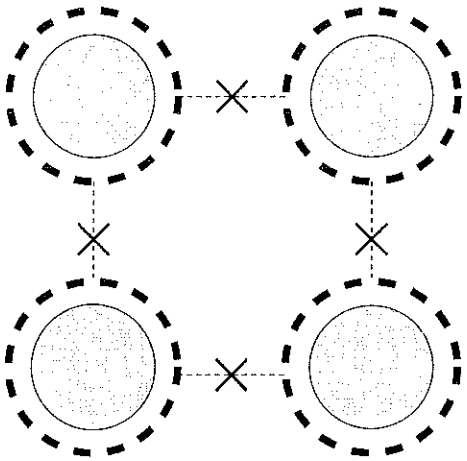

Figure 4.6: Elementary cell of a square array of holes (grey circles). The edge states localized around each hole (thick dashes lines) are weakly coupled to first neighbor edge states. The coupling is indicated with crosses.

The GL free energy which we propose has the following form

$$\mathcal{F} - \mathcal{F}_N = \sum_i \mathcal{F}_i + \sum_{\langle i,j \rangle} \mathcal{F}_{ij} \tag{4.8}$$

where $\mathcal{F}_i$ is the free energy defined in Eq. (4.4) and the subscript $i$ identifies the hole in the array. $\mathcal{F}_{ij}$ takes into account the overlap between the holes.

We choose a $\mathcal{F}_{ij}$ of the following form

$$\mathcal{F}_{ij} = \frac{\hbar^2}{4ma^2} \int d^2r \left[ \alpha_o \left| \psi_i(\vec{r}) - \psi_j(\vec{r}) \right|^2 + (\alpha_1 + \alpha_2 \delta_{ij}) \left| \psi_i(\vec{r}) \right| \left| \psi_j(\vec{r}) \right| \right] \tag{4.9}$$

The effect of the external magnetic field will be included in Eq. 4.9 by means of a Peierls substitution. We assume that the overlap is restricted to a small area (see the dashes lines in Fig. 4.6) and that the hole array can be treated as a weak link array. The first term in Eq. 4.9 is modified as follows

$$|\psi_i - \psi_j|^2 \rightarrow |\psi_i|^2 + |\psi_i|^2 - 2|\psi_i||\psi_j| \cos(\phi_i - \phi_j - \pi m - A_{ij}) \tag{4.10}$$

where $A_{i,j} = (2\pi)/(\Phi_o) \int_i^j \mathbf{A} \cdot d\mathbf{l}$ is calculated along the path indicated by the dashes lines in Fig. 4.6 (we assumed that all the holes contain the same number $m$ of flux quantum).

The terms in Eq. 4.9 can be understood considering that the order parameter in the array of holes can be given as $\psi = \sum_i \psi_i$. Substituting this expression in the

GL free energy of Eq. 4.4, one generates the various terms given above. In general since the approach is phenomenological, the various contributions enter with different coefficients $(\alpha_o, \alpha_1, \alpha_2)$. It is important to stress that the total wave function does *not* satisfy the proper boundary conditions around the holes because of the exponential tails of the edge states of the neighboring island. Therefore this approach breaks down at very small field when the overlap becomes too strong.

The agreement of the experiments with the single hole result in the high flux regime indicates that phase fluctuations do not drive the phase transition. In this case we can approximate the phase dependent part of the free energy by its ground state energy

$$\epsilon(\Phi_{cell}/\Phi_o) = \frac{2}{zN}\sum_{\langle i,j\rangle}\langle\cos(\phi_i - \phi_j - \pi m - A_{ij})\rangle_{GS}$$

where $N$ is the number of holes in the array, $z$ is the coordination number, $\Phi_{cell}/\Phi_o$ is the magnetic flux per elementary cell of the array and $\langle\ldots\rangle_{GS}$ means the ground state configuration of the phases $\phi_i$.

Going over the same steps as Buzdin [18] the nucleation energy for an array of holes is obtained by minimizing the following functional over the trial function introduced in Eq. 4.7

$$\begin{aligned}\frac{\epsilon_{nucl}}{\epsilon_{c2}} &= \mathcal{I}\int_{x_0}^{\infty}\frac{dx}{x}\left[(m-x^2)^2F^2(x) + x^2[F'(x)]^2 + g\frac{R^2}{a^2}\frac{1}{4x_0^2}x^2[F(x)]^2\right] \\ &+ g_1\frac{R^2}{a^2}\frac{1}{4x_0^2}\left[2 - g_2\,\epsilon(\Phi_{cell}/\Phi_o)\right]\langle F(x_i)F(x_j)\rangle \qquad (4.11)\end{aligned}$$

where the overlap integral

$$\langle F(x_i)F(x_j)\rangle = \mathcal{I}\int d\vec{x}F(\vec{x})F(\vec{x}+\frac{\vec{w}}{x_0}) \qquad (4.12)$$

the normalization

$$\mathcal{I}^{-1} = 2\int_{x_0}^{\infty} dx\; xF^2(x)$$

has been introduced. The new parameters $g, g_1, g_2$ are easily expressed as a function of the $\alpha$'s.

In Fig. 4.7 we present the results obtained for various values of the three parameters $g$,$g_1$ and $g_2$. We can observe that the presence of the Josephson coupling increases the array nucleation energy, relatively to the isolated hole case, and introduces cusps

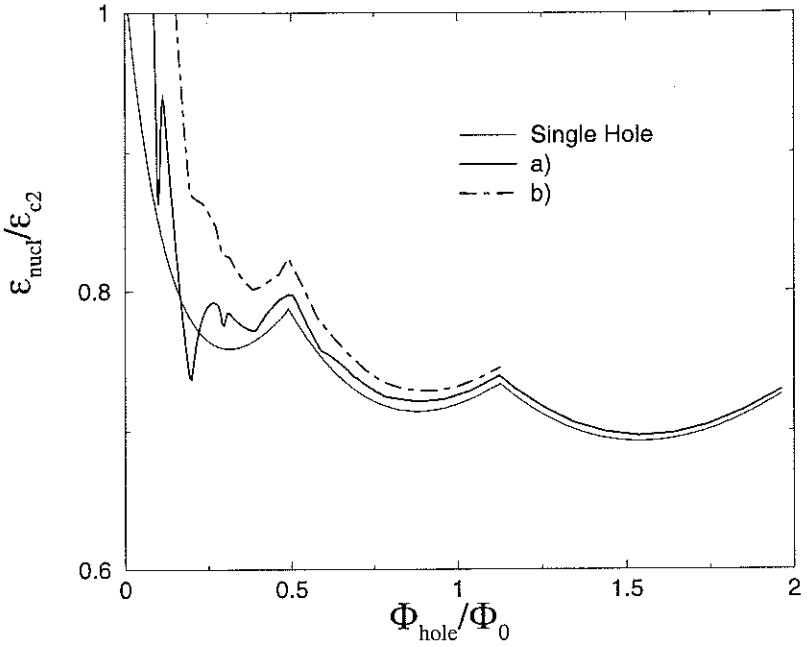


Figure 4.7: The normalized nucleation energy $\epsilon_{nucl}/\epsilon_{c2}$ for a regular array of holes obtained by minimizing the functional as defined in the text for various parameter values: a) g=0.1 g1=0.4 g2=1.6; b) g=0.2 g1=0.7 g2=0.9.

of different concavity superimposed over the main single hole background at low flux when the coupling becomes stronger. These features were found in the experiment of Bezryadin *et al* [14, 15]. At very low fields $\epsilon_{nucl}/\epsilon_{c2}$ rapidly increases, as also seen in the experiments. It may be explained by the fact the wave functions extends over various lattice constants and therefore the system does not show any surface superconductivity. However this model breaks down at flux typically of the order of 0.15 $\Phi_{hole}$.

A word of caution is needed at this point. Although the main features of the crossover are found one should be aware that the model is still too simplified to aim at a quantitative comparison with the experiments. In particular the choice of the values of the constants $g$ is not related to any microscopic model which allow to justify the numerical parameters. It is, however, rewarding that most of the qualitative features are captured by our model. A further step might be to apply the techniques developed by Palacios *et al* [35] to the present problem.

## 4.5 Conclusion

In conclusion, we tried to show how geometric parameters such as the inter-hole and the array lattice constant can influence the transition temperature of periodic superconducting arrays in a magnetic field.

We found a clear crossover with decreasing field from a single to a coupled edge state regime for both samples. The behavior of $\epsilon_{nucl}/\epsilon_{c2}$ in the single edge regime is very similar and the arrays transition depend exclusively on the magnetic flux per hole area. However, we remark that a quantitative comparison of the energy ratios $\epsilon_{nucl}/\epsilon_{c2}$ between samples need some caution since they are extremely dependent on the estimation of $\xi(0)$ and small errors can lead to a shift of the $\epsilon_{nucl}/\epsilon_{c2}$ values.

The low field behavior of the studied samples is representative of two distinct coupled systems: the superconducting wire network (strong coupling) and the weak link array. In both cases the coupling is mediated by the frustration induced by the applied field over the array elementary cell, however the type of coupling depends on the inter-hole distance $w$, the defect shape and the coherence length at $T_c^*(H)$ which controls the edge nucleation process. In the case of the weak link array (array B) we have a coupling of single hole edge states which depend on H through the enclosed flux per hole. However, in the low field regime, the enclosed flux does not necessarily follow the field increase since the change of the hole winding number may be less favorable than placing flux at the array interstices where superconductivity is weakened. In the wire network case (array A at low fields), we have a strong coupling of the order parameter at the array nodes, which is non-zero along the wires due to symmetric nucleation. The flux enclosed per hole or per array cell are equivalent quantities as long as interstitial vortices are not allowed within the array strands. In this regime, the main contribution to the array transition comés from nucleation in the wires (which depends only on H).

This explains why the studied samples which have similar geometric ratios ($w/a \approx 2$ and $V_s/V_{cell} \approx 0.8$) exhibit such a different collective behavior. The relevant parameters are then the inter-hole distance (which allows two-boundary nucleation in a wide field regime for sample A) and the parallel hole edges which favor the thin wire nucleation. For periodic arrays of close enough ($w/\xi(T_c^*) < 1.84$) and parallel hole

edges, the coupling between edge states can be described as a wire network coupling and the array transition approaches the thin wire nucleation at low fields. As a consequence, the ratio $H_{c3}/H_{c2}$ ($\epsilon_{nucl}/\epsilon_{c2}$) in these arrays is not necessarily upper (lower) bounded by the surface sheath result $H_{c3}/H_{c2} = 1.69$ ($\epsilon_{nucl}/\epsilon_{c2} = 0.59$) or the single hole nucleation limit.

When two-boundary nucleation does not occur, due to a higher inter-hole distance and/or due to the hole shape, the wire network formalism is not suitable to describe the coupling between edge states, since the variations of the order parameter amplitude between holes cannot be neglected. In this case the array transition is dominated by single hole nucleation and we presented a coupling description, based in a weak link interaction between single edge states, which is able to recover the main features of the $T_c^*(H)$ line on the low field regime: the inversion of field modulation concavity and the presence of periodic upward cusps. In addition, it reproduces the experimental observation that the array transition occurs at temperatures below the single hole nucleation, since the array energy is increased due to the overlap between neighbor edge wave functions.

# Chapter 5

# Aharonov-Bohm cages in periodic potentials

Dans ce chapitre est présentée une étude expérimentale d'un nouveau phénomène de localisation induit par le champ magnétique dans un système d'électrons sur une classe de réseaux bidimensionels périodiques. Ce phénomène prévue en 1998 par J. Vidal *et al.* est due à une combinaison subtile entre l'effet d'un champ magnétique transverse et la topologie du réseau. Dans une description de liaisons fortes, quand le champ appliqué équivaut à un demi quanta de flux magnétique par cellule, la propagation des paquets d ondes dans le réseau est *localisée* dans des cages de taille finie due à des interférences destructives du type de Aharonov-Bohm.

Nous avons étudié ce phénomène en utilisant des réseaux de fils supraconducteurs comme système modèle. On examine tout particulièrement le comportement supraconducteur pour la *frustration* $f = 1/2$. Selon la terminologie en usage, la frustration $f = BS/\Phi_o$ est définie comme le rapport entre le flux magnétique appliqué par cellule du réseau (de surface $S$) au quantum de flux supraconducteur $\Phi_o = hc/2e$. La comparaison des résultats expérimentaux avec la théorie est faite dans le cadre d'un formalisme de Ginzburg-Landau linéaire pour les réseaux de fils. Nous avons effectué des mesures de transport à quatre fils et visualisé les configurations de vortex en utilisant la méthode de décoration de Bitter.

Pour les mesures de transport nous avons choisi des réseaux d'aluminium, lithographiés au CEA-LETI dans le cadre du programme PLATO. La ligne de transition de phase

et les courants critiques en fonction du champ ont été déterminés par des mesures de transport. Notamment ont pu être observés : (i) l'effondrement du courant critique à un demi quanta flux, phénomène unique dans un réseaux étendu qui contraste avec le renforcement habituellement observé à $f = 1/2$ dans les réseaux carrés ou triangulaires à cette valeur de champ; (ii) le minimum de la température de transition qui correspond au maximum d'énergie de l'état fondamental à demi flux. L'accord avec la théorie est excellent pour la température de transition mais seulement qualitatif pour le courant critique.

Pour les décorations de Bitter nous avons opté pour des réseaux en niobium, qui présentent une plus haute température critique. Des décorations de Bitter ont montré que la distribution des vortex à demi quanta de flux est très désordonnée, alors que les structures identifiés à $1/3$ et à $2/3$ quanta de flux sont ordonnées. Ces résultats constituent la première étude expérimentale de ce phénomène [36].

# Introduction

In this chapter we present an experimental study of a novel localization phenomenon induced by a transverse magnetic field. This effect was recently predicted by Vidal *et al.* [37] for a system of non-interacting electrons under a certain class of periodic two-dimensional networks and occurs when the applied flux is equal to a half of the single electron flux quantum per elementary cell (half-flux). This problem was treated for tight-binding electrons, and is a pure quantum interference phenomenon which arises due to the interplay between the network topology and the applied field. The effect of the transverse magnetic field is to introduce a phase shift on the electron wavefunction. The network restricts the available electron paths and due to its special geometry, at half-flux all available paths will interfere destructively at some node of the network and not very far the departure site. At this flux the propagation of an electron wavepacket in the infinite periodic potential will be bounded within a *cage* of a few cells length due to an effective cancellation of some hopping terms. This effect can thus be simply understood in terms of destructive quantum interference of the Aharonov-Bohm (AB) type.

The singular feature of this phenomenon is that this AB type interference occurs on an infinite periodic network at a commensurate magnetic field, which so far was unknown to occur on other regular periodic geometries, such as the square or the triangular lattices. It also differs from Anderson localization on two essential points: it occurs in a pure system, without disorder, and the confinement at half-flux is a consequence of the non-dispersing character of the system eigenstates at this field. This point will be discussed later, since one of the remarkable findings of Ref.[37] is the total absence of dispersion in the TB spectrum at half-flux.

The experimental system one could think of firstly to study this problem is an anti-dot array on a two dimensional gas [38]. However, in these systems the ballistic regime may be difficult to attain since the electron wavelength does not exceed a few tens $nm$ even in very low carrier density hetero-structures. Our experimental approach consisted in using 2D superconducting (Sc) wire networks. These systems have been widely used has model systems of tight-binding electrons on two-dimensional spatially modulated potentials [39]. We exploit the well known mapping of the TB problem into the linearized Ginzburg-Landau description of wire networks [40, 19] to inspect some of the novel features introduced by this phenomenon in the one-particle energy spectrum. Another advantage of using Sc wire networks is that the quantum regime is accessible even in low $T_c$ diffusive superconductors. Since all Cooper pairs condense in a single quantum state, the relevant wavelength is associated with the macroscopic superfluid velocity and can be much larger than the lattice elementary cell [38]. Also, the magnetic field corresponding to one superconducting flux quantum $\Phi_o = hc/2e$, is easily accessible in a Sc wire network: for a network unit cell of 1 $\mu$m$^2$ surface it is about 1 mT, in contrast to the high value of $10^3$ T for an atomic lattice.

How should we understand this effect in the context of a Sc wire network?

As we will see later, the main signatures of this localization effect are the non-dispersing character of the system eigenstates (absence of band structure) at half-flux, and its ground state which is infinite degenerate and displays the absolute maximum energy, in comparison to other fields.

In the context of a Sc wire network, the ground state maximum energy is expressed on a maximum depression of the field dependent superconductor transition. The

non-dispersing and the infinite degenerate ground state are features related with the wave packet confinement, that is, with the propagation of phase information over the network. Therefore, on a Sc wire network we expect a weakening of the transport critical current at half-flux. In fact, a Sc wire network can be described as an array of strongly coupled Sc islands, with an order parameter (phase and amplitude) defined on each of them, therefore the ground state energy is strongly dependent on the phase configuration and on the applied field. The infinite degeneracy and non-dispersivity at half-flux means that there is no groundstate configuration, therefore if a phase twist occurs on some point of the network, it should not be followed by a phase change in the rest of the system. On the other hand, the absence of phase coherence at half-flux led us to expect that the vortex configurations, which are determined by the distribution of single loop supercurrents, would be very disordered in opposition to the ordered structures expected at other commensurate fields.

We thus studied the transport properties of 2D superconducting wire networks on aluminium, with particular emphasis on the normal to superconducting transition and the transport critical currents in applied field. These measurements are performed in a temperature regime close to the transition, which is the validity regime of the linearized GL description we use. Our experimental results are presented on Sec. 5.4 and were compared with the theoretical predictions. For the transition line we found an excellent quantitative agreement. For the critical current the agreement is only qualitative, which we believe to be a consequence of the limitations of the linearized GL approach. The vortex distributions at half-flux were visualized by Bitter decoration experiments on niobium wire networks. Our results are discussed in Sec. 5.6. The vortex distributions at half-flux were indeed very disordered, supporting the picture of the absence of phase coherence at this field.

In this study we used Sc wire networks of different superconducting metals, the choice being mainly based on the type of measurements to be performed. The decoration experiments are performed at 4.2 K, therefore a Sc wire network with higher transition temperature is needed. We chose niobium since it becomes superconducting around 9.2 K and we can do high quality epitaxial niobium films. As for the transport measurements, the cryostat has a wider working temperature range (from

0.3 K to 10 K) but the networks surfaces must be large (for ex. of about 1 $mm^2$ surface for a 1 $\mu$m lattice constant) to avoid parasitic effects from its borders and very homogeneous to avoid effects from disorder which could mask the effect we are looking for. The most suitable way to pattern wire networks of short wire width is lift-off. Moreover, the coherence length $\xi$ of the material must be large in order to have a two-dimensional network in a wide temperature range (wire width larger than $\xi$) and to maximize the amplitude of the field dependent transition temperature, which is proportional to $\xi/a$ ($a$ is the lattice constant). For these reasons niobium was discarded. We chose aluminium, due to its coherence length of 0.2 $\mu$m which gives a comfortable range for the sample dimensions. The geometric requirements for these arrays (large total surface, small wire width, high isotropy) were however beyond the possibilities of our lithography tools. The lithography of these networks was then performed by the CEA-LETI working teams and tools.

Before the presentation of the experimental results, we described in more detail in the next section the localization effect we studied. The formalism which enables the mapping of the TB problem into the linearized Ginzburg-Landau description of 2D Sc wire networks will be presented on section. We will also briefly review some aspects of the AB effect in finite loop geometries, which will be used for comparison with the network behaviour at half-flux.

## 5.1 Aharonov-Bohm cages

In this section we highlight the main aspects about the so-called Aharonov-Bohm cages. This denomination was introduced in Ref. [37] by the authors to stress the nature of this quantum effect which, such as in the in the well known AB effect [41], is entirely due to quantum destructive interference. The singular feature however, is that it occurs on an infinite periodic network, in contrast to the original AB on finite single loop geometries. In a single loop geometry, all electron paths enclose the same flux. The phase shift $\gamma_{ij}$ of the electron wave function acquired between two sites $i$ and $j$ is given by the line integral of the vector potential along that path, $\gamma_{ij} = (2\pi/\Phi_o)\int_i^j \mathbf{A}d\mathbf{l}$. Two symmetric paths (clockwise and counterclockwise)

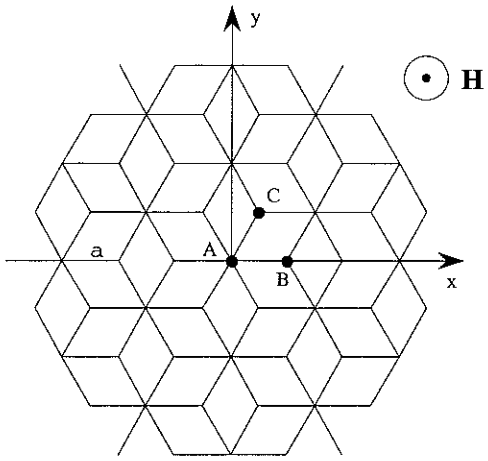


Figure 5.1: $T_3$ topology.

enclosing the same flux will interfere destructively at half-flux. In an infinite 2D network there are multiple electrons paths available. In a tight binding description, in zero field the electron waves scattered by the periodic potential exhibit the same periodicity as the underlying lattice and add constructively for all allowed wave-vectors $k$ (k belonging to the first Brillouin zone). These are the well known Bloch states. In the absence of disorder, the momentum of a Bloch electron in the energy level $\epsilon_n(k)$ is given by the group velocity $v_n(k) = (1/\hbar)\nabla_k\epsilon_n(k)$, therefore as long as $\nabla_k\epsilon_n(k)$ is non-zero, the electron moves in the underlying potential without any degradation of its mean velocity.

In a non-zero transverse magnetic field, the phase of the electron wave function is shifted. However in periodic lattices at some values of applied flux, called commensurate, constructive interference still exists. However, as recently shown [37], in a class of 2D periodic networks quantum interferences are fully destructive when the applied flux per cell is equal to half a flux quantum. The simplest geometry of this class, which is the one we studied, is displayed in Fig. 5.1. This structure, which we will denote $T_3$, is a periodic tiling with hexagonal symmetry composed of rhombus tiles of side length $a$, with 2 sites of different coordination: a 6-fold coordinated (site A) and a 3-fold coordinated site (sites B and C). The reduced flux per cell is $f = Ba^2\sqrt{3}/2$.

The interaction of the charged particle with the network is described by the tight binding hamiltonian :

$$H = \sum_{<i,j>} t_{ij}|i><j|, \tag{5.1}$$

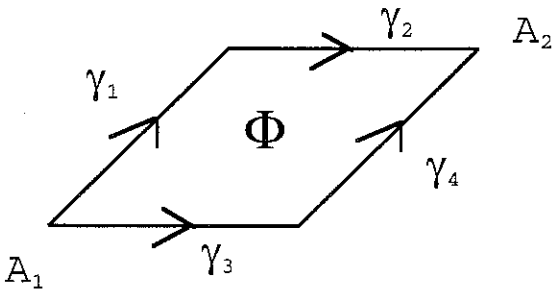


Figure 5.2: Phase shift $\gamma_i$ acquired by the electron wave-function when going from site $A_1$ to site $A_2$ and enclosing a transverse magnetic flux $\Phi$.

where $|i>$ is a localized orbital on site $i$, and the hopping term between sites $i$ and $j$ is given by the phase factor $t_{ij} = e^{-i\gamma_{ij}}$, with $\gamma_{ij} = (2\pi/\Phi_o)\int_i^j \mathbf{A}d\mathbf{l}$. Only first neighbour hopping is considered.

We can intuitively understand the meaning of the bounded cages in terms of AB effect by observing the $T_3$ topology (see Fig. 5.3). The key point about this geometry is the mix coordination of its sites, each site being surrounded by sites of different coordination, though all at the same distance.

Lets consider first a single tile and the phase shift acquired by the wave-function when going from one site to the next due to a non-zero enclosed flux $\Phi$ (see Fig. 5.2). If $\gamma_1$, $\gamma_2$ are the phase shifts acquired on the upper branches and $\gamma_3$, $\gamma_4$, those acquired in the lower branch, we can see that

$$\gamma_1 + \gamma_2 - \gamma_3 - \gamma_4 = 2\pi\frac{\Phi}{\Phi_o} = 2\pi f \tag{5.2}$$

with $\gamma_1 = \gamma_2 = -\gamma_3 = -\gamma_4 = \gamma/2 = (2\pi/\Phi_o)\int_i^j \mathbf{A}d\mathbf{l}$ whatever the applied flux. The phase shift acquired when going from site $A_1$ to $A_2$ from the upper path is then $e^{i\,\gamma}$ and from the lower path $e^{-i\,\gamma)}$, and they interfere at site $A_2$ giving,

$$e^{i\,\gamma} + e^{-i\,\gamma} = e^{i\,\gamma}[1 + e^{-2i\,\gamma}] \tag{5.3}$$

which is zero at half-flux, when $\gamma = \pi/2$. If now we consider the $T_3$ tiling, we can see that the same will happen to every electron path leaving a 6-fold sit once the nearest 6-fold site is reached, and the interference at half-flux will be fully destructive. Therefore the AB cage for a wave packet initially localized on a 6-fold site is delimited by the nearest 6-fold sites. In the same manner, if a site 3-fold is chosen, there are 3

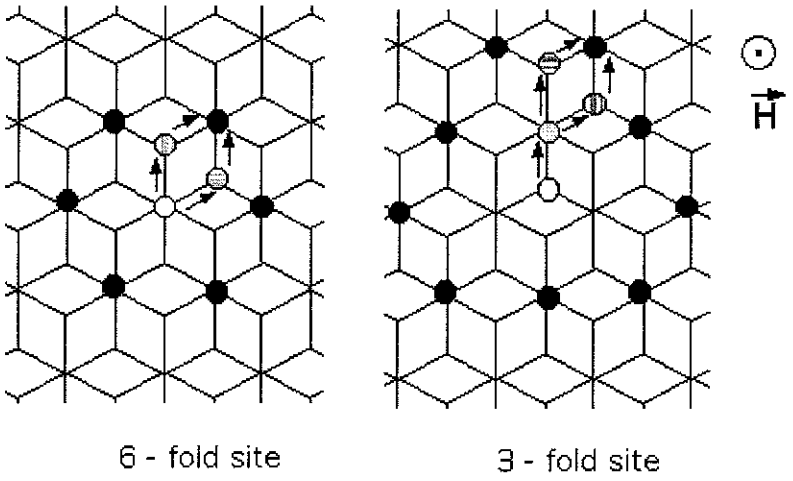


Figure 5.3: AB cage for different initial (open dot) sites of coordination 6 and 3, respectively. The black dots denote the intersection points where fully destructive interference occurs at half-flux, that is the cage.

unidirectional paths for two consecutive hoppings which do not intersect. However, once the 6-fold site is reached, the hopping will be inevitably bounded at the nearest 6-fold sites. For the 3-fold site the cage is larger but still finite. The AB cages for the two types of initial sites are displayed in Fig. 5.3. Moreover, for any finite linear combination of wave packets located in different sites, its propagation will be confined in space, the correspondent cage being included in the union of all individual cages. Two cages which do not overlap will be completely decoupled. This simple picture illustrates the meaning of the non-dispersive state at half-flux. Once a wave packet reaches the AB cage boundary, it is "reflected" backwards without sending any phase information outwards.

This situation is not unique to 2D geometries, though it is for periodic lattices, such as the square and the triangular lattices, for which the wave packets can propagate to infinite at all rational frustrations. Other geometries, such as the Penrose lattice, have some bounded cages at some frustration values, however the effect is not as drastic has for the $T_3$ tiling, for which all cages are bounded at half-flux.

## The effect of disorder

The effect of disorder in the bounded AB cages was also addressed by Vidal *et al* [37], for some cases of positional disorder or electron-electron interactions. In this system disorder seems to delocalize (as in quasi-crystals), though intuitively one might be led to think that disorder should lead to localization. In principle, all types of disorder which disturb the electron paths may destroy the fully destructive interference at half-flux. When a interaction between two electrons is considered, it seems to destroy the bounded cages, or at least, the wave packet is able to spread over more sites than in the absence of interactions. As for positional disorder, the inclusion of a few defects (such as reversing a few dices in the network) though disturbing locally, do not destroy the wave packet bounding, which is recovered once a defect free region is reached. On the other hand, a random distribution of disorder with a finite density may indeed destroy the localization effect.

## The energy spectrum

In this section we will see how this phenomenon affects the one-particle energy spectrum in the $T_3$ geometry. It is well known that on 2D lattices, at commensurate fields, that is, when the reduced flux per cell is a rational $f = p/q$ (p,q integers), the interplay between field and topology leads to exotic features in the one-particle energy spectrum, with the formation of a structure of bands as in the well-known Hofstadter's butterfly spectrum for the square lattice. The particular details of the energy spectrum depend on the network geometry and the applied field, however the spectrum of periodic lattices such as the triangular, the square, and the hexagonal lattices share some common features. Firstly, it depends on applied field exclusively through the reduced flux per elementary cell or frustration, being periodic on $f = \pm 1$ and with reflection symmetry about $f = 1/2$. Frustration is simply defined as the reduced flux per elementary cell, $f = BS_{cell}/\Phi_o$, where B is the magnetic induction field and $S_{cell}$ the elementary tile surface. Moreover, at rational frustration values, besides the presence of a band structure, the ground state level presents an oscillating field modulation with downward local minima, the most important dips occurring at low order rationals.

In contrast, the $T_3$ spectrum shares these common features at all rationals except at $f = 1/2$. At half-flux the spectrum collapses into two infinite degenerate levels $\epsilon = \pm\sqrt{6}$ and the energy band vanishes. Besides, the ground state energy at half-flux is an absolute maximum in comparison to the values at other fields. These features can be clearly seen in Fig. 5.4 where the $T_3$ spectrum is displayed as a function of reduced flux per unit cell.

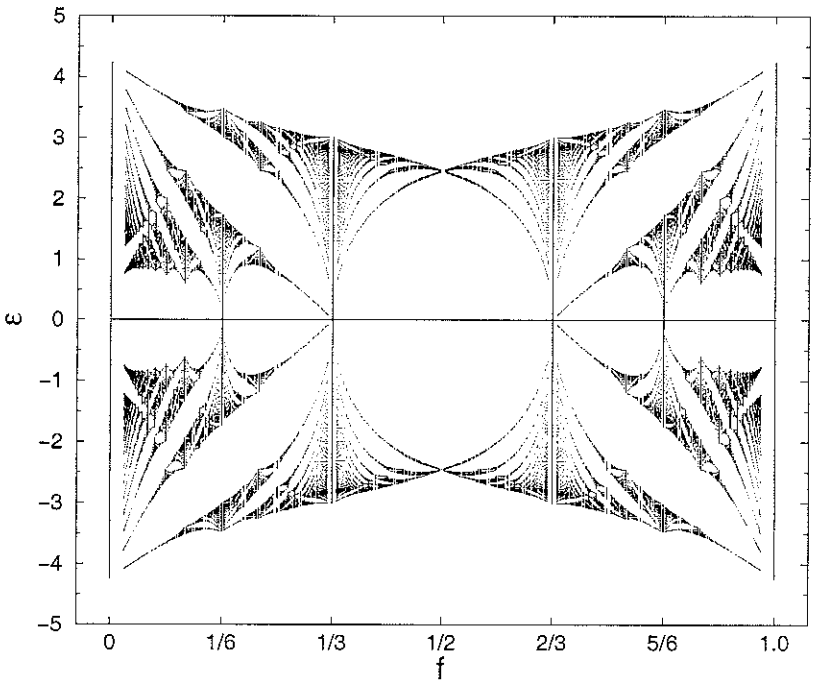


Figure 5.4: Eigenvalue spectrum as a function of frustration (rational values) of a single particle in a 2D tight binding potential with the $T_3$ topology [42].

The details of the spectrum calculation can be found in Ref. [37]. Using a Landau gauge $\mathbf{A}$ =Hx$\mathbf{u}_y$ ($\mathbf{H}$ =H$\mathbf{u}_z$), the system has translational invariance in the $y$ direction and the wave-functions along the wires could be written as, $\psi(x,y) = \psi(x)e^{ik_y y}$ with $k_y \in [0, 2\pi/\sqrt{3}a]$. With this gauge choice the eigenvalue problem was first reduced to a system of three 1D equations (one for each site A,B and C), coupling the wave functions at each node to its first neighbours. Denoting each site as $(x = ma, y = ma)$, and the wave function amplitude at site (j,n) as $\psi(ja)$=$\psi_j$, the set of 1D equations was then reduced to a single eigenvalue equation where only the wave functions at

the 6-fold site appear,

$$(\epsilon^2-6)\psi_m = 2\cos\left(\frac{\gamma}{2}\right)\left(2\cos\left(\frac{3\gamma}{2}(m+\frac{1}{2})+\kappa\right)\psi_{m+1}\right.$$
$$\left.+2\cos\left(\frac{3\gamma}{2}(m-\frac{1}{2})+\kappa\right)\psi_{m-1}+2\cos\left(3\gamma m+2\kappa\right)\psi_m\right) \quad (5.4)$$

where $\psi_m = \psi(x_A)$ is the wave function at site A ($x_A = 3ma/2$, m$\in$ **Z**), $\kappa = k_y\sqrt{3}/2$, $\gamma = 2\pi f$, and $\epsilon$ is the energy eigenvalue of the 2D problem.

From this relation we can already see that, due to the $\cos(\gamma/2)$ factor, the eigenvalue relation is reduced to $(\epsilon^2-6)\psi_m = 0$ at half flux, having two infinite degenerate solutions $\epsilon = \pm\sqrt{6}$ (independent of $\kappa$). As pointed out in Ref. [37], the equation (5.4) is similar to those derived by Claro and Wannier for a triangular lattice [43] at frustration $f_T = 3/2f$ (that is, to the triangular lattice formed by 6-fold sites). Replacing $\gamma_T = 2\pi f_T = 3\gamma/2$, the eigenenergies of the two tilings are simply related (for $\epsilon \neq 0$) by,

$$\epsilon^2(\gamma) - 6 = 2\cos(\frac{\gamma}{2})\epsilon_T(\gamma_T). \quad (5.5)$$

The one-particle $T_3$ spectrum [37] displayed in Fig. 5.4, was calculated as a function of reduced flux per cell for $f = p/q$ with $q < 50$. For each field, the black dots represent the eigenvalue solutions for the allowed $\kappa$ values, while the empty regions correspond to gaps in the spectrum. We can see that at half-flux there is no energy band. In contrast, we identify energy bands at other rationals, in particular, at $f = 1/3$ there is one single band which crosses the whole spectrum. At some other rational reduced flux the bandwidth is very narrow but still non-zero. The absence of band structure implies that the group velocity will be zero for all $k$, thus the degenerate states at half-flux are non-dispersive states. At half-flux there is also the solution $\epsilon = 0$ which corresponds to a flat band. Another important feature of this spectrum is the field modulation on the ground state eigenvalues. At rational $f$ they are local minima (constructive interference), except at half-flux where an absolute maximum can be observed, also associated with an inversion of the field modulation concavity.

These features at $f = 1/2$ are completely absent from the spectrum of other periodic lattices at rational reduced flux, namely the triangular spectrum at $f_T = 1/4$, with whom the $T_3$ spectrum at half-flux can be related.

## 5.2 The Sc wire network as a model system

Some features of the TB spectrum, namely the Hofstadter butterfly [26], are experimentally accessible in the model system of a superconducting wire network[44, 45]. As shown by de Gennes and Alexander[40, 19], the linearized Ginzburg-Landau (GL) equations for a superconducting wire network can be mapped onto the eigenvalues equation of a TB hamiltonian for the same geometry.

The most important limitation to the use of superconducting wire networks is that the isomorphism between the linear GL formalism and the tight binding problem is only valid in a narrow temperature regime close to the network superconducting transition, which means that we can only inspect the energy spectrum very close to the ground state level. Though this is not limiting in what concerns the study of the ground state field modulation (given by the network transition line), a more careful discussion is needed in what concerns the inspection of the non-dispersive nature of the state at half-flux, which we shall analyse through the critical current data. Phase fluctuations are not taken into account in this regime.

Superconducting networks undergo a second-order phase transition on going from the normal to the superconducting state, the details of the transition being determined exclusively by the network topology: if the network is formed by tiles commensurate to each other, the phase boundary will exhibit a structure periodic on the fluxoid quantum $\Phi_o$.

It was shown by de Gennes and Alexander that if the network branches are one-dimensional (1D) in the G.L. context (that is, radius smaller than $\xi$ and $\lambda$) the circuit behaviour close to the transition can be described within mean-field theory. In this case, the order parameter is modulated along the 1D branches and the energy eigenvalues close to the transition are given by the linearized G.L. equation:

$$\left[i\frac{\partial}{\partial l} + \frac{2\pi A}{\Phi_o}\right]^2 \Psi(l) = \frac{\Psi(l)}{\xi^2(T)} \tag{5.6}$$

with superconductor-vacuum boundary conditions at the network A nodes,

$$\sum \left[i\frac{\partial}{\partial l} + \frac{2\pi}{\Phi_o}\right] \Psi(l) \mid_{\,l=0} = 0 \tag{5.7}$$

where the temperature dependent coherence length is $\xi(T) = \xi(0)/\sqrt{1 - T/T_c(0)}$.

The boundary condition yield two relations at each node: an imaginary part particular to superconductivity (the spatial gradient of the order parameter at the boundary) and a real part which expresses the conservation of the supercurrents entering each node.

This formalism corresponds to an eigenvalue problem in which the network transition temperature is the highest temperature for which Eq. (5.6) has a non-zero solution. The solution of the linearized equation leads to a modulation of the order parameter along the wire linking two nodes $i$ and $j$, $\Psi_{i,j}(l)$ given by,

$$\Psi_{i,j}(l) = \frac{e^{-i\gamma_{i,l}}}{\sin(a/\xi)} \left[ \Psi_i \sin(\frac{a-l}{\xi}) + \Psi_j e^{i\gamma_{i\ j}} \sin(\frac{l}{\xi}) \right] \tag{5.8}$$

$$\gamma_{i,l} = \frac{2\pi}{\Phi_o} \int_i^l A(s)ds \tag{5.9}$$

where $\gamma_{i,l}$ is the vector potential line integral between node $i$ and the position $l$ along the wire, and $a$ the distance between nodes. Applying the boundary conditions at each node we obtain the Alexander node equations:

$$\sum_{j=1}^{n} \left[ -\Psi_i \coth \frac{L_{i,j}}{\xi} + \Psi_j \frac{e^{-i\gamma_{i,j}}}{\sin(L_{i,j}/\xi)} \right] = 0 \tag{5.10}$$

where the summation is done over the $n$ first neighbour nodes surrounding the node $i$.

A classical example first treated by Alexander is the square wire network. In this case, every node is linked to four neighbours by branches of equal length $L_{i,j} = a$, and the node equation is reduced to a simple form:

$$4 \cos \frac{a}{\xi_k}\ \Psi_i = \sum_{j=1}^{4} e^{-i\gamma_{i,j}}\ \Psi_j \tag{5.11}$$

This equation is equivalent to a Schroedinger tight binding equation with energy eigenvalues $\epsilon_k = 4 \cos \frac{a}{\xi_k}$ and hoping terms $t_{i,j} = e^{-i\gamma_{i,j}}$.

For an infinite two-dimensional square potential, if we chose Landau gauge $\mathbf{A}$ = H x $\mathbf{u}_y$ along the y axis, the wave-function at node ($n_x$a, $n_y$a), can be written as a plane wave $\Psi_{n_x,n_y} = f_{n_x} e^{-in_y k}$ with $n_x$, $n_y$ integers, and the Alexander node equations are reduced to a 1D tight binding equation:

$$\epsilon_k f_{n_x} = f_{n_x+1} + f_{n_x-1} + 2\cos(k - n_x\ \gamma) \tag{5.12}$$

where the magnetic field enters through the phase $\gamma = 2\pi\Phi/\Phi_o$, where $\Phi = \mathrm{B}a^2$ is the magnetic flux threading a unit tile. At rational magnetic flux $\Phi/\Phi_o = p/q$ ($p$, $q$ integers) this equation is invariant under translation $n_x \rightarrow n_x + q$ and only $q$ equations are needed to obtain the energy eigenvalues. The structure of the energy band spectrum depend on the network topology, nevertheless two features are present on general lattices (square, triangular, honeycomb, ...): the energy spectrum at $\Phi/\Phi_o = p/q$ is constituted by $q$ energy bands, separated by energy gaps and the ground state (k=0) presents cusp-like minima at rational magnetic flux.

The superconducting critical temperature is obtained from the ground state eigenvalues $\epsilon_g$, by:

$$T_c(H) = T_c(0)\left[1 - \frac{\xi^2(0)}{a^2}\arccos^2\frac{\epsilon_g}{z})\right] \tag{5.13}$$

where $z$ is the lattice coordination ($z$=4 for a square lattice).

## 5.3 The superconductor Aharonov-Bohm analog

In this section we will briefly discuss some superconducting closed loop geometries under a transverse field for further comparison with the behaviour at half-flux of the 2D network. The analog of the Aharonov-Bohm effect in the superconducting case is the oscillation of the transition temperature as a function of applied field in closed loop geometries. In this case, the applied field induces a phase shift on the electrons of a Cooper pair (k,-k) which is expressed as a pair breaking energy. This energy is maximum at half-flux leading to a minimum of the transition temperature at this field, and periodic on $\Phi_o$. In the case of simple finite geometries, such as a Little-Parks ring or a dice (see Fig. 5.5, the transition line can be easily calculated applying the Alexander nodes equation. For a single ring of a 1D wire and perimeter $L$, there is only one node and the summation over nearest neighbours ,that is, the two symmetric paths $L_{i,i} = L$ linking the node to itself, leads to the well known Little-Parks oscillation:

$$1 - \frac{T_c(f)}{T_c(0)} = 4\pi^2 \frac{\xi^2(0)}{L^2} (f-n)^2, \tag{5.14}$$

with $n = 0$ for $f < 1/2$ and $n = 1$ for $f > 1/2$. At half-flux the transition temperature is a minimum since we then have an Aharonov-Bohm geometry with destructive interference.

In the case of a dice (four nodes) composed of three tiles of side length $a$, the eigenvalue problem is reduced to three solutions; the symmetric solution of the $3^{rd}$ order polynomial,

$$36\cos^3(\frac{a}{\xi}) - 12\cos(\frac{a}{\xi})(2+\cos\gamma) = \frac{1}{2}\cos(\gamma) - \cos^2(\gamma) + \frac{1}{2}, \tag{5.15}$$

valid at low fields and close to $f = 1$, where $\gamma = 2\pi f$; and the non-symmetric solutions being given by,

$$3\cos^2(\frac{a}{\xi}) - 1 = \pm\frac{\sqrt{3}}{2}\sin|\gamma| - \frac{1}{2}\cos(\gamma). \tag{5.16}$$

corresponding respectively to one or two flux quanta through the large exterior loop (the phase varies regularly around the exterior loop). At the central node the phase is ill defined at half-flux due to destructive interference at this node of the symmetric paths that encircle each tile. The transition line will be simply obtained from the lowest eigenvalues $a/\xi(T)$, as

$$1 - \frac{T_c(f)}{T_c(0)} = \frac{\xi^2(0)}{a^2} \tag{5.17}$$

The variation of the normal to superconductor transition for a Little Parks ring ($L = 4a$) and a dice are displayed in Fig. 5.5. The thick solid line represents the solutions in the dice geometry and thick dashes line for the 1D ring. Both present a clear minimum at half-flux, which for the dice corresponds to the intersection of the non-symmetric solutions centered at $f = 1/3$ and $f = 2/3$, respectively.

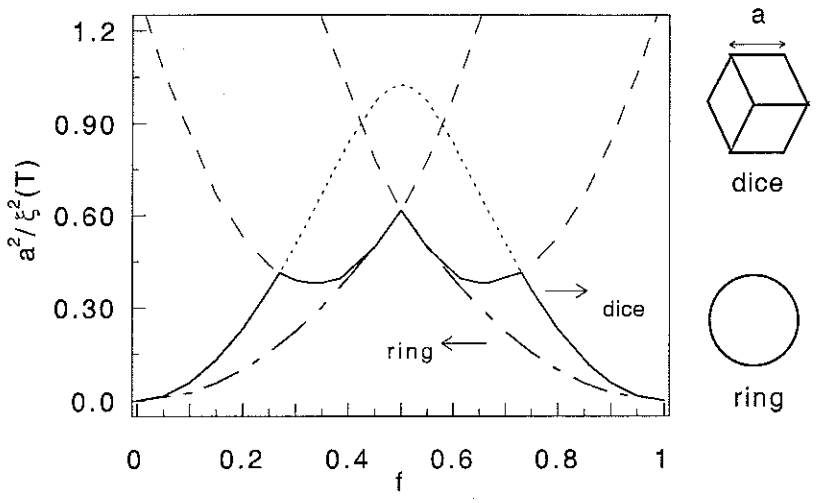


Figure 5.5: Normal to superconducting boundary of a superconducting 1D ring and a dice as a function of frustration. Both geometries present a maximum at half-flux due to Aharonov-Bohm destructive interference.

## 5.4 Transport Measurements

For the transport measurements we used superconducting networks of aluminium wires with the $T_3$ topology which are defined on a large patterned surface. We chose aluminium since for wires width of 100 nm and 80 nm thickness, the sample will display a 2D behaviour close to the transition temperature due to its large coherence length (of about 0.2 $\mu$m at zero temperature). We studied the superconductor-normal transition temperature of the networks as a function of applied field as well as the broadening of the transition width. Critical current measurements as a function of applied field and temperature were also performed. Finally, we also examined the characteristics voltage-current at certain field values.

These measurements were performed using an 33 Hz *ac* four terminal resistance bridge with measuring currents of less than 100 nA. The measurements are done in the $He^3$ cryostat described in Chap. 3 which allows a temperature stability of less than 0.1 mK in the temperature range from 0.3 K to 1.3 K. The samples are sticked to a copper sample holder with a polymer resist and sample probes connected to the cryostat terminals by ultrasound bounding of 25 $\mu$m gold wires.

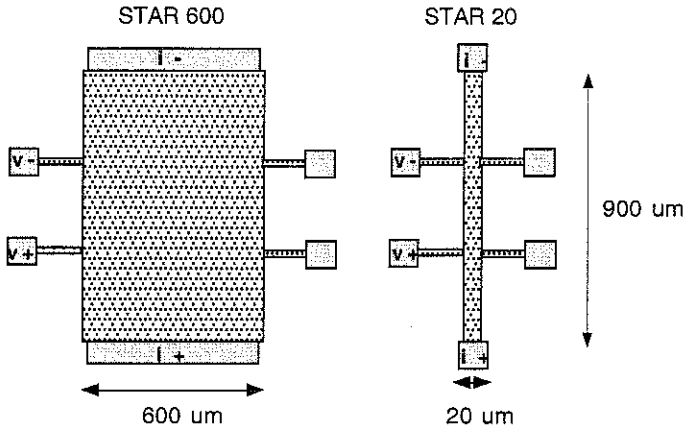


Figure 5.6: Scheme of the networks design and contact pads for transport measurements. The voltage plots have $50 \times 50$ $\mu$m$^2$ surface. The relative sizes of the several elements are not scaled.

### 5.4.1 Sample details

We designed two series of arrays with the same tile parameters but different patterned surface. Each network cell has a side length of $a = 1$ $\mu$m, the wires having 100 nm width and 100 nm thickness. The array used in transition line measurements was defined on a $0.6 \times 1$ mm$^2$ (array Star 600) whereas for the critical current measurements we used an array defined on a surface of shorter side length, $0.02 \times 1$ mm$^2$ (Star 20), to avoid heating effects due to feeding large currents. A scheme of the networks and the contacts position for Star 600 and Star 20 are displayed in Fig. 5.6.

The networks pattern was defined on a 600 nm thick layer of positive UV3 resist using an *e-beam* writer Leica VB6-HR. The large patterned surface required stitching and alignment of $200 \times 200$ $\mu$m$^2$ writing fields. A 100 nm thick layer of pure aluminium was *e-beam* evaporated in a ultra-high vacuum chamber, followed by the resist *lift-off*. The contact probes are aluminium rectangular pads located as illustrated in Fig. 5.7. The current pads are located on the shortest side of the array which ensure current injection in each wire in the direction indicated in Fig. 5.7. The voltage pads are located at 70 $\mu$m from the array sample and connected to it through patterned arms (10 $\mu$m width) to avoid invasive effects [1]. The distance between the voltage probes is approximately 580 $\mu$m, which corresponds to a measuring surface of $1.4 \times 10^4$ tiles for Star 20 and $4 \times 10^5$ tiles for Star 600.

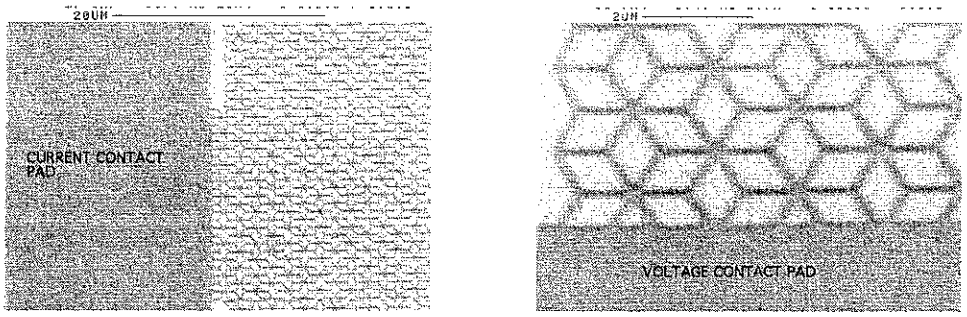


Figure 5.7: SEM image of the current and voltage of the contact pads for Star 20.

The normal state resistance $R_n$ of the arrays at 1.25 K are, 4.21 $\Omega$ and 63.56 $\Omega$ for Star 600 and Star 20, respectively. The arrays transition temperature in zero field are 1.236 K for Star 600 and 1.240 K for Star 20, respectively, obtained from the resistive transition for a resistive criterion of 0.5 $R_n$.

The transition width for both arrays is 3 mK ($10\% - 90\%$ of $R_n$), that is 0.2% of the zero field transition temperature, and comparable to the width in the homogeneous film. No double transitions where found, indicating that both arrays are very homogeneous.

## Temperature regime for negligible screening effects

In all the data analysis we are neglecting screening effects of the external applied field $\mu_o H$, which is supposed to be uniform and equal to the induction field $B$ over the entire network. This assumption is valid as long as the array dimensions are much smaller than the array effective screening length in transverse field $\lambda_\perp^{eff}$, which has the GL form [46],

$$\lambda_\perp^{eff} = \frac{a}{w}\frac{\lambda^2(0)}{d}\frac{1}{1-T/T_c(B)} \tag{5.18}$$

where the penetration depth is given by $\lambda = 0.64\lambda_o\sqrt{\xi_o/l_{el}}$ in the dirty limit, and the electronic mean free path $l_{el}$ is obtained from the zero temperature coherence length $\xi(0) = 0.852\sqrt{\xi_o l_{el}}$. Using $\xi(0) = 157$ nm, a wire cross section $wd = 0.01$ $\mu$m$^2$ and the values for pure Al, $\xi_o \approx 1600$ nm and $\lambda_o \approx 50$ nm, we obtain $\lambda_\perp^{eff}(0) = 7.72$ $\mu$m.

Taking the shortest side length of the arrays, the temperature regime for neglecting self-screening effects is then $T > 0.614\ T_c(B)$ for Star 20 and $T > 0.987\ T_c(B)$ for Star 600. The array Star 600 is only used in transition line measurements, where

this requirement is largely fulfilled. The smaller size of Star 20 allows us a wider temperature range for the critical current measurements.

### 5.4.2 Superconducting to normal transition

We performed measurements of the arrays transition temperature as a function of applied field $T_c(\mathrm{H})$, which are to be compared with the lowest energy solution of the network linear GL equations. As seen previously, the transition line depends on the applied field only on the reduced flux per elementary cell, $f = BS_{cell}/\Phi_o$, and can be mapped into the ground state eigenvalue $\epsilon_g(f)$ of the $T_3$ tight-binding spectrum [19] by,

$$\frac{T_c(f)}{T_c(0)} = 1 - \frac{\xi^2(0)}{a^2}\arccos^2\left(\frac{\epsilon_g(f)}{\sqrt{18}}\right) - \xi^2(0)\frac{\pi^2}{3}\frac{w^2}{\Phi_o^2}B^2, \tag{5.19}$$

where $\xi(0)$ is the superconducting coherence length at zero temperature, $f$ the frustration, $\sqrt{18}$ the effective coordination, and the last term represents a parabolic contribution due to the field penetration in the finite wire thickness.

In order to attain a fine field tuning, the transition temperature was monitored by locking the temperature controller to keep the sample resistance at a constant value as the magnetic field is varied. The transition line of Star 20 for a resistance criterion of 0.5 $R_n$ is displayed in Fig. 5.8(top) as a function of applied field. As we can see, the transition line presents an oscillatory field dependence with local maxima occurring with a magnetic period of 2.39 mT which correspond to one flux quantum per unit tile. These oscillations are superposed in a parabolic background which describes the critical field of the wires and which is represented by a dash line in Fig. 5.8(top). The coherence length at zero temperature $\xi(0)$ can be estimated from this contribution, leading to $\xi(0) = 135$ nm for star 20. From a similar fit we obtain $\xi(0) = 137$ nm for Star 600.

The transition line on regular networks is periodic on $f = \pm 1$ [47] thus we shall restrict our discussion to the range $0 \leq f < 1$. Several resistance criteria were used in the determination of the transition line. A rich field structure of the transition line at rational frustration was observed independently of the chosen resistance criteria, between 0.06 and 0.87 $R_n$, though the field structure at lower temperatures becomes more pronounced in the curve taken at low criteria, as well as the dip at half-flux is

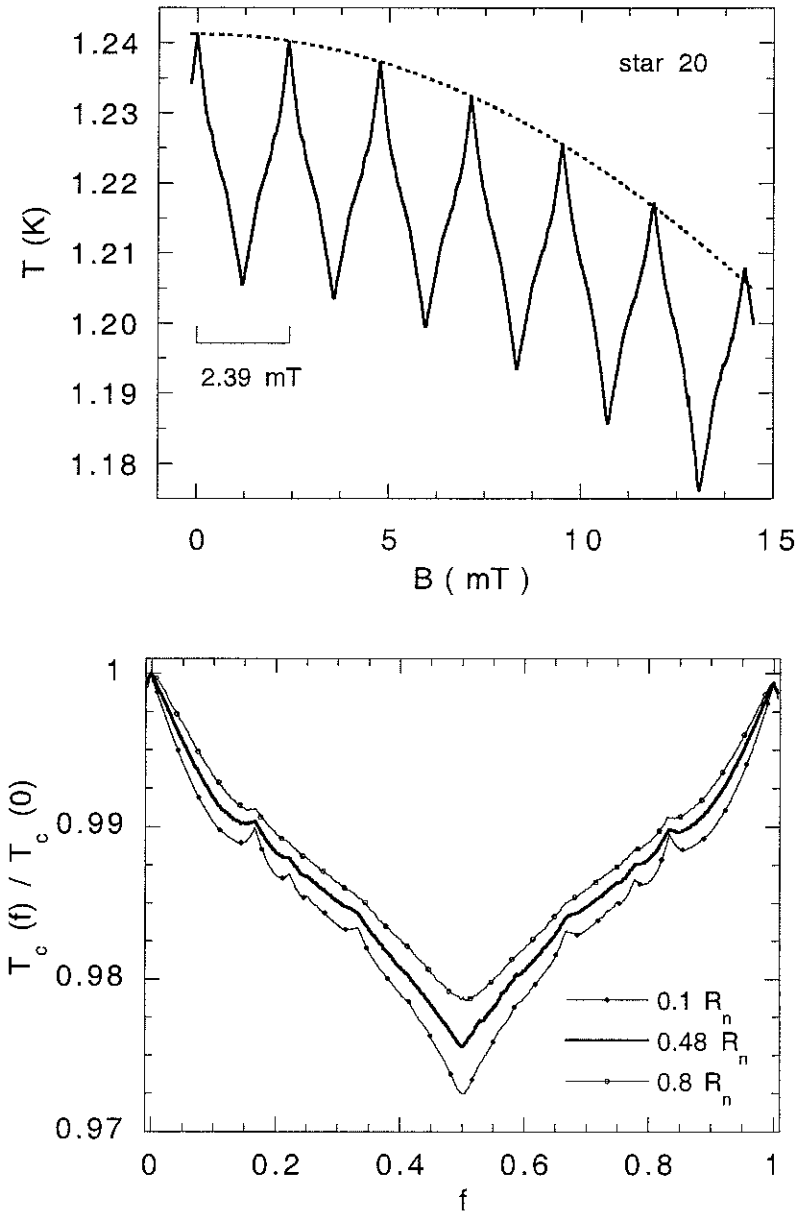


Figure 5.8: Top graph: Transition line of Star 20 as a function of applied field (solid line). The transition temperature presents local maxima with a field periodicity of 2.39 mT and follow a parabolic field dependence (dash line). Bottom graph: Reduced critical temperature $T_c(f)/T_c(0)$ of Star 600 measured at different resistance criteria, 0.1, 0.48 and 0.8 of $R_n$.

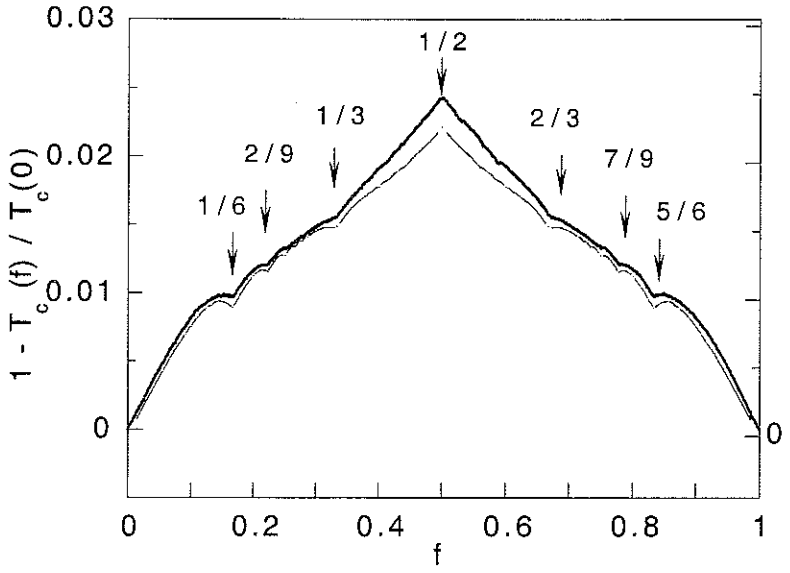


Figure 5.9: Reduced critical temperature as a function of frustration for Star 600 (heavy line, left axis). The theoretical curve has been offset by -0.0005 for clarity (small dots, right axis).

more prominent. In Fig. 5.8 are displayed the transition temperatures of Star 600 taken at different criteria 0.1, 0.48, and 0.8 of $R_n$, respectively.

We shall assume the half resistance criterion corresponds to the mean-field transition, since the temperatures measured at the low criteria are affected by the broadening of the transition in applied field, as well as at higher resistance criteria the fluctuations of the order parameter amplitude may become important. In Figure 5.9 is displayed the transition line of array Star 600 in reduced units $1 - T_c(f)/T_c(0)$ as a function of frustration after subtraction of the parabolic background. It is also displayed the theoretical $T_c(f)$ obtained from equation 5.19 (without the parabolic term) using the ground state eigenvalues of the $T_3$ spectrum. The only adjustable parameter is the coherence length, the best fit being obtained for $\xi(0) = 157$ nm.

The fine field structure of the experimental data is very well described by the theoretical curve. Distinct downward cusps are visible at low order rationals $f = 1/q$, for $q = 3, 4, 6$, and $f = 2/9$. They reflect the long range phase ordering of the order parameter among network sites, established at fields commensurate to the underlying lattice. These are well known features of the field behaviour of periodic superconducting networks and were discussed previously [44, 48].

The novel feature of the transition line occurs at $f = 1/2$, where the maximum of $T_c(f)$ depression (30 mK) is achieved. It differs from the field behaviour observed at rational frustration in two senses: it is the maximum depression of the transition temperature induced by the magnetic field and is associated with an inversion of the field modulation concavity. Moreover it persists distinctly at all criteria used on $T_c(f)$ determination, from 0.06 $R_n$ to 0.87 $R_n$, though the downward cusps at other rationals fade out with increasing temperature, as observed in Figure 5.8.

This maximum depression at half-flux is a consequence of the destructive interferences occurring at individual cells at this flux. Therefore, the field dependence of the transition line close to half-flux should be similar to the $T_c$ variation in a single loop geometry, characteristic of quantum effects determined on a finite length scale. We compared the field dependence of both curves near half-flux and observed that they are indeed similar close to half-flux. In Figure 5.10 is displayed the transition line of Star 600 and the transition line of a Little-Parks loop using with the same $T_c(0) = 1.234$ K and the coherence length $\xi(0) = 157$ nm. The dice transition is also displayed. Both curves have been offset for clarity. The similarity of the field dependence using the same array parameters for the single-loop as those used in the fitting of the array ground state energy, confirms that due to the AB cage effect, only finite closed paths are available for the phase circulation, such as in simple finite geometries.

### 5.4.3 Broadening of the transition width in applied field

Associated to the inversion of the $T_c(f)$ cusps we also observed an anomalous broadening of the resistive transition $\Delta T_{width}$, at half-flux. The resistance of Star 20 as a function of increasing temperature is displayed in Fig. 5.11(top) for different frustrations: 0, 1/6, 1/3, 1, and 1/2. The transition width (10%-90% of $R_n$) at $f = 0$ and 1 are the same (3 mK) and increase slightly to about 6 mK for f=1/3 and 1/6. At half-flux it attains the maximum broadening of 12 mK.

The anomalous broadening at half-flux is best identified on the transition width as a function of a fine field tuning, as displayed in Fig. 5.11(bottom) for Star 600. $\Delta T_{width}$ is obtained as the difference between the $T_c(f)$ curves taken by the sweeping

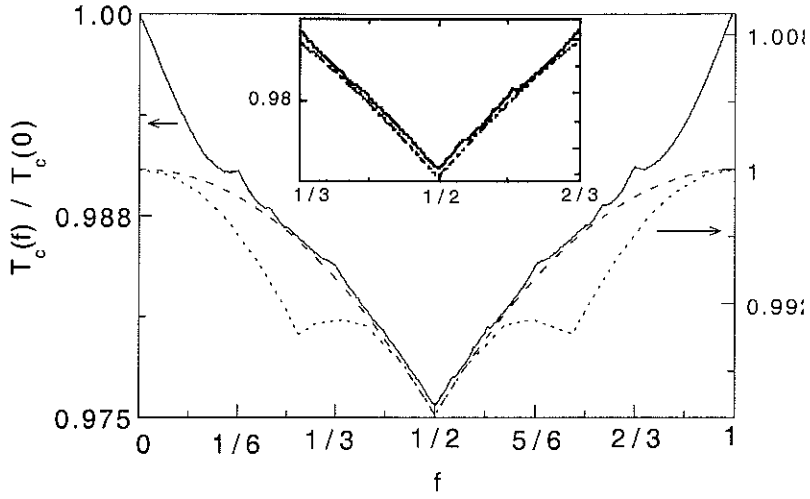


Figure 5.10: Comparison between the transition line of Star 600 (thick line), the Little-Parks loop (short dashes line) and the dice geometry (dashes line) in reduced units $T_c(f)/T_c(0)$ as a function of frustration. The Little-Parks curves were offset. Inset: Zoom of the graph in the field range $1/3 < f < 2/3$.

field method for criteria $0.6R_n$ and $0.1R_n$, respectively. We can see that at half-flux, the transition width as an abnormal broadening, reaching 12 mK which is twice the average width over most of the field range. At the strong commensurate fields $f = 0$, 1/6, 1/3, and 2/9, $\Delta T_{width}$ is sharply reduced to a few mK as expected for a phase ordered system. Close to these fields, the circulating phase of the order parameter over the network tiles is able to "lock" in the nearest commensurate state with the creation of few mobile defects, broadening slightly the transition. Close to half-flux no commensurate state is available, thus phase correlations between network sites cannot be established, leading to a strong broadening of the transition.

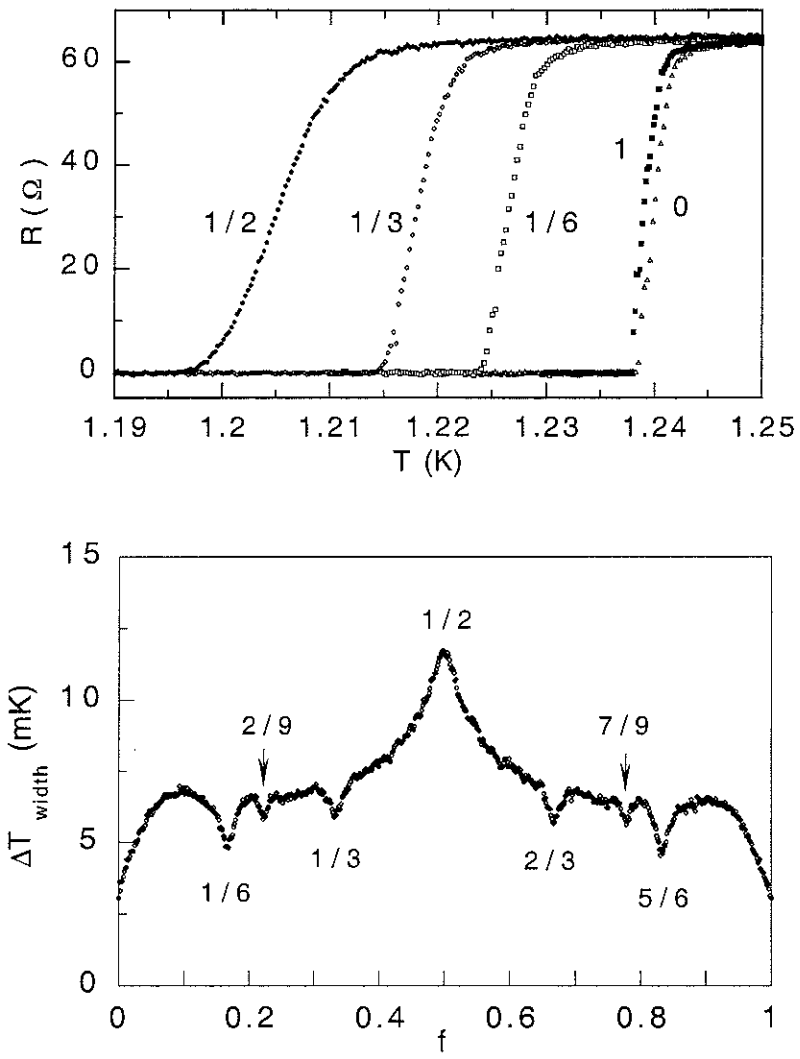


Figure 5.11: Top: Resistive transition of Star 20 at several frustrations. An anomalous broadening is observed at half-flux. Bottom: Transition width *vs* frustration for Star 600. The large broadening at $f = 1/2$ indicates the presence of strong phase fluctuations.

## 5.5 Critical Current

In the context of a superconducting wave function, a non-dispersive state cannot carry phase information through the network, contrary to a Bloch state. Therefore, we performed critical current measurements in order to test the ability of the superconducting circuit to sustain a supercurrent, *i.e.*, both a finite order parameter and a finite superfluid velocity, under the action of an external transverse field. In fact, due to the isomorphism between the tight binding problem and the linearized GL, the superfluid can be expressed in terms of the group velocity calculated from the knowledge of the band spectrum close to the ground state. Close to $T_c$, we expect the critical current to follow a 3/2 power law that generalizes the depairing current of a one-dimensional superconducting wire [34] to a superconducting network[49]:

$$J_c(T,f) = J_n C(f) \left( \frac{T_c(f) - T}{T_c(0)} \right)^{3/2}, \tag{5.20}$$

where $J_n$ is the zero field depairing current density at T = 0 K. The field dependent coefficient $C(f)$ is derived by,

$$C^2(f) = -\frac{1}{a^2\sqrt{18-\epsilon_g^2}} \frac{\partial^2 \epsilon_g}{\partial k^2} \arccos \frac{\epsilon_g}{\sqrt{18}} \tag{5.21}$$

where $\partial^2\epsilon_g/\partial k^2$ is the band curvature calculated from the knowledge of the band structure close to the ground state $\epsilon_g(f)$. The coefficient $C(f)$ is obtained from the group velocity [1] and expresses the effect of the applied field in the band structure itself, or in this case, the superfluid velocity. In the case of non-dispersive state such as for the $T_3$ spectrum at half-flux, $\partial^2\epsilon_g/\partial k^2$ is strictly zero.

We performed critical current measurements as a function of applied field and temperature. They are obtained from the dynamic resistance characteristics $dV/dI$ *vs* increasing dc bias current at temperatures close to $T_c(0)$. A resistance bridge at 33 Hz and an ac measuring current of 20 nA is used. In order to avoid heating effects due to feeding a large current, we used sample Star 20 with 23 cells (20 $\mu$m) width, smaller than Star 600. The critical current density per wire $J_c(T,f)$ is obtained from the network critical current divided by the number of parallel wires (25) and the wire cross section.

Measurements were done automatically using a routine described in Chap. 3: for ex. at a fixed field, the temperature is decreased from above $T_c$ by small increments, and after a waiting time of 60 seconds, the dynamic resistance is measured as a function of bias dc current, which is varied by small increments. When the measured resistance equals or exceeds the chosen criterion, the incremental current sequence is stopped, the bias current is decreased by one step and the resistance re-measured as a function of smaller increments of current until the criterion is fulfilled. The critical current measurements were always done in increasing current to avoid thermal hysteresis effects. Since the array resistance may overshot well below the true critical current is reached, due to a large increment step, increments steps were chosen in order to avoid this problem. We observed that the overshot effect was minimized for increments smaller than $2.5\times10^{-4}$ of the critical current at the respective temperature (or field).

The criteria used for the critical current was the threshold current for which the dynamic resistance exceeds 1 $\Omega$ (0.2% $R_n$). Within the sensitivity limits of our measurements, it corresponds to the maximum current that the circuit is able to carry without dissipation.

### 5.5.1 Temperature dependence at fixed field

We performed measurements of the critical current as a function of temperature at several strong commensurate fields and at half-flux. These measurement allowed us to confirm that the power law dependence predicted by Eq. 5.20 for the depairing current is indeed observed in the temperature range $T_c(f) - T < 40$ mK.

The data obtained for the resistance criteria 0.16% $R_n$ is presented in Fig. 5.12.a) on a 2/3 power as a function of the reduced temperature $(T_c(f) - T)/T_c(0)$ for frustrations 0, 1, 1/6, 1/2 and a non-commensurate state, $1/3-\delta$, with $\delta = 0.016$. The fit of the zero field data gives a $J_c(T = 0) = 7 \times 10^6$ A/cm$^2$ which compares well to the theoretical value for the depairing current of a 1D wire in zero field, $J_c(T = 0) = 7.6 \times 10^6$ A/cm$^2$. The results obtained at frustrations $f = 0$ and 1 are comparable and a similar symmetry was also observed at other frustrations, such as 1/6, 5/6 and 1/3, 2/3. At half-flux we obtained the lowest values of critical current.

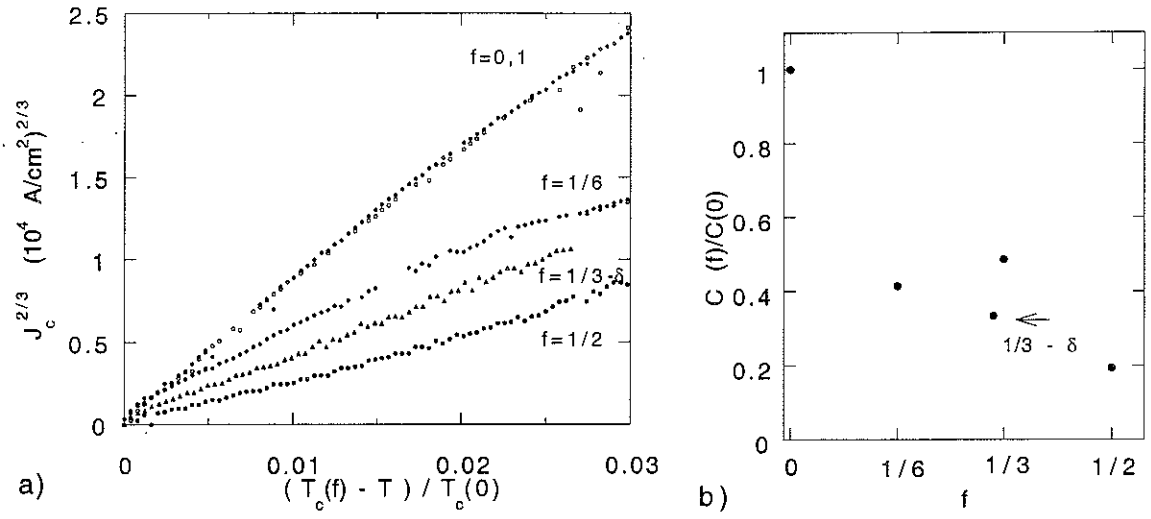


Figure 5.12: a) Critical current density powered to 2/3 as a function of the reduced temperature $(T_c(f) - T)/Tc(0)$ for several frustrations. b) The coefficients C(f) obtained from the slope of the $J_c^{2/3}$ data and normalized by the zero field value.

The coefficients $C(f)$ obtained from the slopes of the $J_c^{2/3}$ data are displayed in Fig. 5.12.b) after normalization by $C(f = 0)$. At half-flux, $C(f)$ is reduced to 19% of its zero field value, indicating that the lower critical current at half-flux is not only due to a reduction of the transition temperature but also directly related to the applied field.

These results show that the 3/2 power law which generalizes to a network the depairing critical current of a 1D wire is a good approximation, at least within the studied temperature range. The comparison of the field coefficients $C(f)$ at several frustrations indicate that the lowest critical current values attained at half-flux are also related with the effect of the applied field in the superfluid velocity and are not only a consequence of the strong depression of $T_c(f)$ at this flux.

### 5.5.2 Field dependence at fixed temperature

Critical current measurements as a function of magnetic field were performed at several temperatures below the transition temperature at half-flux, T=1.2 K. The field is varied by increments of frustration of $3.5 \times 10^{-3}$. At a given field, the current

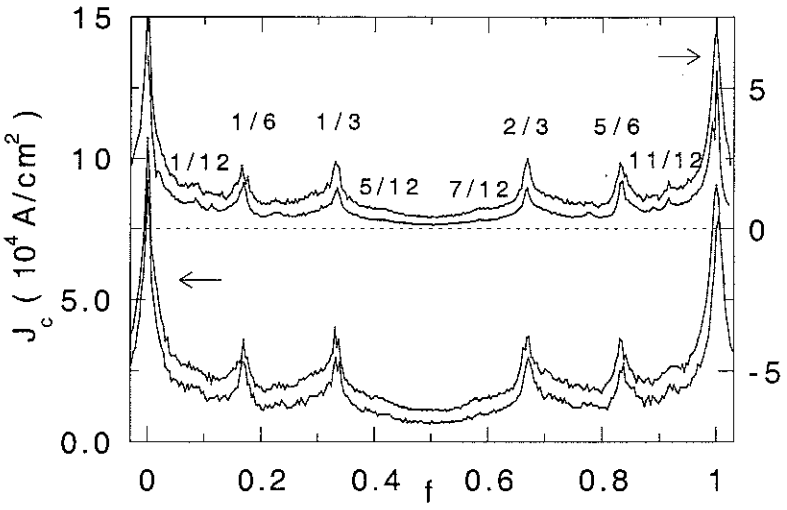


Figure 5.13: Critical current density of Star 20 as a function of $f$ at several temperatures. From top to bottom 1.172 K, 1.185 K, and 1.155 K, 1.165 K. The upper two curves have been offset (see right axis).

is increased by small increments (typically smaller than 2 $\mu$A). When the criterion is reached, the fed current is decreased of one step and re-increased in smaller steps ($\approx$ 0.1 $\mu$m) until the resistance criterion is again fulfilled. The current value is recorded, the dc current set to zero, and the field increased by one step and the process restarted. Each resistance measurement is done after a delay of 1 second and after the field change we give a waiting time of 3 seconds.

In the field and temperature ranges we studied we didn't observe any hysteresis effects. We restricted these measurements to temperatures above 1.14 K, since at lower temperatures the bias of high currents may lead to heating or non-negligible field screening effects. The critical current obtained at temperatures 1.185 K, 1.172 K, 1.165 K, and 1.155 K are displayed in Fig. 5.13. Besides the fundamental peaks at frustrations 0 and 1, prominent peaks are clearly identified at frustrations 1/6 and 1/3, in sharp contrast to the total absence of peak at half-flux. Moreover, the critical current at this field was always found to exhibit the lowest values for all studied temperatures.

The field structure of the data presented in Fig.5.13 is not as rich as for the transition line due to noise in our measurements, which covers the fainter peaks. The field structure can be improved by averaging $J_c(f)$ readings of independent field runs at

the same temperature. Attention is paid to the effective zero field of which $J_c(f)$ sequence. In Figure 5.14(top) is plotted the average over 20 independent measurements taken at $T = 0.96\ T_c(0)$ (1.185 K). We can now distinguish sharp peaks for the same frustrations as the downward cusps observed in the transition line. The peaks width reveal the sensitivity of the network to commensurability, being reduce to about half their height at the commensurate states for a frustration change of $7 \times 10^{-3}$. The remarkable finding is the absence of peak in the critical current at the lowest order rational $f = 1/2$, at which it exhibits a clear minimum. This behaviour is in sharp contrast to those of other regular periodic lattices. The most familiar example is the square lattice where a checkerboard commensurate state at half-flux leads to an important peak in the critical current [49].

In the inset of Fig. 5.14(top) is displayed the theoretical $J_c$ obtained using Eqs. (5.20), (5.21) and the theoretical $\partial^2\epsilon_g/\partial k^2$ calculated by P. Butaud from the knowledge of the band structure close to the ground state ($k = 0$), and for $f = p/q$, $q < 50$. We used $T = 0.96\ T_c(0)$ and $J_n = 7 \times 10^6$ A cm$^{-2}$, estimated from a 3/2 power law fit of the zero field $J_c(T, 0)$ data. The critical current consists of successive $\delta$-functions at rational frustration $f = p/q$ except at 1/2, for which it is strictly zero. The critical data in the inset of Fig. 5.14(top) was calculated for a small set of rationals, the reason why no data close to, for example, zero field is presented. At all rational frustrations, but 1/2, the spectrum is band-like and the group velocity is finite (Bloch states). However, half-flux the group velocity is strictly zero due to the absence of band and the critical current vanishes. The experimental data follow the same qualitative behaviour *vs* field as the theoretical predictions. A good qualitative agreement between the experimental data and the theoretical $J_c$ is obtained at the strong commensurate states $f = 0, \frac{1}{6}, \frac{1}{3}$ and symmetric frustrations. At half-flux, though non-zero, the critical current attains the lowest value in applied field.

If we discount the temperature dependence of the critical current data using the 3/2 power law of Eq. 5.20, we can observe that at half-flux the field dependent coefficient $C(f)$ is flat, and no peak is observed in contrast to the other low order rational frustrations. In Figure 5.14 we display the coefficient $C(f)$ obtained from the $J_c(f)$ data at 1.185 K and using the transition temperatures measured for the same resistive

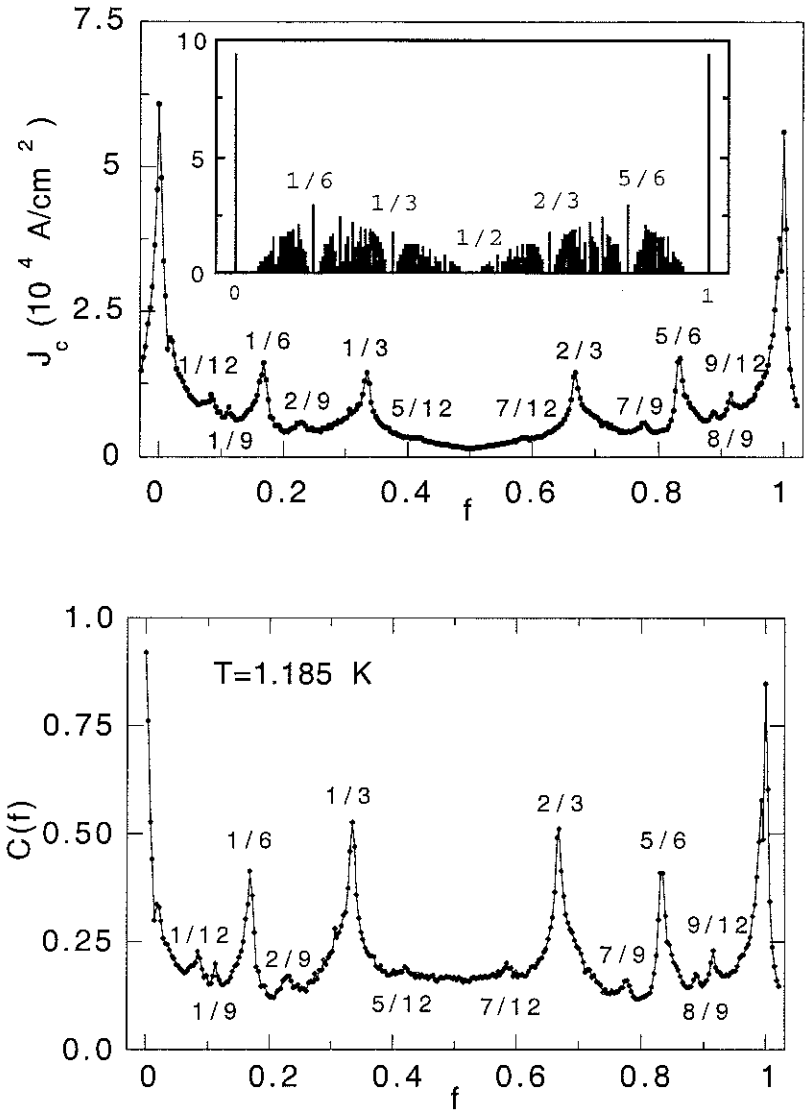


Figure 5.14: Top: Critical current density of Star 20 *vs* $f$ at T=1.185 K. Peaks indicate phase coherent states. Inset: Theoretical values calculated for the same temperature. Bottom: The coefficient $C(f)$ obtained from the experimental data.

criterion as the critical current data.

The absence of structure in $C(f)$, thus of $J_c$, at $f = 1/2$ reflects the effect of the band structure on the superfluid velocity, and provides a strong evidence of the non-dispersive character of the state at $f = 1/2$, although the measured critical current does not vanish. This situation is original for an infinite tiling and is due to the special $T_3$ geometry. A similar effect is found when $f$ approaches irrational frustration (for example, at small frustration $f = 1/q$, with large $q$): the bandwidth then becomes exponentially small and therefore the group velocity and the critical current are suppressed.

The comparison of the experimental $J_c$ data with the theoretical values can only be done on a qualitative basis. On one hand the incomplete suppression of $J_c$ at half-flux can be due to the finite size of the network. A current carrying state (an edge state similar to surface superconductivity in finite type-II superconductors) exists along each edge of the finite network and is expected to lead to a non-zero supercurrent. On the other hand, the comparison is made on the basis of a linearized GL approach. In the presence of important bias currents this may be no longer valid and the non-linear GL term which was neglected in Eq. (5.20) may become important. Presumably, the non-linear terms in the GL formulation are responsible for degrading the fine features of the band structure and therefore lead to a finite theoretical critical current. To go further, an exact solution of the non-linear GL equations would be needed. The critical current observed in Fig. 5.14(top) at small frustrations, for example close to 0, may have the same origin. Nevertheless, as was demonstrated by Abrikosov[50], a good physical insight of the superconducting properties can be obtained from the eigenstates of the linearized GL equation.

In what concerns the qualitative discussion of the $J_c$ field dependence , we believe it is not dependent on the chosen criteria. In Fig. 5.15 is presented the critical current measured at T= 1.195 K for a resistance criteria 0.02 $R_n$. We can see that the sharpness of the strong commensurate states is reduced, however the relative height of the peaks as well as its absence at half-flux is still similar to what was found for the lower criteria.

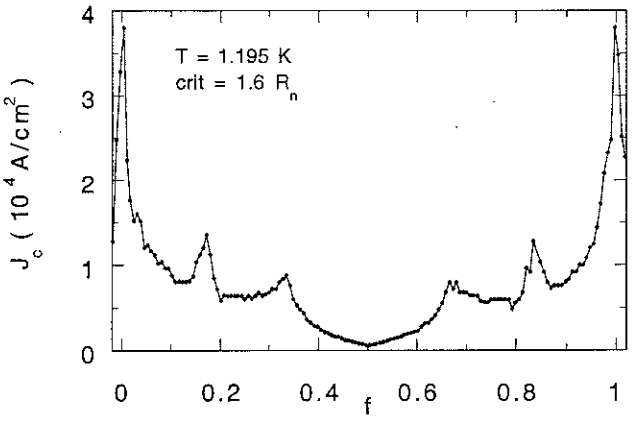


Figure 5.15: Critical current density of Star 20 as a function of $f$ at 1.195 K for the criteria 1.6 $R_n$.

### 5.5.3 Dissipation effects in the dV/dI characteristics

The previous data was obtained for the criterion which corresponds to the onset of dissipation in the network (within our resolution limits). In this section we discuss briefly some features of the $dV/dI$ characteristics as a function of applied current, which are related with dissipation processes. In the linearized GL approach we are neglecting fluctuations of the order parameter amplitude, which remains constant in time. In the absence of fluctuations, dissipation sets in when the bias dc current reaches the depairing critical current. If fluctuations are non-negligible, dissipation sets in before the depairing limit is reached and the sample behaves as a non-linear resistor. The appearance of resistance in a 1D superconducting wire was originally studied by Langer and Ambegoakar. In this case, dissipation sets in due to current induced phase slips. Essentially, a phase slip occurs when the order parameter amplitude at some point in the wire goes to zero, decoupling the two extremes, and the relative phase is then allowed to change by $2\pi$.

We have seen previously that the resistive transition width as an anomalous broadening at half-flux, indicating that the phase configuration is very disordered at this field. We observed a similar broadening on the $dV/dI$ characteristics as a function of bias current at half-flux, in contrast to other commensurate fields.

The characteristics in zero field didn't present dissipation tails at temperatures below 0.998 $T_c(0)$, the transition to the resistive state occurring with a jump when

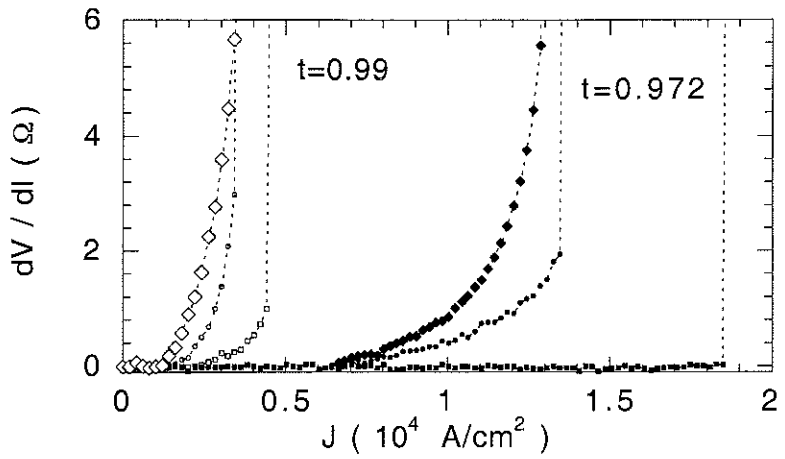


Figure 5.16: Dynamic resistance as a function of bias dc current density for frustrations 1/2 (◇), 1/3 (□) and 1/3−$\delta$ (○) taken at the same reduced temperature $T/T_c(f) = 0.99$ (open symbols) and 0.972 (solid symbols).

the critical current value was reached. Therefore the critical current data in zero field is independent on the criterion.

At non-zero field the criterion for the critical current is a delicate choice, since a dissipation tail is identified before the resistive jump to the normal state, at temperatures close to $T_c(f)$. We compared the characteristics $dV/dI$ *vs* $I$ at a strong commensurate state $f = 1/3$, at half-flux and at the non-commensurate state $1/3-\delta$, with $\delta = 0.016$. The characteristics obtained at the same reduced temperatures $T/T_c(f) = 0.972$ and 0.99, respectively, are displayed in Fig. 5.16

We can see that at $T/T_c(f) = 0.99$ all characteristics present a dissipation tail at low currents, followed by a jump at some current value, except at half-flux. At f=1/3 and $T/T_c(f) = 0.99$, the tail follows an exponential dependence in current which we relate to thermal activation of current induced phase-slips in the network wires. This dissipation mechanism, previously developed to explain the dissipation onset in 1D wires [34], was also identified in JJ arrays and strong coupled wire networks [1],[46] . The exponential fit of the characteristic at $T/T_c(f) = 0.99$ leads to a $I_o = 12.07$ nA/K per wire, which compares well with the theoretical value for phase slip in a 1D wire, $I_o = 13$ nA/K [34]. We believe this good agreement comes from the fact that at a strong commensurate field, the phases are well aligned and therefore we are sensible

to phase slips in the wires. This fitting value increases to 32 nA/K at 1.204 K and at temperatures below 1.2 K the resistive tail becomes quasi-linear and almost negligible. Below this temperature, the onset of dissipation coincides with the jump into the resistive state, and the critical current is independent on the criterion choice.

In contrast, the dissipation tails remains at $1/2$ and $1/3 - \delta$. The absence of tail at $1/3$ below $T/T_c(f) = 0.972$ in contrast to the close field $1/3 - \delta$, indicates that at $f = 1/3 - \delta$ the tail is related to disorder (of density $\delta$) in the vortex sublattice (or phases configurations) which are easily mobile under the influence of a current or thermal agitation. The similarity of the half-flux curves seem to indicate that the phases configurations are also very disordered. At these frustrations we could not fit the current dependence of the dissipation tail to the exponential law.

A comparison of several characteristics at $f = 1/3 - \delta$ and half-flux are displayed in Fig. 5.17. The curves taken at the same reduced temperature are presented using the same symbols, open symbols for $f = 1/3 - \delta$ and solid symbols for $f = 1/2$. The resistive tail at half-flux is distinctly present until resistances of the order of 10 $\Omega$ ($0.16R_n$). We tried to find the law which best describes the dissipation at half-flux. The exponential law $e^{I/I_o}$ for phase slip activation lead to estimations of $I_o$ much higher than the theoretical values for a 1D wire, such as 40 times in the best cases. We found a reasonable agreement using a power law $dV/dI \approx I^{a_{1/2}-1}$. The corresponding fits are shown in Fig. 5.17 by dash lines and the fitting exponent $a_{1/2}(T)$ in Fig. 5.17 as a function of reduced temperature $t = T/T_c(f)$. The exponent $a_{1/2}$ is about 3 close $t = 0.995$ and increases with decreasing temperatures. The results are very similar to those obtained at $f = 1/3 - \delta$. This power law dependence often used to describe dissipation due to current induced binding of vortex-vortex pairs, in our case it suggests that the dissipation is due to current induced dissociation of the supercurrent loops (vortices) over the network. However, this simplified discussion does not allow to conclude on this subject.

Given the presence of the dissipation tail at half-flux for all studied temperatures, we have chosen the onset of dissipation as the criterion for the critical current. We will see that in fact this criterion allows to discern between the phase ordering of the vortex lattice at different fields. In Figure 5.18 is displayed a comparison between the

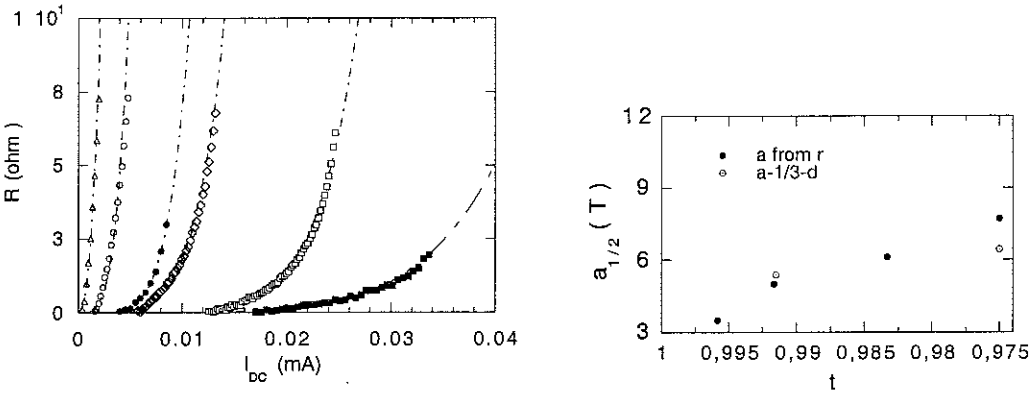


Figure 5.17: Left: dynamic resistance as a function of dc current at frustration 1/2 (open symbols) and $1/3-\delta$ (solid symbols). Right: exponent obtained from a power law fit of the dynamic resistance data as a function of current at half-flux (solid symbols) and $1/3-\delta$ (open symbols).

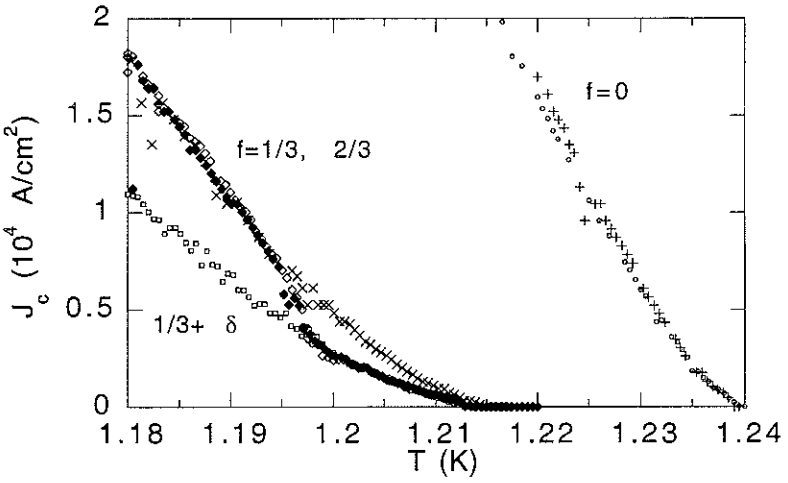


Figure 5.18: Comparison between the critical current data taken at frustrations 0, 1/3, 2/3, for different resistive criteria, 0.0016 $R_n$ and 0.016 $R_n$ (crosses). At zero frustration the data is independent of the criterion. The same at strong commensurate frustrations 1/3 and 2/3, below T=1.198 K. Above this temperature the criterion choice is no longer equivalent due to the onset of dissipation processes.

data obtained for criteria 0.0016 $R_n$ and 0.016 $R_n$ in zero field, and for frustrations 1/3 and 2/3. The data obtained at frustration $1/3 - \delta$ at $0.0016R_n$ is also presented. In zero field the data is independent of the chosen criterion at all temperatures, as well as the data at 1/3, 2/3 below 1.2 K. Above this temperature similar results are obtained at 1/3 and $1/3 - \delta$ indicating that in this regime the low criterion is sensible to dissipation due to thermal activation, which destroys the phase ordering in the 1/3 state. No anomaly is observed in the whole temperature regime for the high criterion data.

Another two important aspects of this figure are: (i) the anomaly in the temperature dependence for frustrations 1/3 at T=1.2 K, which occur at the same temperature at which the system becomes superconductor at half-flux; (ii) the absence of anomaly in the data obtained at $1/3 - \delta$ or at half-flux. These features might be related with the temperature dependent coherence length which, at T=1.2 K and below becomes comparable to the network lattice constant $a$. Above this temperature, the vortices or fluxoids are coreless and extend over a radius $\xi(T)$ which can be several tiles length. At lower temperatures, when $\xi(T)$ becomes smaller than $a$ the coreless fluxoid can be confined within a single tile. At half-flux this would lead to the possibility of forming closed superconducting loops (leading to a *single-loop* type transition) and the transition to the superconducting state. At ordered vortex states, it would mean that thermal activation of phase slips will be more difficult, since, due to phase coherence over several tiles length, the creation of a few vortex defects is not favorable, and implies an activation energy to move the entire vortex sublattice (which scales with the domain size). In such a case, the dissipation will set in only when the transport current reaches the critical value in every wire, and the whole vortex sublattice becomes unstable. For a disordered vortex state, there are no ordered domains, which may explains the absence of anomaly in the curve at $1/3 - \delta$ and half-flux. These results thus indicate that below 1.2 K, the low resistance criterion allow us to discern between an ordered and a disordered vortex state. In fact, this temperature regime is the same used in the critical current measurements as a function of sweeping field, therefore the previous discussion remains unchanged.

## 5.6 Imagery of the vortex configurations at half-flux

We performed several Bitter decorations on superconducting (Sc) wire networks to observe the vortex arrangements at half-flux and other frustrations. The decoration experiments are performed at 4.2 K, therefore we used niobium wire networks for which the transition temperatures are around 9 K.

From these experiments we tried to obtain information about the phase coherence and degeneracy of the vortex sublattice in the $T_3$ network at half-flux.

For a Sc wire network, the ground state vortex configuration at rational frustration can be seen as the distribution of loop supercurrents which minimize the system free energy while maintaining fluxoid quantization around the cells and satisfying current conservation at every node. The system will be phase coherent if the same choice of ground state is done over the entire network. Phase coherence is related with the ground state degeneracy since, if a free energy minimum exists, the network will be sensible to phase twists at its boundaries and the whole system will readjust to occupy the correspondent ground state configuration. Ordered vortex structures are then formed over the entire network, or at least over phase coherent domains of several cells size.

If the ground state is highly degenerate, such as for the $T_3$ network at half-flux, the vortex sublattice is not able to chose one ordered configuration and a very disordered structure is to be expected.

### 5.6.1 The problem of the ground state configurations

For a discrete 2D superconducting system such as a wire network, the vorticity of a lattice cell is generally defined as the sum of the phase differences around the cell edges. When exposed to a magnetic field, the circulation of the vector potential around a cell, as well as the loop supercurrents which arise in response to the applied field, induce a phase difference between the cell nodes. In this case, we assign a vortex to a cell if there is a closed supercurrent loop counterclockwise and no vortex otherwise.

The calculation of the ground state configurations is a very delicate problem. In the case of Sc wire networks, close to the S-N transition, the applied field induces not only frustration on the phase of the order parameter at the network nodes but also a reduction of the order parameter amplitude in the wires where loop supercurrents flow. Both variables must be then taken into account to find the minimum free energy. Some ground state configurations for the square network at low order frustrations $f = p/q$ with $q = 2, 3$ and 5 were calculated using the wire network nodes equations by Wang *et al.* [51]. A simpler approach employed by Chi *et al.*[52] consisted in finding the distribution of loop supercurrents which led to the minimum free energy. This approach assumes a constant amplitude of the order parameter over the network and therefore is valid at temperatures well below $T_c$. Both approaches lead to similar ground state configurations, including the well known checkerboard vortex configuration at half-flux. The ground state patterns at rationals 1/2, 1/3, 2/5 were previously observed by decoration experiments on superconducting wire networks [9], scanning Hall microscopy [53, 54] and scanning SQUID microscopy [55].

On Josephson junction (JJ) arrays the problem is somewhat simplified. These systems can be described as an array of superconducting islands weakly connected to its neighbours. Under a transverse magnetic field the only variables to the problem are the distribution of the order parameter phase at each island and the array can be described by the uniformly frustrated 2D XY model [13]. The first vortex configurations were calculated by numerical methods by Teitel and Jayaprash [56] for JJ square arrays at low order frustrations $f = p/q$, with $p, q$ prime, and assuming the vortex arrangements to be periodic on a unit cell $q \times q$ tiles. However, one limitation of the numerical methods is that it is difficult to determine if a given configuration corresponds to a local or a global minimum energy. Moreover, simulations are performed on *finite* size networks and using periodic boundary conditions, that is, the periodicity on a $q \times q$ unit cell is imposed, which may not be valid at high order rationals. Namely, the unit cell for the vortex pattern might be $mq \times nq$ with $m, n \geq 2$ [57].

Another related problem is the degeneracy of the ground state configurations. An ordered vortex lattice always displays a discrete degeneracy associated with the symmetry of the underlying lattice itself, for example the checkerboard configuration

displays the 4-fold degeneracy of the square lattice. However, the ground states may have a degeneracy not related with symmetries. This point has been addressed 2D frustrated XY model in a triangular [58, 59, 60] and a honeycomb lattices[61] at certain frustrations. A particularly interesting case is the triangular lattice at rational frustrations close to 1/2 and at 1/4 [12, 60]. At rationals close to half-flux it was shown that a set of commensurate states can be constructed from the f=1/2 state by introducing different sorts of defects [12]. The defects considered were 1D linear defects formed by parallel domain walls separating domains of frustration 1/2 with the same chirality (designated stripped phase), 2D periodic networks of intersecting domain walls separating domains of opposite chirality or the formation of a superlattice of point like defects (vacancies). Such commensurate states were found to be consistent with the rationality $p/q$ of the peaks found experimentally on the superfluid response of a JJ triangular array under a magnetic field [12]. On the other hand, the state at frustration $f = 1/4$ is highly degenerate and a set of degenerate commensurate states can be obtained from each other by introducing zero energy domain walls [60, 59].

The frustrated 2D XY model at irrational frustration was initially addressed by Halsey for the square JJ array [62, 63] at $f = 1-\Omega = (3-\sqrt{5})/2$, where $\Omega = 0.6108\ldots$ is the golden mean. At this frustration he predicted a glass transition at finite temperature of the vortex lattice into a frozen disordered glass [62]. The vortex distribution is then very disordered, displaying quasi-one dimensional ordering on small length scales. This ordering comes from the formation of quasi-one dimensional staircase structures, separated by domain walls, for which the supercurrents are automatically conserved at each node. Later work by Teitel *et al* [64] indicate that the nature of the transition is modified by introducing next-nearest neighbour interactions. In this case they predicted a first order phase transition to a ordered vortex state with the formation of ordered stripe structures.

These points illustrate well the subtlety of determining ground state configurations. No calculations were performed so far for the $T_3$ geometry. We tried to draw some ordered vortex structures by applying some simple rules which help to approach a low energy configuration: the number of fluxoids in the network is equal to the applied

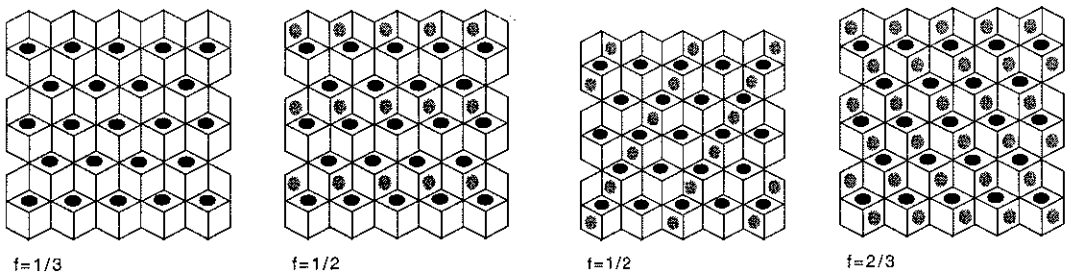


Figure 5.19: Some commensurate states for vortex distribution at frustrations 1/3, 1/2 and 2/3, constructed on the basis of geometric arguments.

flux and adjacent occupied cells should have a minimum of common nodes (maximum separation which minimizes vortex repulsion). Some commensurate vortex configurations at frustrations 1/3, 1/2 and 2/3 are presented on Fig. 5.19. The configurations at 1/3 and 2/3 have the 6-fold degeneracy associated with the lattice symmetry. At half-flux several commensurate distributions of vortices can be obtained, as those illustrated. Such ordered configurations should not be observed if the phase coherence vanishes at half-flux as predicted.

### 5.6.2 Experimental details

The superconducting wire networks are obtained from an epitaxial niobium film of 200 nm thickness. The wires patterning is performed by *Reactive Ion Etching* with $SF_6$ gas through a metal aluminium mask of 30 nm. The etching time is controlled in order to leave a bottom niobium layer of 70 nm which will be used as compression layer for the decoration. The details of the patterning process are described in Chapter 2. Several networks are patterned in a row and distant of 0.2 mm from each other to avoid perturbations from adjacent networks. The total number of cells per network is 650, the lattice constant $a$ varying from one network to the next by 0.1 $\mu$m, for $a$ between 2.5 $\mu$m and 3.5 $\mu$m. Therefore, for a given magnetic field, we have a set of different frustrated networks which are simultaneously decorated. The magnetic field correspondent to frustration 1/2 is calculated for the network whose lattice constant is 3.0 $\mu$m, defining frustration $f = BS_{cell}/\Phi_o$ as the applied flux per unit cell surface $S_{cell} = a^2\sqrt{3}/2$, which gives 0.135 mT. The cells wire width varies between networks, 0.3 $\mu$m and 0.7$\mu$m for the smaller and the larger tiles, respectively. A set of square

networks is patterned in another row, with the same cell areas than the correspondent star network in the upper row, therefore the same frustration. These square networks are used to confirm the position of the frustrated network at half-flux by identifying the checkerboard configuration.

The samples are cooled in applied field from above 9.2 K to 8.6 K at a controlled rate of 0.1 K/s. Above 8.6 K the wires are superconductive while the bottom layer is still in the normal state, therefore it should not interfere in the fluxoid distribution. At the 8.6 K the bottom layer becomes superconductive and the heating is turned off, and all cooled to 4.2 K at a rate of 1.6 K/s. The faster cooling favours the pinning of the previous fluxoid distribution on the compression layer and by the network itself.

### 5.6.3 Experimental results

For all networks the applied frustration $f_{applied}$ agrees well with the frustration observed experimentally $f_{exp}$, indicating that effects such as field screening, vortex migration or creation/aniquilation of vortex-antivortex pairs are negligible (or at least compensated). We define $f_{applied} = BS/N\Phi_o$, where B is the applied field, $S$ the network area and $N$ the total number of cells. $f_{exp}$ is obtained dividing the number of occupied cells by N. In general we didn't observe more than one vortex per cell. The error on $f_{exp}$ depends on the ability to identify an occupied cell, which we estimate to be largely below 0.03 (20 vortices per network). The frustrations of some decorated networks are summarized in Table 5.6.3.

| network | a [$\mu$m] | $f_{applied}$ | $f_{exp}$ | vortex ordering | defects |
|---|---|---|---|---|---|
| A | 2.5 | 0.32 | 0.32 | domain 1/3 | point like |
| B | 3.0 | 0.51 | 0.50 | disordered | |
| C | 3.1 | 0.55 | 0.52 | 1D stripes | |
| D | 3.2 | 0.57 | 0.54 | 1D stripes | |
| E | 3.4 | 0.66 | 0.66 | domain 2/3 | point like |

Table 5.1: Applied $f_{applied}$ and experimental $f_{exp}$ frustrations for several networks.

SEM photographs of decorated networks with frustrations 0.32 (network A), 0.50

(network B), 0.52 (network C) and 0.66 (network D) are presented in Figs. 5.20 to 5.21, respectively. The white spots indicate the vortices positions.

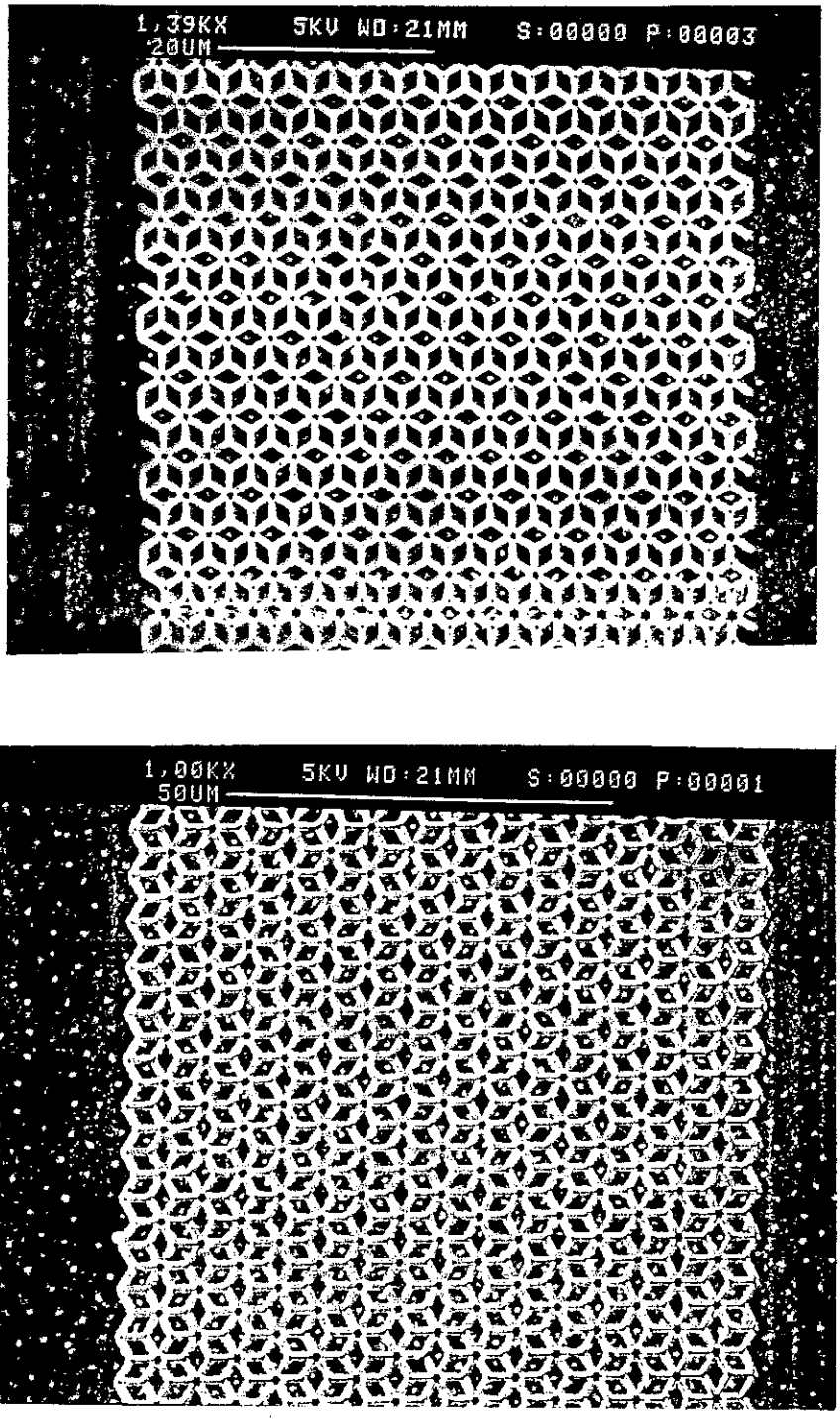


Figure 5.20: SEM photographs of decorated network at frustrations f=0.322 (top) and 0.66 (bottom).

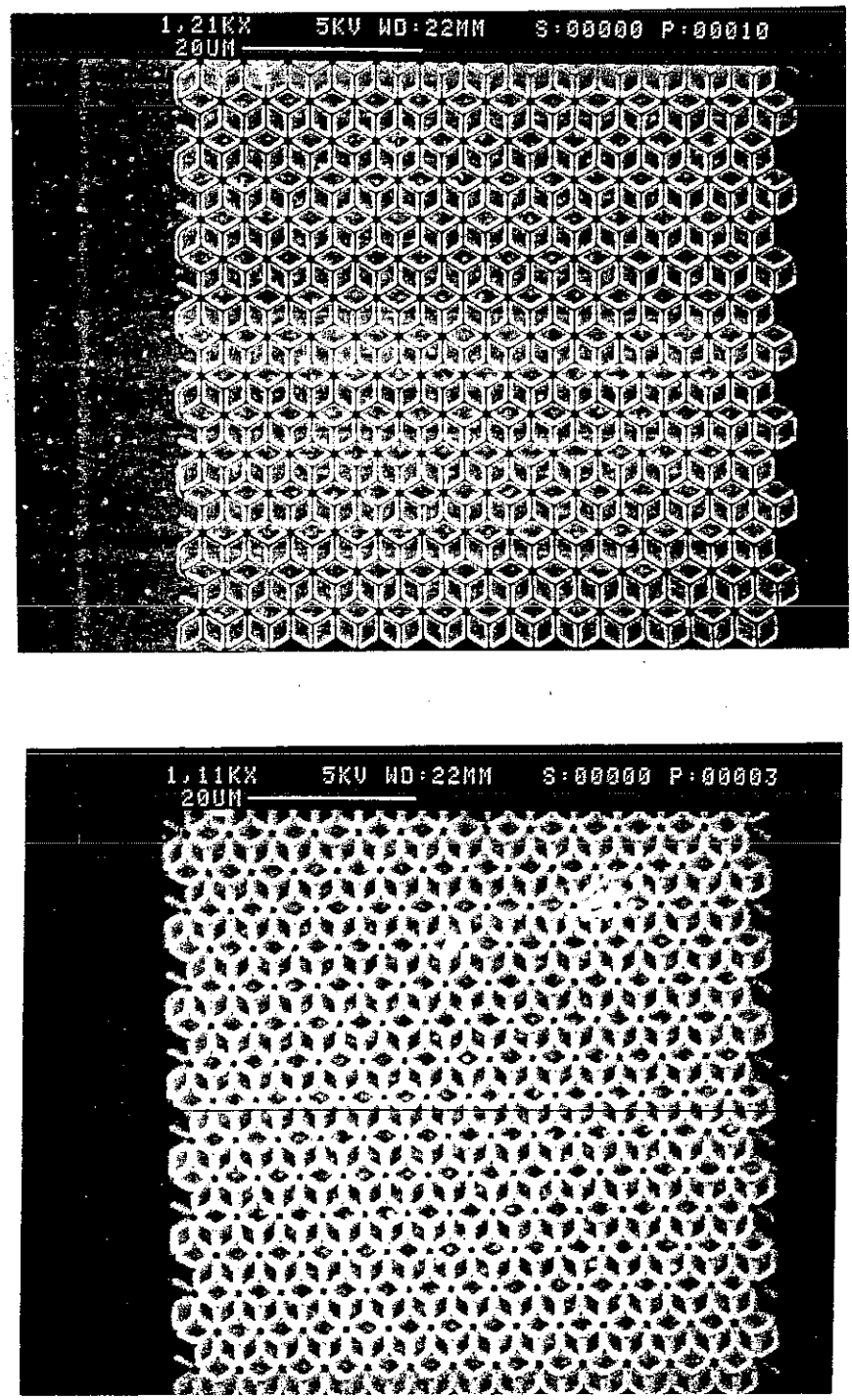


Figure 5.21: SEM photographs of decorated network at frustrations f=0.50 (top) and 0.52 (bottom).

We can clearly distinguish a periodic arrangement for network A, the one closer to frustration 1/3. Vortex patterns at 0.66 and half frustrations are more difficult to identify, due to the higher vortex density. For clarity it is displayed in Figs. 5.22 to 5.23 the vortex distributions for several networks, with the occupied cells represented by colour dots (the network itself was removed). The colour scheme facilitates the identification of ordered vortex structures. Each colour corresponds to different cells rotation within the network (see inset of Fig. 5.22). The black dots correspond to occupied horizontal cells, the light grey to a cell rotated by 60° and the dark grey to a cell obtained by 120° rotation of the horizontal one.

On network A (Fig. 5.22, $f_{exp}$=0.32) we identify the 1/3 ordered vortex configuration illustrated in Fig. 5.19 (rows of black dots) on a single domain covering the whole network. When comparing the fraction of occupied cells with a given orientation, the black cells have about 90% occupancy as displayed on the graph of Fig 5.22. No domain walls are identified but a few random point like defects (vacancies). These defects are in equal number of the occupied grey tiles, indicating that those missing in the ordered 1/3 structure moved into these cells. For network E (Fig. 5.23, $f_{exp}$ =0.66), we find a central domain with the 2/3 configuration illustrated in Fig. 5.19, formed by ordered stripes of alternate light grey and dark grey cells, which run over the whole network width. This distribution is the dual of the 1/3 configuration (empty tiles are reversed). A similar duality was previously observed on the square lattice between the states at frustrations 1/3, 2/3 and 2/5, 3/5 [54]. The occupancy of the dark and light grey cells is equivalent and almost 80%, as expected for an extended ordered domain. This ordered state presents more point like disorder (black dots) than at 1/3. The number of vacancies (empty cells) in the ordered 2/3 stripes is about 18% of the total number of vortices in the network and equivalent to the number of occupied black tiles.

Network B (Fig. 5.24, $f_{exp}$=0.50) is the one closer to the half-flux frustration. We observed the checkerboard configuration for the square network with the same lattice constant indicating that these networks do correspond to the half-flux frustration. In contrast, the vortex distribution for the $T_3$ network is very disordered. We cannot identify any extended ordered domain, in particular none of the configurations

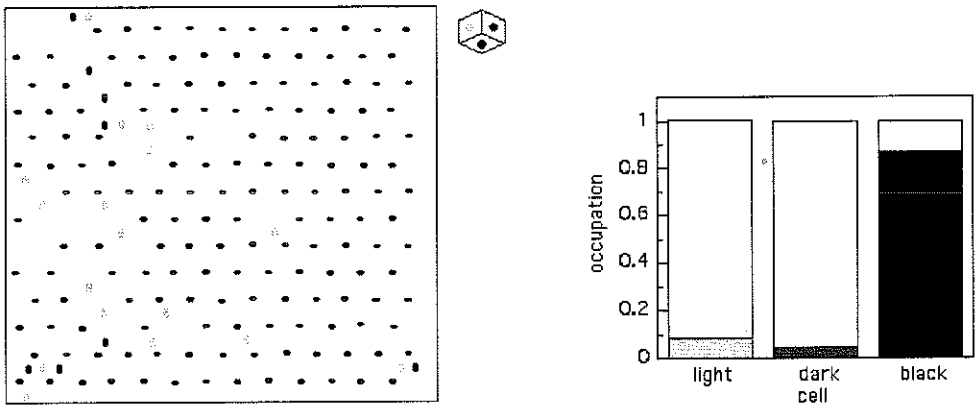


Figure 5.22: Vortex distribution for network A with $f_{exp}$=0.322.

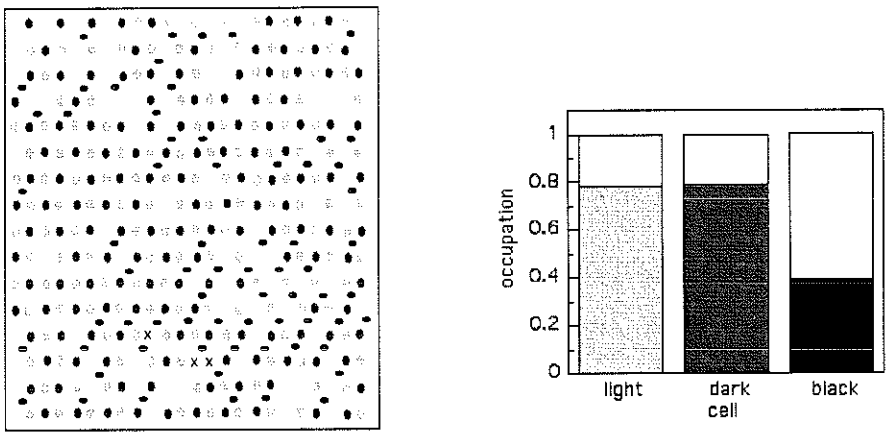


Figure 5.23: Vortex distribution for network E with $f_{exp}$=0.66.

presented in Fig. 5.19 for half-flux.

Some isolated short length rows (four cells) of occupied tiles displaying the 1/3 and 2/3 stripe order can be identified with different orientations or a few patches (4 to 8 vortices) with the 2/3 and 1/3 configurations. The occupied dark and light grey cells are present in equal proportion, which is about half of the black cells occupation. The dominance of the black cells might be due to boundary effects at the network limits. For the networks C and D (Fig. 5.24, $f_{exp}$ =0.52 and $f_{exp}$ =0.54, respectively), the formation of 1D ordered structures (2/3 ordering) which extend up to 10 vortices are now clearly visible and for all directions. In the case of network D, the occupation of the different tiles is very similar.

More information on the vortex order can be obtained from the distribution of the occupied cells coordination. For the $T_3$ topology, each cell is surrounded by four

nearest neighbour cells, therefore the coordination of an occupied cell can range from zero (if no surrounding cells are occupied) to four. If ordered vortex distributions are present, the correspondent coordination distribution should exhibit an ordered pattern. The coordination distributions of the decorated networks at frustrations $f = 0.32, 0.50, 0.54$ and $0.66$ are displayed in Fig. 5.6.3. To each occupied cell we assigned a colour correspondent to its coordination. The black tiles correspond to occupied cells at the network edges and are not considered. The coordination patterns of the ordered configurations displayed in Fig. 5.19 for the 1/3, 1/2 and 2/3 vortex states is also displayed.

At $f = 0.32$ the extended 1/3 domain (coordination 1, blue tiles) is clearly visible. At $f = 0.66$ we identify the 2/3 domain (coordination 2, yellow tiles) which covers about half the network surface. The regularity of this distribution is disrupted on some regions due to point like disorder which is indicated by small crosses. For the network at half-flux we can only identify some short 1D stripes of coordination two, while other coordinations are also present. Finally, in the network at $f = 0.54$ we can identify a central domain of coordination 2, corresponding to two small domains of the 2/3 state separated by a domain wall.

A comparison between the probability of occurrence of a given coordination for the different networks (number of cells with the same coordination divided by their total number) is displayed in Fig. 5.26. For the network at $f = 0.32$ the coordination 0 reaches almost 100% while the network at 0.66 has mostly coordination 2 for 60% of the occupied cells. The network at 0.50 has about the same fraction of 1-fold and 3-fold coordinated cells, while the coordinations 0 and 1 are also present on 10% each.

These results indicate that the vortex arrangement at half-flux is indeed very disordered. Besides the presence of a few short range 1D stripes (4 vortices) for network B, we could not identify any ordered domain, but a few clusters of maximum 6 vortices displaying the 2/3 or the 1/3 ordering. On the other hand, the networks at frustrations close to half-flux display At frustrations 1/3 and 2/3 we identified ordered commensurate states with some point like defects but no domain walls were identified.

The inversion of the dominant occupied tiles at frustrations 1/3 (network A) and

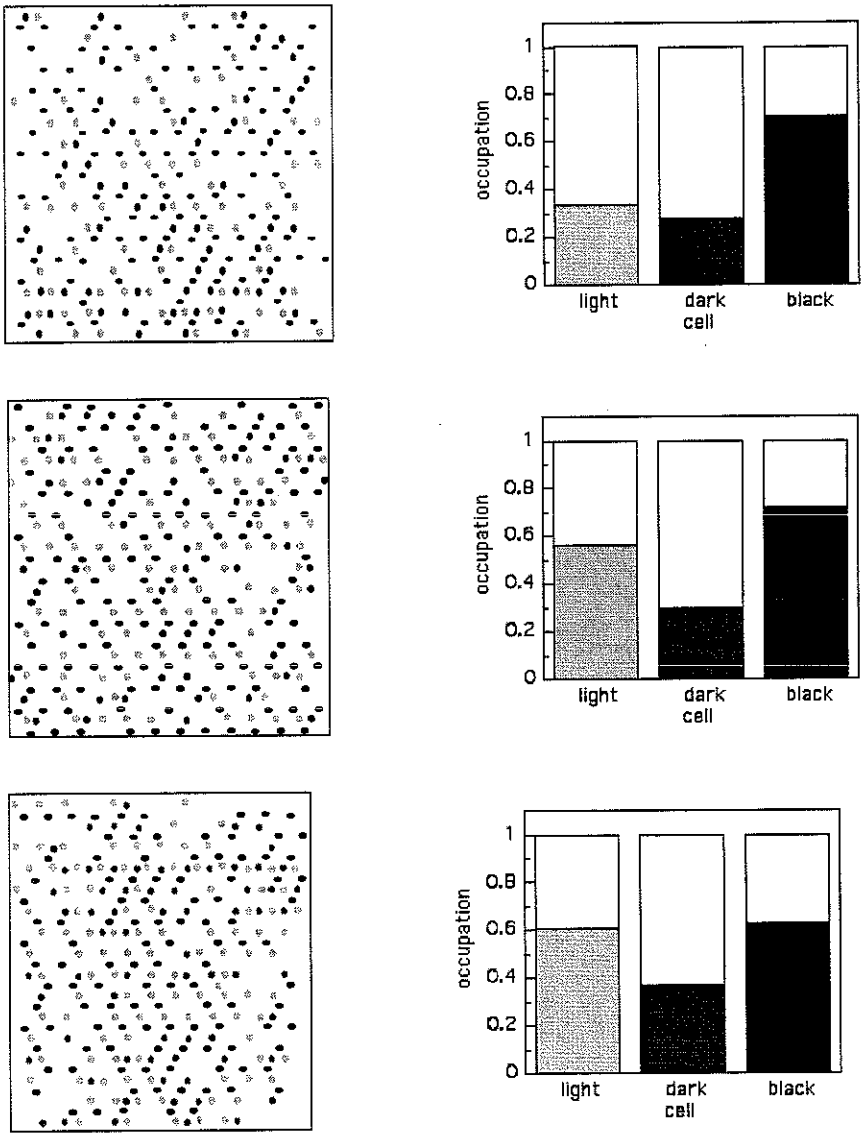


Figure 5.24: Vortex distributions and cell occupation rates at different frustrations. From top to bottom: network B with $f_{exp}$=0.503, network C with $f_{exp}$=0.52 and network D with $f_{exp}$=0.54.

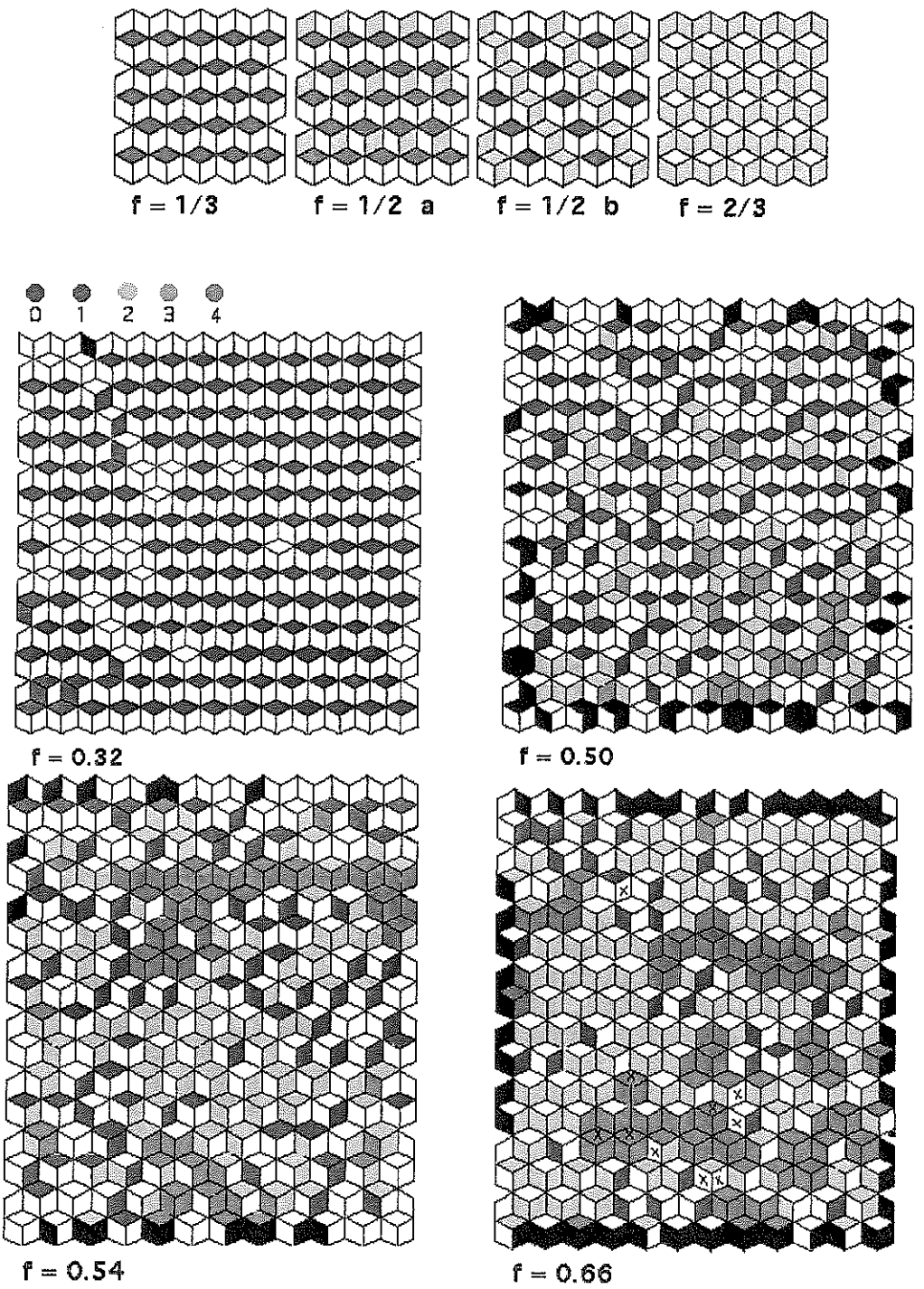


Figure 5.25: Vortex coordination at different frustrations for the configurations of Fig. 5.19 and the decorated networks. The coordination colour scheme is also displayed.

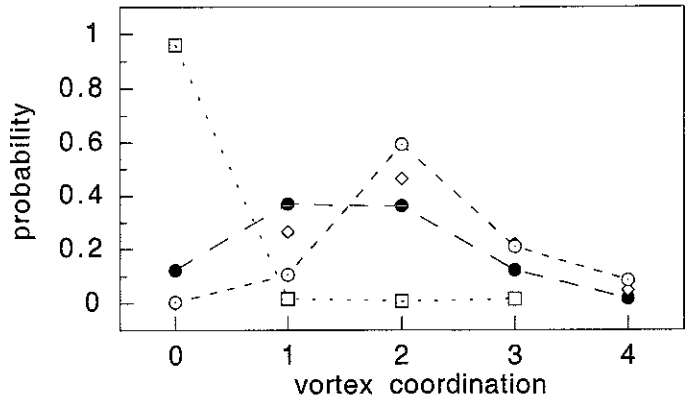


Figure 5.26: Experimental probability distributions for the vortex coordination at different frustrations: 0.32 (□), 0.50 (•), 0.54 (◇), and 0.66 (⊙).

2/3 (network E) as well as the selection of the rows parallel to the network edges is not clear. In fact these rows lead to the most homogeneous distribution of vortices inside the network, since they have the same length and first neighbours than the adjacent ones, in contrast to the rows in the network diagonals, of different lengths. For an ordered distribution, the occupation of the parallel rows may thus lower the systems energy. Another possible reason is the network finite size. In an infinite periodic lattice with hexagonal symmetry, ordered configurations are 6-fold degenerate and no preferred direction should be selected, however on finite size samples conditions at the edges may lead to a preferential orientation. On the other hand, if long range ordering is absent as expected at half-flux, the above arguments may no be longer valid. In fact the diagonal rows on the networks close to half-frustration are equally occupied as the parallel ones.

## Characteristic energies of wire networks

In the previous discussion, we assumed that the vortex configurations identified at 4.2 K correspond to the ground states determined close to the network transition temperature. In the following, we will give a simple estimation of the characteristic energies involved and how realistic this approximation is.

The final vortex distribution observed by decoration in a wire network will depend on the thermal fluctuations and the two characteristic energies of the system: the pinning energy arising from the condensation energy when one vortex crosses a wire

$U_{core}$, and the coupling energy $E_J$, related with the kinetic energy of the supercurrents distribution. The pinning energy depend on temperature as well as on the network lattice constant $a$, wire width $w$ and coherence length $\xi(0)$. The typical parameters of our Nb networks are $T_c = 9.1\ K$, $\xi(0) = 20$ nm and $\lambda(0) = 0.1\ \mu$m. Using the dimensions of network B ($a = 3.0\ \mu$m, $w = 0.35\ \mu$m and wire thickness $d = 0.1\ \mu$m) we see that this network will cross different pinning regimes during the cooling from above $T_c$ to the 4.2 K at which the decoration is performed. In the regime close to $T_c$, where $\xi(T) \geq a$, the coreless vortices are extended over several networks cells, therefore they are not sensible to the network discreteness and thus very mobile. In this regime, the vortex distribution is determined by the flowing supercurrents ($E_J$) and the system may relax to its ground state configuration if the cooling is not proceeding too fast. However it is susceptible to thermal fluctuations.

When the temperature regime $a \geq \xi(T) \geq w$ is crossed, the coreless vortices will be confined within the network tiles and besides the coupling energy, they will be subjected to an overall pinning barrier which can be described by [65],

$$U_B(T) = [0.94\frac{a}{\xi(T)} - 2.46]E_J \tag{5.22}$$

where $2.46E_J(T)$ is the coupling energy between nodes for a square unit tile, and the first term is related to the loss of condensation energy each time a vortex crosses a wire that is driven normal. The coupling energy for a strongly coupled wire network is proportional to the supercurrent flowing between adjacent nodes and the phase difference between them, and for a square network can be simply expressed by,

$$E_J(T) = \frac{\Phi_o^2 wd}{4\pi\mu_o\lambda(T)^2 a} \tag{5.23}$$

In this regime the vortex configuration will be pinned if thermal fluctuations are negligible, as well as vortex-antivortex pairs that might have been thermally created.

Using the Nb network parameters, we obtain $E_J(0) = 1 \times 10^{-19}$ J. and the temperature regime below which the pinning barrier is effective ($U_B \geq k_B T$) will be $T \leq T_c - 3$ mK.

Therefore, we can consider that the observed vortex arrangements correspond to the vortex configuration established close to the transition and strongly pinned

below $T = T_c -$ 3 mK. It also means that when the compression layer will become superconducting (at 8.6 K) it should not alter the initial vortex distribution. The creation of vortex-antivortex pairs will only be important at temperatures $k_B T \geq E_J(T)$, that is for $T_c - T10$ mK, in zero field.

Finally, using Eq. 5.18 for the effective penetration length, we find that it is comparable or larger than the total network area for temperatures $T_c - T \leq 100$ mK, therefore the networks are uniformly frustrated close to the transition temperature when the vortex distribution is established. When screening effects at lower temperatures become important the vortex distribution will be already pinned by the compression layer and the network itself.

## 5.7 Concluding remarks

Our transport measurements on 2D superconducting networks with the so-called $T_3$ geometry allowed us to confirm some of the exotic features of the $T_3$ energy spectrum related to the localization mechanism. The normal to superconductor transition line was measured as a function of applied field and related to the ground state of the $T_3$ spectrum, which was found to be in excellent agreement with the theoretical results. The critical current was also studied as a function of applied field and temperature. The critical current at half-flux exhibited the lowest values when compared, in terms of reduced temperature, with those obtained at other rational commensurate states. These results were compared with the theoretical calculations of the group velocity which are based on the knowledge of the band structure. A good qualitative agreement was found, though for a finer comparison it would be necessary to include the non-linear terms of th GL equations, which for a network is a very complex problem. The striking behavior found at half-flux was discussed as a possible signature of the studied localization effect. The strong broadening of the normal to superconductor transition supports this interpretation. Finally, we also studied the vortex distributions in superconducting networks of niobium by imagery of the vortices positions by Bitter decoration. The states at half-flux and at the strong commensurate fields, f=1/3 and f=2/3 were analysed. We identified ordered structures at frustrations 1/3 and 2/3,

which are a signature of the presence of phase coherence over the network. In contrast, the state at half-flux was found to be very disordered and no domain structure was identified. These results indicate that the state at half-flux is indeed very degenerate as theoretically predicted in Ref. [37].

# Chapter 6

# Vortex quenching on superconducting films

La dynamique des transitions de phase par brisure de symétrie du paramètre d'ordre suscite un grands intérêt dans le domaine de la cosmologie mais aussi dans celui de la matière condensée, qui offre des tests expérimentaux pour ces théories. Les couches minces supraconductrices constituent un des systèmes privilégiés pour aborder ces phénomènes. Cependant, du point de vue expérimental plusieurs difficultés se présentent, en particulier l'obtention des taux de refroidissement suffisamment rapides pour obtenir une densité de défauts mesurable, et l'écrantage du champ magnétique terrestre. Dans ce chapitre, on décrit un étude préliminaire visant l'optimisation d'une expérience de *quench* en température avec des couches supraconductrices. La technique de détection choisie est la décoration de Bitter, pour laquelle on a amélioré les taux de refroidissement et inclus une mesure de très bonne résolution du zéro du champ magnétique. Un étude de la résolution de cette technique aux très faibles champs a été effectuée.

# Introduction

The dynamics of symmetry breaking phase transitions has been subject to attention both in high energy physics, due to its implications for cosmology scenarios, as in condensed matter, since this field provides a laboratory test for these theories. The first experiments of this kind were performed on liquid crystals [66],[67] and followed by experiments on $He^3$ [68], [69] and $He^4$ [70], [71] . As initially proposed by Zurek [72], two-dimensional superconductors are good candidates for the study of topological defects formation. These systems also undergo $2^{nd}$ order phase transitions when going from the normal into the superconductive phase, which are associated with the symmetry breaking of the order parameter. If the phase transition is crossed quickly enough, topological defects of the order parameter are formed, whose equivalent in a superconductor are the normal vortex cores. However in this case, the vortices are induced in zero applied field, in contrast to the usual magnetic field induced vortices.

The simplest way to produce a quench in a superconductor is by cooling it rapidly, since the variation of the transition temperature with pressure is negligible (excluding high-Tc superconductors). Nevertheless, on the experimental side two complications are immediately presented. On one hand, the earth magnetic field must be screened and/or well compensated, and on the other hand, the quenching rates must approach the millisecond in order to induce a significant defect density. Since temperature cooling is mostly done by heat conduction, which is a diffusion process driven by temperature gradients, it is limited by the finite thermal conductivity of the samples, heat exchanges with the sample holder, *etc.* However, in 2D films temperature gradient can be neglected with heat transport done in the direction normal to the film surface. Still, the heat exchanges between the film sample and the substrate, sample holder and the contact surfaces limit considerably the cooling rates. The problem of reaching fast cooling rates and the detection of weak vortex densities still remain difficult points.

Our concept of the quenching experiment is as follows: to reduce heat transfer limitations, a thin film sample is maintained at a constant temperature, slightly below its transition temperature, by heat exchanges with its substrate and the sample holder. Then, the sample is heated above its transition (for example by 0.5 K) by an

incident light pulse, short enough to avoid heating the substrate and sample holder. In optimum conditions, the cooling rate of the sample after the pulse will be only limited by the heat exchanges between the film and its substrate. The presence of topological defects, which in a superconducting Nb film will be the supercurrents loops (vortices) originated at the intersection point of phase coherent domains of different phase choice, can then be detected by Bitter magnetic decoration. A disadvantage of this technique is that it cannot discern between a vortex and an antivortex.

In this chapter it is described a preliminary study for temperature quenching in superconductor thin films in our decoration chamber. The cooling rates attained in the chamber were characterized as well as the magnetic sensitivity of the experiment to the detection of low vortex densities. Decoration experiments done at zero applied field revealed the presence of vortices, which we related to a small but non-zero effective magnetic field. A high precision measurement of the applied field using Josephson junction arrays was then installed, which is described in Chap. 3.

## 6.1 General background on topological defects formation

Topological defects formation in cosmology scenarios can be discussed in an equivalent form in superconductive systems due to the similar behaviour of the free energy close to the phase transition. The potential energy has the Ginzburg-Landau form:

$$V(\psi) = \alpha(T)|\psi|^2 + \frac{\beta}{2}|\psi|^4 \tag{6.1}$$

where $\psi$ is the order parameter, $\alpha$ a coefficients whose dependence on the relative temperature $\epsilon = T/T_c - 1$ is given by, $\alpha(T) = \alpha_o\epsilon$ and $\beta$ is taken as constant. $T_c$ is the phase transition temperature.

The shape of the potential energy in three dimensions is illustrated in Fig. 6.1. Above the phase transition ($T > T_c$, $\alpha > 0$), the system is near equilibrium in the symmetric phase with $< \psi >= 0$ everywhere , for which the potential energy $V(\psi)$ has the single minimum. Below the transition ($T < T_c$, $\alpha < 0$), the potential energy takes the *sombrero* shape with a degenerate minimum at $< \psi >= |\psi_o| = \sqrt{|\alpha|/\beta}$, for

which different choices of the order parameter exists (different choices in the direction it points) and the vacuum symmetry is broken.

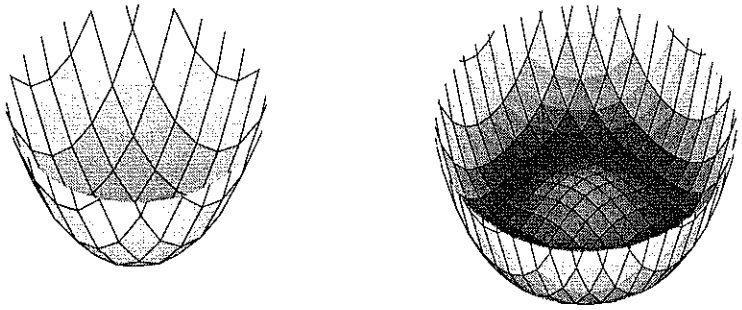

Figure 6.1: Potential energy in three dimensions. One single minimum with $V = 0$ exist above the transition (right). Below the transition the potential acquires the *sombrero* shape with degenerate minima at $V = -\alpha^2/2\beta$.

Below $T_c$, in equilibrium the true ground state corresponds to a spatial uniform $<\psi>$ since the gauge field involves the first derivative of the order parameter. However, in a non-equilibrium situation, such as cooling rapidly through the transition, the order parameter may not have time to relax to its equilibrium thermodynamic value. Since a perturbation of the order parameter propagates with a finite speed in a length of the order of the coherence length $\xi(T)$, at sufficient distances the choices of the order parameter will be done randomly and a domain structure corresponding to independent choices of $\psi$ is formed. Part of this structure will die out quickly since an uniform $\psi$ is energetically preferred, however some defects may remain trapped. That's why a rapid method for the detection of these defects is also required.

Though it remains unclear the mechanism responsible for topological defects formation, an important effort towards the experimental detection of the defect density has been developed and experimental results confronted with the two main theoretical scenarios, proposed by Kibble [73] and Zurek [72], respectively.

In both, the initial density of defects is set by the size of the domains with broken symmetry, which is determined by the coherence length value $\hat{\xi}$, when the initial domain structure is established. Essentially the two scenarios differ on what sets $\hat{\xi}$. Kibble's mechanism is essentially an activation mechanism, where the initial domain size will be determined by the Ginzburg temperature $T_G$, which sets the critical temperature above which thermal fluctuations become important. Zurek's scenario

is based on the concept of *critical slowing down*, for which it is the dynamics of the order parameter close to the transition that will set the initial defects density.

So far, Zurek's scenario seems to be in better agreement with experiments performed in irradiated superfluid $He^3$. Nevertheless, the interplay between thermal activation and the critical slowing down have yet not been addressed in detail. Probably they both intervene. Zurek argued that if the freezing temperature $T_{frozen}$ lies below $T_G$, since the dynamics of the order parameter will be frozen for $T > T_{frozen}$, it is the critical slowing down that will set the initial defect density. Experiments performed with different quenching rates could help to discern between both mechanisms, though the time decay of the initial density may severely limit this analysis.

### 6.1.1 Kibble's mechanism

Kibble [73] proposed a thermal activation mechanism which, close to the transition, induces fluctuations of the order parameter back to $< \psi >= 0$ or to the other degenerate choices of $\psi$ below $T_c$, $< \psi >= |\psi_o|$. These fluctuations are highly probable as long as the thermal energy is enough for *flipping* the locally uniform domain, of a given $\hat{\xi}$ and $\psi$ choice. The minimum energy required to overcome the potential energy barriers separating degenerate minima is given by the condensation energy in a volume $\xi^2$,

$$E_c(T) = \xi^3(T)\frac{\mu_o H_c^2(T)}{2}, \tag{6.2}$$

where $H_c(T)$ is the thermodynamic critical field. The critical temperature regime close to $T_c$, where the thermal *flipping* occurs, is set by the Ginzburg condition,

$$|\epsilon_G| = |T_G/T_c - 1| = (k_B T_c/E_c)^2$$

, where $T_G$ is the Ginzburg temperature below which the *flipping* events cease. Though the cooling through $T_c \rightarrow T_G$ must occur with a faster rate than the finite time scale for a *flipping* event to occur in order to *freeze out* the domain structure, Kibble considered that the domain size would be ultimately set by $\xi(T_G)$, independently of the quenching rate.

### 6.1.2 Zurek's mechanism

Within Zurek's scenario [72, 74] it is considered the only way the order parameter can become correlated is through its dynamics.

The dynamics of the order parameter close to the transition is characterized in space and time by two simultaneous divergent length scales: the coherence length,

$$\xi(\epsilon) = \frac{\xi(0)}{\sqrt{|\epsilon|}} \tag{6.3}$$

which sets the dye-out distance for an order parameter perturbation (it is thus the space scale of the perturbation itself), and the dynamic relaxation time,

$$\tau = \frac{\tau_o}{\epsilon}, \tag{6.4}$$

which sets the time required for the order parameter to relax to its equilibrium value. $\tau_o = \pi\hbar/8k_BT_c$ is a material dependent constant [34].

Since both parameters diverge close to the transition, the evolution of the order parameter is slowed down near $T_c$. If while cooling from above the transition, at a given instant of time, the relaxation time $\tau(t)$ becomes larger then the remaining time $\hat{t}$ to cross the transition, then the order parameter will not have time to adjust everywhere to the equilibrium values, being correlated only in a finite distance set by the coherence length at that instant, $\hat{\xi}$.

The instant $\hat{t}$ is called the *frozen out* and is defined as,

$$\tau(\hat{t}) = \hat{t} \tag{6.5}$$

where the instant zero is when the system is at the transition temperature $T = T_c$, and $t > 0$ at $T > T_c$ ($t < 0$ at $T < T_c$)

The *frozen-out* scenario is illustrated in Fig. 6.2. When the system recovers its dynamics at a lower temperature (or at an instant $-\hat{t}$), the symmetry breaking transition already took place and if $T < T_G$, the initial *frozen* domain structure remains. The size of the domains with the same choice of vacuum is set by the coherence length at the freezing instant, $\hat{t}$.

Within this scenario the initial density of defects depends on the quenching rate.

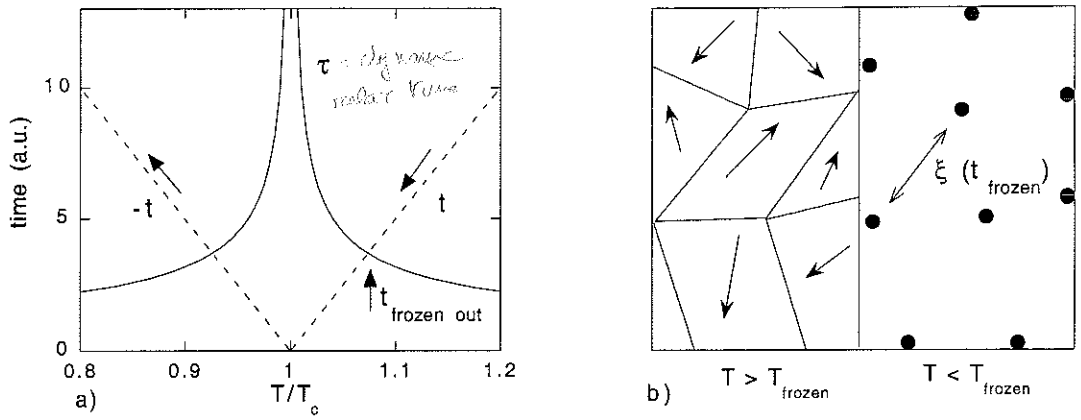


Figure 6.2: a) Variation of the time scale $\tau$ (solid line) during cooling down through the transition. The cooling time $t$ is represented by dashes lines. $t = 0$ at $T = T_c$. b) Representation of the domains with broken symmetry with independent choices of $\psi$ (arrows) at $T > T_{frozen}$ and frozen defects at $T < T_{frozen}$.

## 6.2 Temperature quenching rate in the decoration chamber

We began an optimization study of the decoration chamber for the detection of vortex formation on a superconductor film during a temperature quenching through the transition. Since the film cooling in the decoration chamber is done through heat exchanges with its substrate, the film cooling rate will be always limited by electron-phonon exchanges between the film and its substrate. Moreover, the exchanges between the substrate and sample holder will also limit the cooling, namely when the sample is cooled by simply turning off the heating power of the sample holder. We characterized the cooling rate attained in the decoration chamber by this method and improved it by using a pulse of light to heat the film, while the sample holder is kept at a constant temperature.

### 6.2.1 Determination of the experimental cooling rate

The decoration chamber used in our experiments was optimized to perform decorations at a fixed temperature of $T = 4.2$ K. We are thus constrained to use supercon-

ductor samples with higher transition temperatures, such as niobium films. All the characterization is thus performed in the temperature range of interest for niobium films. These samples are suitable to our experiments since we can evaporate epitaxial Niobium films of high quality. The films thickness is 200 nm, comparable to the coherence length at zero temperature, therefore close to the normal-superconductor transition the film can be considered two-dimensional. Finally, we count on the strong intrinsic pinning of niobium to trap the low density of induced vortices as well as to prevent vortex-antivortex recombination.

In order to estimate the cooling rates attained in this chamber, we used a thin film thermometer sample of Au-Ge, with some similar characteristics to the niobium samples to be decorated, that is, similar contact surface, and substrate thickness. The Au-Ge films are resistance thermometers developed in C.R.T.B.T.[75] and are suitable to our measurements since they are very sensitive in a broad temperature range (10 mK to 1000 K) and have very short relaxation time constants at low temperatures (below 2 ms at 50 mK).

Their resistance increase with decreasing temperature by a power law,

$$R(T) = R_o T^{-a}. \tag{6.6}$$

where the constant $a$ determines the thermometer sensitivity. For an ideal resistance thermometer $R_o$ is of the order of a few k$\Omega$ and $a = 0.8$. Since $a = -\partial \ln R / \partial \ln T$, the resolution in temperature $dT/T$ is only limited by the resolution attained in the resistance measurements, $adT/T = dR/R$. We first calibrated our thermometer and then estimated the cooling rates by monitoring the film resistance as a function of time.

#### 6.2.1.1 Calibration of the Au-Ge thermometer

The sample is a 200 nm thin film of Au-Ge alloy, deposited by sputtering on a oxided Si wafer of thickness 290 $\mu$m. Gold strips for the electrical contacts are sputtered with a separation of 1 mm. The sample dimensions are 6 mm$\times$4 mm.

The sensitivity of these films, at low temperatures is known to increase after annealing during one hour, the best characteristics being obtained for temperatures

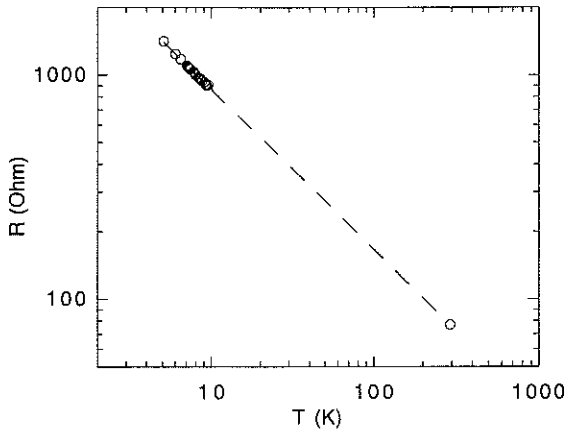


Figure 6.3: Au-Ge film resistance (open symbols) at several temperatures and the linear fit to the data on log-log scale (dashes line).

between 110°C and 160°C [75]. The optimum temperature can be found by monitoring the variation of the sample resistance with increasing annealing temperature. Initially, the Au-Ge resistance decreases and reaches a minimum at the optimum annealing temperature, before restarting to increase. This optimum temperature for the present sample was 110°C at which it was annealed during one hour. The final resistance at ambient temperature was 76.813 Ω.

The thermometer calibration was then performed by measuring its resistance at several temperatures between 4 and 10 K and at ambient temperature.

The power law parameters $a$ and $R_o$ are then determined from a linear fit of the experimental data in a log-log scale, which gives

$$R(T) = 4.498 \times 10^3 \; T^{-0.72} \; (ohm). \tag{6.7}$$

The thermometer resistance at several temperatures as well as the data fit are displayed in Fig. 6.3.

#### 6.2.1.2 Sample cooling by turning off the heating power

We firstly determined the cooling rate of the Au-Ge sample when the heating power of sample holder is turned off, by monitoring the variation of the sample resistance in a fixed amount of time. In this case, the cooling is mainly limited by heat conduction between the sample, the sample holder and the cold point at 4.2 K. The heat transfer

with the cold point is done through a thin copper wire heat leak (for further details, refer to chapter 3). The other processes depend on the sample and substrate thermal conductivity, thickness, surface, as well as the heat transfer through the contact surfaces.

For several initial sample temperature between 8.5 K and 15 K we obtained on average a cooling rate of 0.15 K/s, which is independent of the initial sample temperature. This rate is mostly determined by the heat exchanges between the sample holder and the cold point at 4.2 K through the heat leak.

The heat flow $Q$ through a metal bar whose extremities are kept at a temperature T and $T_o = 4.2\ K$, respectively, is given by,

$$Q = \frac{S}{L}\int_{4.2}^{T} k(T)dT \tag{6.8}$$

where $Q$ is the heat flow in watts, $S$ the cross section area in $cm^2$, $L$ the bar length in cm and $k(T)$ the thermal conductivity in watts/cm-°K. The thermal conductivity integral for a copper wire with T=9 K is 25.8 watts/cm.

After substitution of the heat leak by a shorter (1/0.22) and a thicker (2.6 larger in diameter) copper wire, the cooling rate was improved by a factor of 10, to 1.6 K/s. However, with the new heat leak in order to maintain the sample at 10 K, we were almost in the limit of our heating power supplier. In fact, the heat flow in watt necessary to maintain a temperature gradient of 9.2 K to 4.2 K at the heat leak extremities, is 2.1 mW for the previous heat leak and 62.7 mW for the second one. The maximum heating power of the heat controller is limited to 100 mW. Therefore, a further increase of the cooling rate by changing the heat leak is not possible without loss of temperature stability at 9.2 K.

#### 6.2.1.3 Cooling rate using a LED as a heating source

The cooling rate will also be ultimately limited by heat diffusion through the contact surfaces and the thermal conductivity of the substrate. We thus tried to increase the cooling rates by maintaining the sample at a constant temperature, a few mK below the transition temperature, and heat it through the transition with a short pulse of heat, using a flash of light. In this case, only the thermal conductivity and heat diffusion of the metal film will limit the cooling rate

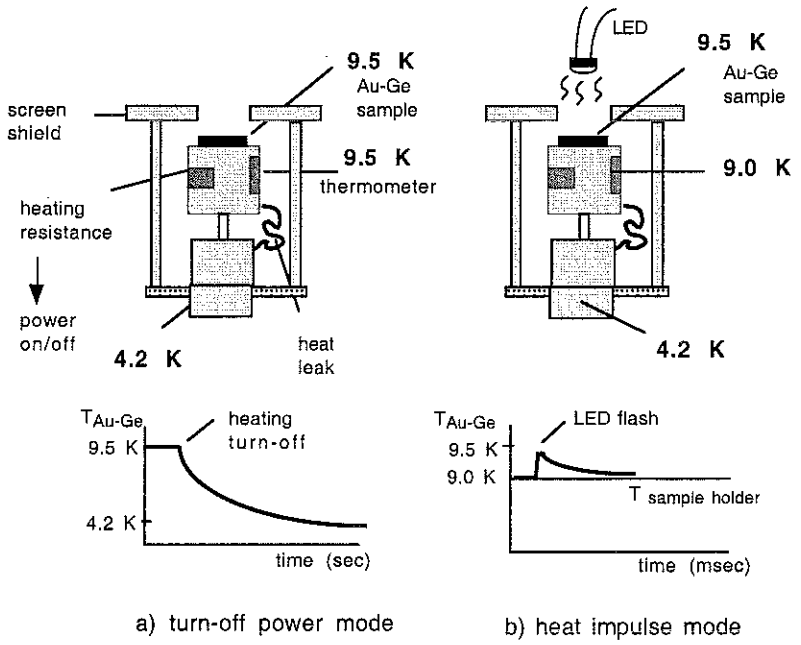


Figure 6.4: Schematic representation of the sample holder and the two cooling modes by: a) turn-of the heating of the sample holder, the sample follows its temperature; b) heat impulse mode: the sample holder is kept at a constant temperature (for *e.g.* 9.0 K) and only the sample is heated of 0.5 K by light radiation from a mounted LED.

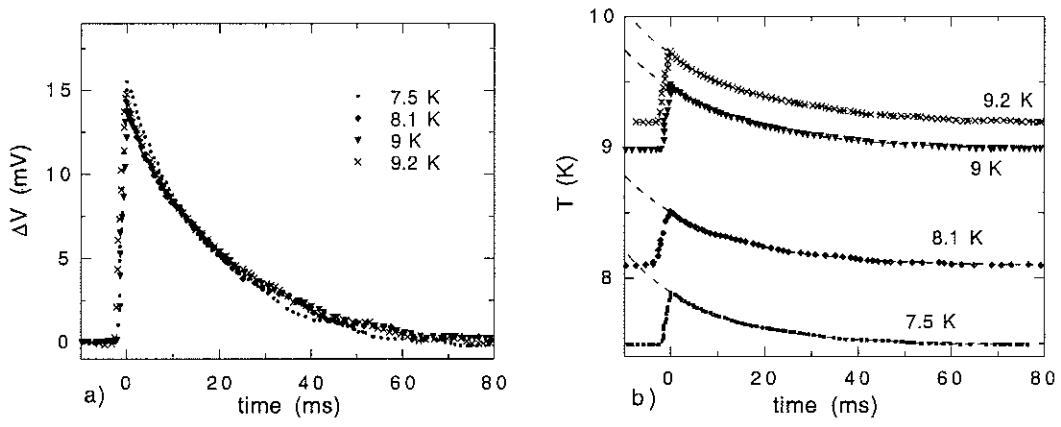


Figure 6.5: Variation of the voltage across the Au-Ge film after a pulse of light during 2.4 ms at different initial temperatures.

The experimental set-up is illustrated in Fig. 6.4. A pulse of current is fed to the LED to produce a flash of light. The sample heating due to the LED depend on the initial sample temperature and the duration of the flash pulse which can be varied.

The light pulse is generated by feeding a square pulse voltage of 6.0 V amplitude during 2.4 ms. This pulse generates a temperature increase of about 0.5 K for an initial sample temperature between 7.5 K and 9.2 K, in the range of interest for the quenching experiments with Nb thin films. The voltage across the Au-Ge film is measured using an oscilloscope and a measuring current of 2 $\mu$A. In Figure 6.5.a) is displayed the voltage variation across the sample after the light pulse, for different initial sample temperatures. The film resistance is sharply raised during the pulse and then decreases following approximately an exponential decay. In Fig. 6.5.b) is represented the correspondent temperature variation calculated using Eq. 6.7. As seen, after the pulse, the sample relaxes to its initial temperatures in approximately 60 ms. Since this time is much larger than the initial temperature raising time (2.4 ms), this decay rate is related with heat exchanges and not with the time response of the sample itself. The exponential decay suggests that the cooling is dominated by transient heat conduction of a thin slab (temperature gradients neglected) through its contact surface. In this case, the temperature after the pulse $T_{max}$, will relax back to the initial temperature $T_o$, as

$$T(t) - T_o = (T_{max} - T_o)\ e^{-t/\tau_Q} \tag{6.9}$$

with $\tau_Q = d\ C_p\ \rho /\ k_{heat}$, where $d$ is the film thickness, $C_p$ and $\rho$ the specific heat and the density of the material and $k_{heat}$ a coefficient of heat transfer through the contact surface with the film. We estimated the Au-Ge film quenching rate $\tau_Q$ using this exponential law. The fits are displayed in Fig. 6.5 by dashes lines. For all temperatures it was obtained a similar quenching rate, with an average value of $\tau_Q = 19 \pm 1.5$ ms.

### 6.2.2 Estimation of the quenched vortex density

We can estimate the initial density of defects in zero field, using the previous cooling rates and typical parameters for our Nb films. Within Zurek's scenario, the order

parameter is able to adjust to the equilibrium thermodynamic value on a time scale which depends on temperature (thus on time) by $\tau = \tau_o/\epsilon$, with $\epsilon = T/T_c - 1$. The *frozen out* instant takes place when $\tau(\hat{t}) = \hat{t}$, that is, when the time remaining to cross the transition becomes comparable to the adjusting time $\tau(\hat{t})$ of the order parameter.

If we approximate the frozen domain size by

$$\xi(\hat{t}) = \frac{\xi(0)}{\sqrt{\epsilon(\hat{t})}} = \xi(0)\sqrt{\frac{\hat{t}}{\tau_o}} \tag{6.10}$$

and assign one defect per frozen domain, the initial density of vortex lines $n_o$ is set by the coherence length at the instant $\hat{t}$,

$$n_o \approx \frac{1}{\xi(\hat{t})^2} \tag{6.11}$$

For a linear quenching, processing at a constant rate $\tau_Q$,

$$\epsilon = T/T_c - 1 = t/\tau_Q \tag{6.12}$$

where $t$ is the time remaining to cross the transition ($t \geq 0$ for $T \geq T_c$ and $t = 0$ when $T = T_c$). The *frozen out* instant defined by $\hat{t} = \tau(t) = \tau_o/\epsilon(t)$ will occurs at $\hat{t} = \sqrt{\tau_o \tau_Q}$. The frozen instant and initial vortex densities estimated with the quenching rates obtained in the turn off heating mode are displayed in table 6.1. For typical Nb films parameters, $\tau_o = 1.63 \times 10^{-13}$ seconds.

However, we have seen that when the film is heated by a short heat pulse, the cooling is better described by an exponential decay, of the form

$$T(t) = T_o + \Delta T e^{-t/\tau_Q} \tag{6.13}$$

where $T_o$ is the sample temperature before the heat pulse, $\Delta T$ the sample temperature increase due to the pulse, and $t > 0$ is the time counted after the heat pulse.

Since we are interested in a decay rate expressed in terms of the remaining time $t'$ to cross the transition ($t' > 0$ for $T > T_c$, and $t' < 0$ for $T < T_c$), after a suitable variable change, $t \to t' = t_c - t$, where $t_c$ is the instant of time (in the variable t) when $T(t_c) = T_c$, the cooling will be given by,

$$T(t') = T_o + (T_c - T_o)e^{t'/\tau_Q} \tag{6.14}$$

| | $\tau_Q$ | $\hat{t}$ | $\xi(\hat{t})$ |
|---|---|---|---|
| heat leak 1 | 61.3 s | 3.16 $\mu$s | 88.1 $\mu$m |
| heat leak 2 | 5.75 s | 0.97 $\mu$s | 61.6 $\mu$m |
| heat pulse | 0.019 s | 0.38 $\mu$s | 30.5 $\mu$m |

Table 6.1: Quenching rates $\tau_Q$, frozen instant $\hat{t}$ and the initial frozen domain size $\xi(\hat{t})$ for the different cooling rates attained in the decoration chamber.

with $T(t') = T_c$ when $t' = 0$. In this case, the quenching is described by,

$$\epsilon = \frac{T}{T_c} - 1 = \frac{T_c - T_o}{T_c}(e^{t'/\tau_Q} - 1) \tag{6.15}$$

The frozen instant $\hat{t} = \tau(\hat{t})$, will thus be given by,

$$\hat{t} = \sqrt{\tau_o \tau_Q}\sqrt{\frac{T_c}{T_c - T_o}}. \tag{6.16}$$

Assuming an initial temperature $T_o = 9$ K before the heat pulse and $T_c = 9.2$ K, the frozen instant occurs at $\hat{t} = 0.38$ $\mu$s.

On table 6.1 are summarized the frozen instant and the initial frozen domain size ($\approx \xi(\hat{t})$) estimated for the different cooling rates obtained in the previous section and using typical parameters for niobium thin films, $T_c = 9.2$ K and $\xi(0) = 20$ nm. For the heating turn-off modes, the quenching time $\tau_Q$ is estimated for a linear quenching.

As seen from Table 6.1 the initial vortex densities predicted for the cooling in the turn-off heat mode are insufficient, in what concerns the decoration technique (resolution in the applied field and image resolution of one vortex). The results obtained in the heat pulse mode are encouraging: besides the increase of the cooling rate, the exponential cooling law favors an increase of the initial vortex density to values detectable by the decoration technique. However, in all estimations we are neglecting the decay of the initial vortex density due to vortex-antivortex recombination, and

thermal activation, which may decrease considerably the number of created defects.

## 6.3 Decoration results for weak vortex densities

As seen in the previous section, for the best cooling rate the vortex density will still be very weak, corresponding to an average of one vortex per $30 \times 30 \mu m^2$.

We thus tested the magnetic resolution of the decoration technique to very weak vortex densities, since the background of magnetic particles that fall uniformly over the sample may reduce the image contrast when only a few spots of flux gradient are present. The decoration experiments were performed at very low fields, susceptible of inducing a density of Abrikosov vortices comparable with the estimations for the best cooling rate ($B = 2.2$ $\mu$T in the heat pulse mode). All decorations were done using epitaxial Nb films of 200 nm thickness. The samples are cooled from 10 K to 4.2 K in an applied field by turning off the heating, for which the cooling rate is 1.6 K/s and the estimated frozen domain size is $\xi(\hat{t}) = 61.6$ $\mu$m. The details of the decoration procedure are as described in Chap. 3. The decorations were done independently, without compensation of the residual fields which can be different for each experiment. In Figs 6.6, 6.7, and 6.8 are displayed SEM images of the decorated samples without an applied field and for applied fields of 0.01 mT and 0.03 mT, respectively. On the left are represented the negatives of the SEM images (vortices appear as black dots) and on the right the same images after applying a threshold on the gray-scale. All pictures correspond to a decorated surface of $80 \times 60$ $\mu m^2$.

The presence of vortices with zero applied field are easily identified. Assigning one $\Phi_o$ to each, the total flux corresponds to a magnetic induction of B= 4.3 $\mu$T. This induction field is however comparable to typical values of the incomplete screened earth field which was not determined for this experiment, therefore we cannot conclude if they are related to quenching or to a non-zero effective field, or to both. For the other applied fields, we can also identify the vortex structure.

The density of counted vortices per unit surface $n_o$ is displayed for the three cases in Fig. 6.9 as a function of applied field $B_{applied}$. The dashes line represents the vortex density in the mixed state, $\approx B_{applied}/\Phi_o$ (Abrikosov vortices). The vortex

43 mgauss

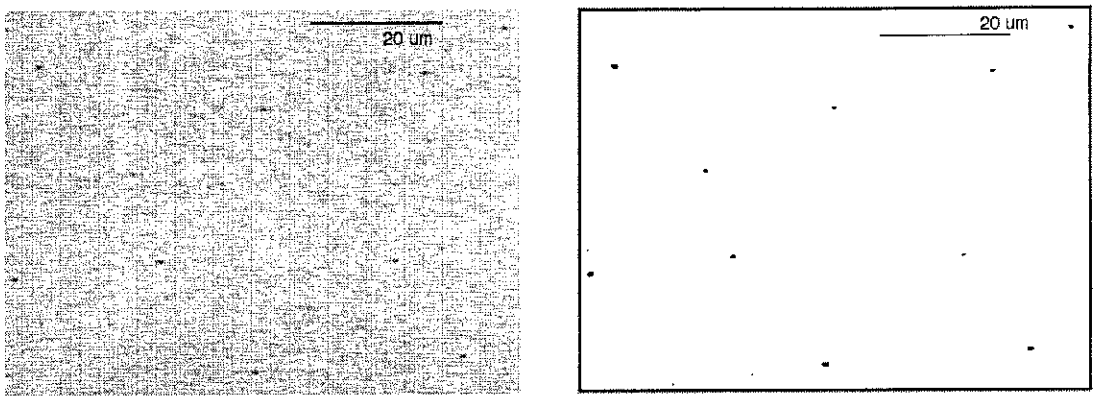


Figure 6.6: SEM image of a decorated Nb thin film for an applied field of B=0 mT.

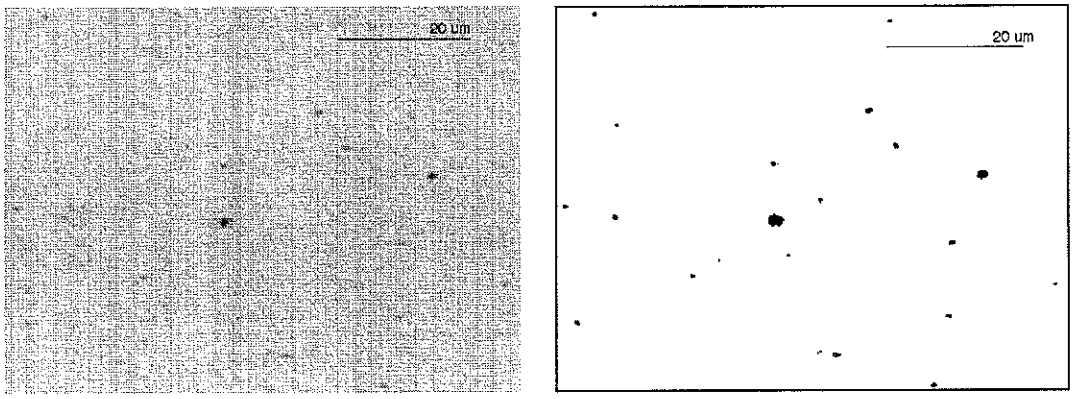


Figure 6.7: SEM image of a decorated Nb thin film for an applied field of B=0.01 mT.

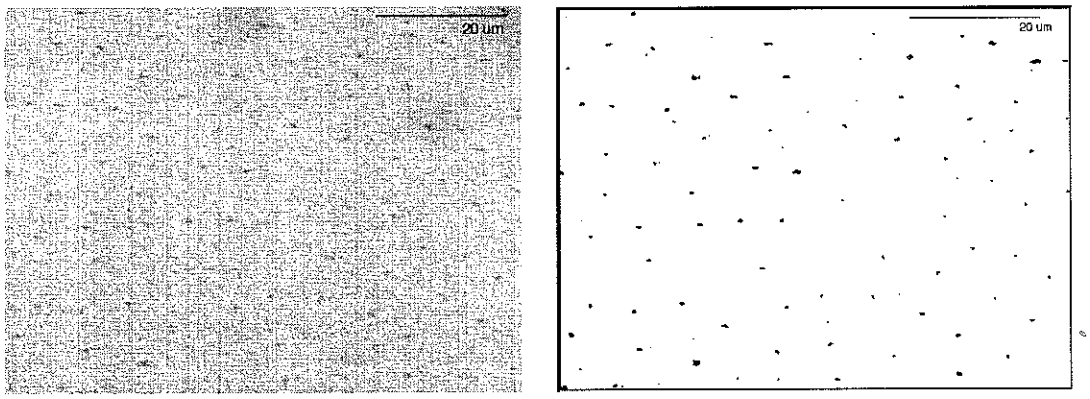


Figure 6.8: SEM image of a decorated Nb thin film for an applied field of B=0.03 mT.

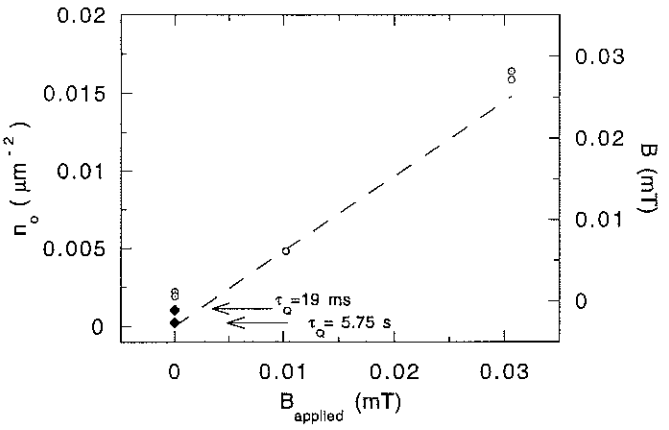


Figure 6.9: Vortex density represented as total flux per unit surface as a function of applied field obtained from the decoration experiments. The dashes line represents the Abrikosov vortex density. The quenched vortex density estimated for two different cooling rates $\tau_Q = 19$ ms and $\tau_Q = 5.75$ s are represented by solid diamonds.

density at non-zero field is close to the density of Abrikosov vortices. In zero field, the vortex density is non-zero and equal to $2 \times 10^{-3}$ vortices/$\mu$m$^2$, well above the estimated $0.3 \times 10^{-3}$ vortices/$\mu$m$^2$ for vortex quenching at the same cooling rate, as well as for the faster quenching $\tau_Q = 19$ ms, which is $1 \times 10^{-3}$ vortices/$\mu$m$^2$. These estimations are for the presented in Fig. 6.9 by solid diamonds. The error on the experimental vortex density is associated to the vortex counting, which was approximately $0.2 \times 10^{-3}$ vortices/$\mu$m$^2$ for these decorations.

Though this decoration results are not conclusive in respect to quenched vortices, they demonstrate that the decoration technique has enough magnetic sensitivity to visualize vortices separated from a few tens of a micron, of the order of the predicted quenched vortex separations.

Nevertheless, even in ideal cooling conditions, the initial defect density can be significantly decreased due to several factors: vortex-antivortex recombination, thermal fluctuations and the mobility of the quenched vortex at finite temperatures.

The intrinsic pinning of the material may not be sufficient to impede the initial vortices and anti-vortices from moving, specially at temperatures close to the transition where it is washed out by thermal activation. The introduction of artificial pinning structures may prevent the vortex migration during the cooling procedure.

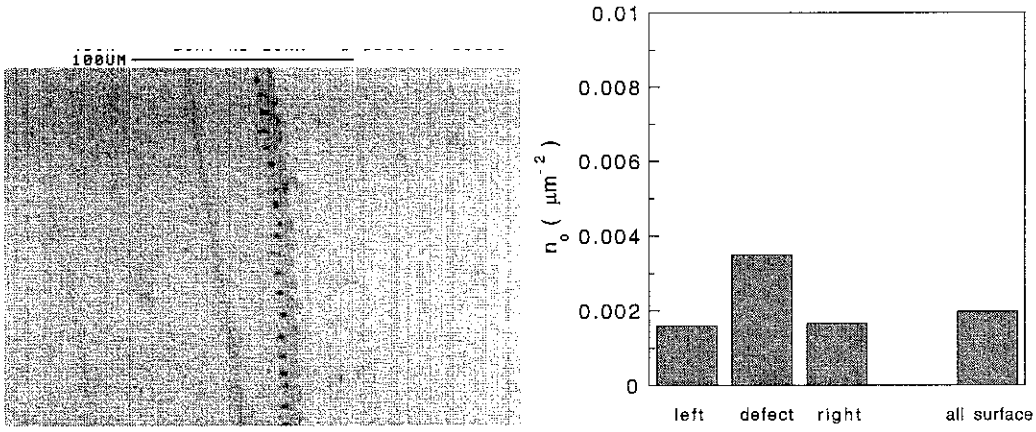


Figure 6.10: SEM image of the sample decorated at applied zero field near a defect of the niobium layer.

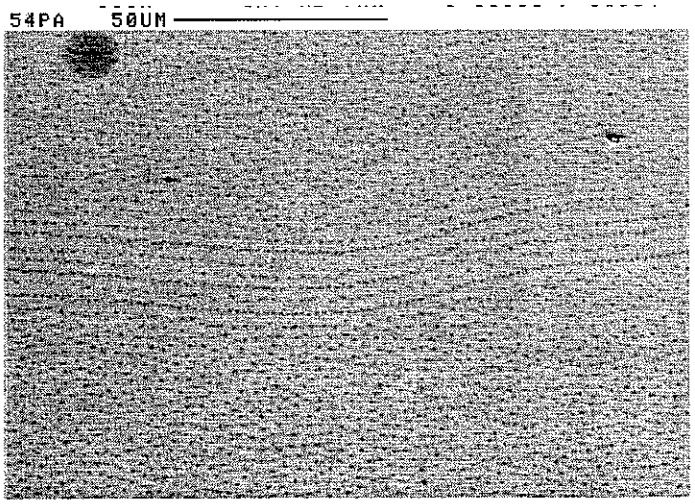


Figure 6.11: SEM image of a Nb sample decorated at B=0.28 mT, not showing a broadening of the spot size.

In Fig. 6.10 is displayed a SEM image of the sample decorated at applied zero field (Fig.6.6) near a defect of the niobium layer. We can observe an accumulation of black large spots along the defect. The vortex density over the entire surface is comparable to the vortex density measured in other part of the sample. However, if we compare the vortex densities in a intermediate region centered on the defect line ($\approx$ 40 $\mu$m large) and the vortex densities in the respective regions on the left and on the right, we obtain a flux density on the central region which is about the double of the other regions. Besides, the average distance between vortices situated on the linear defect is 7.7 $\mu$m, in contrast to an average distance of 21.9 $\mu$m in the homogeneous film, indicating that the vortex attraction by the defect is much stronger than the vortex-vortex interaction.

We remark that the diameter size of the spots over the defect line is approximately 2.7 $\mu$m, in contrast to 1 $\mu$m in the homogeneous film. This may be due to an anomalous weakening of the shielding currents close to this defect. Decorations performed at other applied fields, which exhibit the same linear vortex distribution, do not show a broadening of the spot size, as can be seen in fig. 6.11, where is displayed a Nb sample decorated at 0.28 mT.

## 6.4 Concluding Remarks

The results presented in this chapter have shown that our decoration technique presents a good magnetic resolution to detect weak vortex densities (that is a magnetic induction below 4 $\mu$T) and that cooling rates of at least several milliseconds can be achieved by heating the sample *via* a short heat pulse. Our preliminary studies performed with a LED indicate a good improvement on the cooling rate, which can be further increased by using a pulsed laser focused on the sample. Besides, the magnetic resolution achieved is well above the resolution on applied field of 0.4 $\mu$T (Chap. 3). The pulsed laser presents some advantages: the sample can be kept at a temperature well below the transition before the pulse (in contrast to our LED, only able to vary the sample temperature by $\approx$ 0.5 K) and the short decay time of the laser ($<$ 2 ns) will not be itself a limit in the sample response time. The disadvantage of

this method is that the laser is focused on a limited region of the sample (for example, a spot of 50 $\mu$m), thus generating temperature gradients in the sample.

Finally, the measurement of the residual field using Josephson arrays as described in Chap. 3 allows a good resolution compensation of the effective field, thus suitable for quenching rates performed with cooling rates of the order of a millisecond.

# Chapter 7

# General Conclusions

The main results presented in this thesis concerned phase coherence and localization effects in superconducting arrays which result from an interplay between the applied field and the array topology.

In a first part we studied the effects of the interaction between superconducting edge states on the transition line of superconducting arrays of holes. The hole density in the studied arrays places them in an intermediate regime, between the isolated hole (large spacing) and the wire network (small hole spacing) behaviour. This intermediate regime is very interesting since the interference between neighbour edge states can be tuned by changing the magnetic field. By decreasing the applied field we can induce a crossover from a *dilute* system, dominated by localised edge states around each hole, to a collective regime where interference phenomena over the array unit cell dominates over the flux quantization at the individual holes. In the present work we addressed the role of interactions between edges states at low fields. We studied an array whose collective regime is well described by the wire network formalism. We identified a clear crossover to the single hole regime with increasing field which is associated to the crossover from a two-boundary (thin slab limit) to a one boundary nucleation at hole edges. These nucleation phenomena had not been studied in a multiple connected geometry such as an array. They are responsible for novel properties of the superconductive arrays, namely the clear enhancement of the nucleation fields ratio $H_{c3}/H_{c2}$ and the ordering of the interstitial vortices induced at low fields. These results were confronted with previous work as well as a simple model proposed

by Rosario Fazio for dilute arrays, which allowed us a global understanding of the problem.

On a second part we presented the first experimental results on a novel localization phenomenon induced by magnetic field in two-dimensional periodic networks. In this case, we used superconducting wire networks as model systems. In the context of a superconductive wire network, we were expecting to find anomalies in its transport properties at half-flux as well as on the network fluxoid configurations. We used the well known mapping of the linear Ginzburg-Landau formalism into the tight binding problem to infer some of the exotic effects of this localization phenomena in the energy spectrum. In particular, the strong maxima of the groundstate energy at half-flux and the absence of band structure at this field. From the transport measurements we have found an excellent agreement between the field dependence of the array transition line and of the ground state eigenenergies, which confirmed the presence of an absolute energy maxima ($T_c(f)$ minima) at this field. The critical current measurements shown that the lowest values are attained at half-flux and were in good qualitative agreement with the calculations of the superfluid velocity, obtained from the spectrum curvature close to the ground state. The imagery of the fluxoid distributions by Bitter decoration revealed a highly disordered vortex state at frustration $f = 1/2$, while fluxoid ordering was identified at frustrations $1/3$ and $2/3$. The ensemble of these results confirm the singular nature of the state at half-flux. They are in clear contrast with the behaviour at half-flux for other regular periodic lattices and give a strong support for the existence of this localization phenomena.

In this experimental approach we only focused on the static properties of the networks, that is on probing the phase configurations for a given static field. The validity regime for the above mentioned mapping constrained us to work at temperatures close to the network transition, thus we cannot inspect the band structure far away from the ground state level. Some interesting questions concerning the nature of the superconducting transition at half-flux, the vortex dynamics and the vortex state at this field (disordered vortex lattice, vortex glass ?) remains to be addressed. The study of other systems such as Josephson junction arrays or 2D electron gas hetero-structures may help to clear some of these questions.

In the course of this thesis work, some nanofabrication techniques were adapted to the needs of the studied samples, particularly a tri-layer process of PMMA/Si/PMMA was developed for the patterning of large arrays using Deep-Ultra Violet photolithography. Some important improvements on the transport and decoration techniques were also carried out. The automation of the transport measurements in C programming language now offers an easy access to any user. We also optimized the conditions to perform temperature quenching experiments by Bitter decoration using 2D superconducting systems. Namely, the cooling rates in the decoration chamber were improved and a high precision measurement of the effective zero magnetic field was implemented using Josephson junction arrays. A field resolution better than one vortex per 0.01 $mm^2$ surface was attained and can be further increased. This resolution is suitable for decoration experiments with a high resolution in the applied field, namely in the detection of vortex formation by temperature quenching in zero field which are being carried out.

# Conclusions Générales

Les principaux résultats présentés dans cette thèse concernent des phénomènes de cohérence de phase et de localisation dans des réseaux supraconducteurs. Ces effets résultent d'une combinaison subtile entre l'effet du champ magnétique et la géométrie du réseaux. Dans une première partie nous avons étudié l'effet des interactions entre états supraconducteurs de surface sur la ligne de transition supraconducteur-normal des réseaux de trous de taille micronique. La densité de défauts dans les réseaux étudiés les situe dans un régime intermédiaire, entre un comportement de trou isolé (distance grande) et un comportement du type de réseau de fils (distance petite). Ce régime intermédiaire est très intéressant, car l'interférence entre les états de bord adjacents peut être changé par le champ magnétique. En diminuant le champ magnétique, on peut induire une transition d'un comportement de système dilué , c'est-à-dire, dominé par les états de bords localisés autour de chaque trou, vers un régime collectif où des phénomènes d'interférence à l'échelle de plusieurs trous dominent. Dans ce travail nous avons abordé les interactions entre les états de bords des trous voisins à bas champ. Nous avons étudié un réseau pour lequel le régime collectif est bien décrit par le formalisme des réseaux de fils supraconducteurs. Nous avons pu observé une transition très claire vers le régime de trou isolé en augmentant le champ. Cette transition est associée au passage d'une nucléation de supraconductivité déterminée par les deux bords de trous voisins (comme dans la limite de fil étroit) à une nucléation où seules les conditions de frontières au bord d'un trou sont importantes. Ces phénomènes de nucléation dans la géométrie multiconnexe d'un réseau n'avaient pas été étudié auparavant. Ils sont à l'origine de propriétés nouvelles, notamment l'augmentation du rapport $H_{c3}/H_{c2}$ et l'apparition d'une configuration ordonnée des vortex interstitiels à bas champ. Nous avons comparés l'ensemble des résultats présents et antérieurs

avec un modèle théorique simple, proposé par Rosario Fazio pour des réseaux dilués, ce que nous a permis une compréhension globale du problème.

Dans une deuxième partie, nous avons présenté l'étude expérimentale d'un phénomène de localisation induit par le champ magnétique dans un réseau périodique bidimensionnel. Pour cette étude, nous avons utilisés les réseaux de fils supraconducteurs comme système modèle. Dans le contexte d'un réseau supraconducteur, on s'attend à des anomalies importantes dans les propriétés de transport et dans la configuration de vortex à demi quanta de flux. L'isomorphisme entre le formalisme des équations linéaires de GL pour les réseaux et le modèle des liaisons fortes nous permet d'accéder à certaines propriétés du spectre d'énergie qui sont reliées au phénomène de localisation. Citons notamment, le maximum de l'énergie de l'état fondamental qui est atteint à demi quanta de flux et l'absence de bande d'énergie pour cette valeur de champ. Nous avons trouvé un excellent accord entre la dépendance en champ de la transition supraconducteur-normal des réseaux et les valeurs propres d'énergie de l'état fondamental. Les mesures de courant critique ont montré que les valeurs les plus faibles sont obtenues à demi flux, et sont en bon accord qualitatif avec les valeurs théoriques, obtenues à partir du calcul de vitesse de groupe proche de l'état fondamental. L'imagerie des positions des vortex par la décoration de Bitter a montré que les distributions à demi flux sont très désordonnées, tandis que nous avons pu identifier des structures ordonnées à frustrations $f = 1/3$ et $2/3$. Ces résultats confirment la nature singulière de l'état à demi flux. L'ensemble de nos résultats donne un bon support à l'existence de ce phénomène de localisation. Dans cette étude expérimentale, nous avons seulement considéré les propriétés statiques du réseau, c'est-à-dire, les configurations de phase sous champ magnétique statique. D'autre part, comme l'isomorphisme entre l'approche linéaire de GL et le problème de liaisons fortes est valable uniquement aux températures très proches de la température de transition, l'intérieur du spectre d'énergie nous reste inaccessible. Quelques questions intéressantes, à savoir la nature de la transition supraconductrice à demi flux, la dynamique de vortex et l'état de vortex (réseaux de vortex désordonnée, verre de vortex ?) à cette valeur de champ reste à répondre. L'étude de ce phénomène dans d'autres systèmes comme les réseaux de jonctions Joseph-

son ou des structures de gaz d'électrons 2D peuvent aider à clarifier beaucoup d'entre elles. Dans le déroulement de ce travail de thèse, nous avons adaptés des techniques de nanofabrication de *lift-off* et de gravure au besoins de nos échantillons. Un procédé de tri-couche PMMA/Si/PMMA a été développé pour la fabrication des réseaux étendus par photolithographie en ultraviolet profond. Des améliorations significatives de la technique de mesures de transport et de décoration ont aussi été apportées. Nous avons automatisatisé l'acquisition des mesures de transport par un programme en langage C qui offre un accès simple à tout utilisateur. D'autre part, nous avons optimisé la technique de Bitter pour l'application à des expériences de trempe en température dans des systèmes supraconducteurs à deux dimensions. Notamment, le taux de refroidissement a été amélioré et une mesure de très bonne résolution du zéro effectif du champ magnétique a été mise au point, en utilisant des réseaux de jonctions Josephson. Une résolution dans la mesure de champ meilleure que un vortex par 0.01 $mm^2$ de surface a été atteinte. Ce valeur correspond bien au requis des expériences de trempe à champ nul.

# Bibliography


[1] O. Buisson. PhD thesis, Univ. Joseph Fourier, Grenoble I, France, 1990.

[2] W. M. Moreau. Semiconductor Lithography - Principles, Practices and Materials. Plenum Press, New York, 1988.

[3] M.J. Kelly and C. Weisbuch, editors. The Physics and Fabrication of Microstructurs and Microdevices. Springer-Verlag Berlin Heidelberg, 1986.

[4] IBM J. Res. Develop., 24, 1980.

[5] K. Runge. Visualisation de fluxoides dans des réseaux 2D artificiels supraconducteurs. PhD thesis, Univ. Joseph Fourier, Grenoble I, France, 1993.

[6] P. Dubos, P. Charlat, T. Crozes, P. Paniez, and B. Pannetier. submitted to J. Vac. Sci. and Tech. B, 1999. Cond-Mat 9909053.

[7] H. Träuble and U. Essmann. J. Sci. Instrum., 43:344, 1966.

[8] H. Träuble and U. Essmann. Phys. Stat. Sol., 20:95, 1967.

[9] K. Runge and B. Pannetier. Europhys. Lett., 24:737, 1993.

[10] A. Bezryadin, Yu.N. Ovchinikov, and B. Pannetier. Phys. Rev. B, 53:8553, 1996.

[11] G. S. Mkrtchyan and V. V. Shmidt. Soviet Phys. JETP, 44:195, 1972.

[12] R. Theron, S.E. Korshunov, J.B. Simond, Ch. Leemann, and P. Martinoli. Phys. Rev. Lett., 72:562, 1994.

[13] A. Lobb, D. W. Abraham, and M. Tinkham. Phys. Rev. B, 36:150, 1983.

[14] A. Bezryadin and B. Pannetier. J. Low Temp. Phys., 98:251, 1995.

[15] A. Bezryadin and B. Pannetier. Physica Scripta, T-66:225, 1996.

[16] A.T. Fiory, A.F. Hebard, and S. Somekh. Appl. Phys. Lett., 32:73, 1978.

[17] M. Baert, V.V. Metlushko, R. Jonckheere, V.V. Moschalkov, and Y. Bruynseraede. Phys. Rev. Lett., 74:3269, 1995.

[18] A.I. Buzdin. Phys. Rev B, 47:11416, 1993.

[19] S. Alexander. Phys. Rev. B, 27:1541, 983.

[20] R. Rammal, T.C. Lubensky, and G. Toulouse. Phys. Rev. B, 27:2820, 1983.

[21] D. Saint-James and P.G. de Gennes. Phys. Lett., 7:306, 1963.

[22] L.G. Aslamazov and A.I. Larkin. Phys. Lett. A, 26:238, 1968.

[23] A. Abrikosov. Fundamentals of the theory of metals, Chap. 21. North-Holland, 1988.

[24] P.G. de Gennes. Superconductivity in Metals and Alloys, Chap. 8. Benjamin, New York, 1966.

[25] K. Maki. Superconductivity, Chap. 18. R.D. Parks (Dekker, New York), 1969.

[26] D. F. Hofstadter. Phys. Rev. B, 14:2239, 1976.

[27] B. Pannetier, J. Chaussy, R. Rammal, and J.C. Villegier. Phys. Rev. Lett., 53:1845, 1984.

[28] Y.Y. Wang, B. Douçot, R. Rammal, and B. Pannetier. Phys. Lett. A, 199:145, 1996.

[29] H.J. Fink, A. Lopez, and R. Maynard. Phys. Rev. B, 25:5237, 1982.

[30] H.A. Schultens. Z. Physik, 232:430, 1970.

[31] A. Bezryadin, A.I. Buzdin, and B. Pannetier. Phys. Rev. B, 51:3718, 1995.

[32] Yu.N. Ovchinnikov. Sov. Phys. JETP, 52:755, 1980.

[33] R. Benoist and W. Zwerger. Z. Phys. B, 103:377, 1997.

[34] M. Tinkham. Introduction to Superconductivity. Mac Graw-Hill New York, 1996.

[35] J.J. Palacios. Phys. Rev. B, 57:10873, 1998.

[36] C.C. Abilio, P. Butaud, Th. Fournier, B. Pannetier, S. Tedesco, B. Dalzotto, and J. Vidal. Phys. Rev. Lett., 83:5102, 1999. Cond-Mat 9907187.

[37] J. Vidal, R. Mosseri, and B. Douçot. Phys. Rev. Lett., 81:5888, 1998.

[38] R. Schuster and K. Ensslin. Adv. Solid State Phys., 34:195, 1994.

[39] NATO Advanced Research Workshop on Coherence in Superconducting Networks, 1988.

[40] P.G. de Gennes. C.R. Acad. Sci. Ser. B, 292:9 and 279, 1981.

[41] Y. Aharonov and D. Bohm. Phys. Rev., 115:485, 1959.

[42] P. Butaud. unpublished.

[43] F. H. Claro and G. H. Wannier. Phys. Rev. B, 19:6068, 1979.

[44] B. Pannetier, J. Chaussy, and R. Rammal. J. Phys. Lettres, 44:L–853, 1983.

[45] B. Pannetier, O. Buisson, P. Gandit, Y.Y. Wang, J. Chaussy, and R. Rammal. Surf. Sci., 229:331, 190.

[46] M. Giroud, O. Buisson, Y.Y. Wang, and B. Pannetier. J. Low Temp. Phys., 87:683, 1992.

[47] B. Pannetier, J. Chaussy, R. Rammal, and J.C. Villegier. Phys. Rev. Lett., 53:1845, 1984.

[48] M.A. Itzler, R. Bojko, and P. Chaikin. Europhys. Lett., 20:639, 1992.

[49] O. Buisson, M. Giroud, and B. Pannetier. Europhys. Lett., 12:727, 1990.

[50] A. Abrikosov. Soviet Phys. JETP, 5:1174, 1957.

[51] Y.Y. Wang, R. Rammal, and B. Pannetier. J. Low Temp. Phys., 68:301, 1987.

[52] C.C. Chi, P. Santhanam, and P.E. Blochl. J. Low Temp. Phys., 88:163, 1992.

[53] A.M. Chang, H.D. Hallen, L. Harriott, H.F. Hess, H.L. Kao J. Kwo, R.E. Miller, R. Wolfe, J. vand der Ziel, and T.Y. Chang. Appl. Phys. Lett., 61:1974, 1992.

[54] H.D. Hallen, R.Seshadri, A.M. Chang, R.E. Miller, L.N. Pfeiffer, K.W. West, C.A. Murray, and H.F. Hess. Phys. Rev. Lett., 71:3007, 1993.

[55] L.N. Vu, M.S. Winstrom, and FD.J. van Harlingen. Appl. Phys. Lett., 63:1963, 1993.

[56] S. Teitel and C. Jayaprakash. Phys. Rev. Lett., 51:1999, 1983.

[57] M.R. Kolahchi and J.P. Straley. Phys. Rev. B, 43:7651, 1991.

[58] W.Y. Shih, C. Ebner, and D. Stroud. Phys. Rev. B, 30:134, 1984.

[59] M.Y. Choi and S. Doniach. Phys. Rev. B, 31:4516, 1985.

[60] S.E. Korshunov, A. Vallat, and H. Beck. Phys. Rev. B, 51:3071, 1995.

[61] W.Y. Shih and D. Stroud. Phys. Rev. B, 32:158, 1985.

[62] T.C. Halsey. Phys. Rev. Lett., 55:1018, 1985.

[63] T.C. Halsey. Physica B, 152:22, 1988.

[64] P. Gupta, S. Teitel, and M.J.P. Gingras. Phys. Rev. Lett., 80:105, 1998.

[65] H.S.J van der Zant, M.N. Webster, J. Romojn, and J.E. Mooij. Phys. Rev. B, 42:2647, 1990.

[66] I. Chuang, N. Turok, and B. Yurke. Phys. Rev. Lett., 66:2472, 1991.

[67] M.J. Bowick, L: Chander, E.A. Schiff, and A.M. Srivastava. Science, 263:943, 1994.

[68] C. Bauerle, Y.M. Bunkov, S.N. Fisher, H. Godfrin, and G.R.Pickett. Nature, 382:332, 1996.

[69] V.M.H. Ruutu, V.B. Eltsov, A.J. Gill, T.W. Kibble, M. Krusius, Yu.G. Makhlin, B. Plaais, G.E. Volovik, and Wen Xu. Nature, 382:334, 1996.

[70] M.E. Dodd, P.C. Hendry, N.S. Lawson, P.V.E. McClintock, and C.D. Williams. Phys. Rev. Lett., 81:3703, 1998.

[71] M.E. Dodd, N.S. Lawson, R.A.M. Lee, P.V.E. McClintock, and C.D. Williams. Nature, 368:315, 1994.

[72] W.H. Zurek. Nature, 317:505, 1985.

[73] T.W.B. Kibble. J. Phys. A, 9:387, 1976.

[74] P. Laguna and W.H. Zurek. Phys. Rev. Lett., 78:2519, 1997.

[75] O. Bethoux, R. Brusetti, J.C. Lasjaunias, and S. Sahling. Cryogenics, 35:447, 1995.

# List of Figures

Nous avons étudié expérimentalement des réseaux supraconducteurs bidimensionnels soumis à un champ magnétique transverse. Nous observons des phénomènes d'interférences quantiques de la fonction d'onde supraconductrice qui résultent des effets joints du champ magnétique et de la topologie du réseau. Les techniques de nano-fabrication des échantillons sont présentées. Nous avons étudié par des mesures de transport les interactions entre les états supraconducteurs de surface dans des réseaux de trous microniques et montré que la nature de ces interactions change avec la distance entre les trous. Lorsque la longueur de cohérence est supérieure à cette distance, nous retrouvons le comportement de couplage fort obtenu dans des réseaux de fils supraconducteurs. Dans le cas contraire, il est décrit par un couplage faible. Une comparaison avec la théorie est effectuée. Ensuite nous avons observé, pour la première fois, des effets de localisation induit par le champ magnétique dans un réseau supraconducteur périodique *étoilé*. Cet effet apparait lorsque le flux magnétique par cellule est égal à un demi quantum. Dans une description de liaisons fortes il s'explique par des interférences destructives de type Aharonov-Bohm. Des réseaux de fils supraconducteurs ont été utilisés comme systéme-modèle. La ligne de transition et le courant critique en fonction du champ sont étudiés par des mesures de transport. Les résultats sont en très bon accord avec la théorie, dans le cadre d'un formalisme de Ginzburg-Landau linéaire pour les réseaux de fils. En particulier à un demi quantum de flux, la ligne de transition présente un maximum et le courant critique s'affaiblit fortement. De plus la décoration de Bitter montre une distribution des vortex très désordonnée en opposition aux structures obtenus aux flux 1/3 et 2/3. Dernièrement nous avons optimisé la technique de Bitter pour des expériences de trempe en température dans des systèmes supraconducteurs 2D.

Mots clés

1. Supraconductivité
2. Cohérence Quantique
3. Localisation
4. Nanofabrication
5. Physique Mésoscopique
6. Réseaux supraconducteurs
7. Vortex


Grenoble, janvier 2000

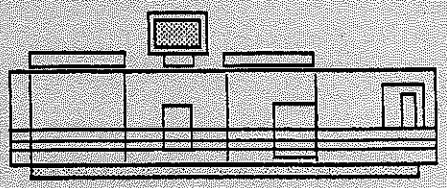

Imprimé sur "Xerox 5090"
au Service Reprographie du CNRS de Grenoble